MOIST STATIC ENERGY BUDGET ANALYSIS OVER THE TROPICAL OCEAN

by

Kuniaki Inoue

A dissertation submitted in partial fulfillment of
the requirements for the degree of

Doctor of Philosophy

(Atmospheric and Oceanic Sciences)

at the

UNIVERSITY OF WISCONSIN–MADISON

2016

Date of final oral examination: 08/01/16

The dissertation is approved by the following members of the Final Oral Committee:

Larissa E. Back, Assistant Professor, Atmospheric and Oceanic Sciences
Daniel J. Vimont, Associate Professor, Atmospheric and Oceanic Sciences
Gregory J. Tripoli, Professor, Atmospheric and Oceanic Sciences
Matthew H. Hitchman, Professor, Atmospheric and Oceanic Sciences
Samuel N. Stechmann, Associate Professor, Mathematics

Acknowledgments

First of all, I must thank my adviser, Prof. Larissa Back, for her every effort to support my academic life. She spent tremendous amount of time attempting to give me the essence to be a good scientist. Because I am a person who can be easily distracted (well, I should say I have great curiosity about everything), she has made a great effort to get me back on the right track. Besides, she sent me to a lot of conferences (I went to four conferences last year), one of which I met Dr. Yi Ming at, who is one of my postdoc advisers at GFDL. I would like to thank her endless and generous support, which made me a qualified PhD.

I also want to thank the rest of my PhD committee members: Profs. Dan Vimont, Greg Tripoli, Matt Hitchman, and Sam Stechmann (ordered alphabetically). I took three classes taught by Dan, and all of them were fascinating. But I want to emphasize that his statistics class was the most useful among all the classes I've ever taken in my life. Actually, the statistical tools I used when I wrote all of my papers (e.g., time filters, spectral analyses, EOF analyses, lag regression, composite analyses, statistical tests, etc.) were all from the materials I got in Dan's class. I will keep using those tools forever! Greg is a person who aroused my interest in atmospheric modeling. I took his modeling class, and spent one-and-a-half years to finish that class (I kept it incomplete) with the anelastic non-hydrostatic model which I wrote up from scratch. I still vividly remember my excitement when I found my model created a nice mushroom flow. I'm still fascinated by modeling, and

want to study convective parameterization someday in the future. The dynamics class I first took was Matt's class, which made me love fluid dynamics. I really thank Matt for letting me keep using his group's office. I really liked that (messy and chaotic) room with nice roommates, Marek, Shellie, and Ross. The most vivid memory of Matt is the fantastic one on his sailing boat. That was really fun. I also wonder if the goat kept by his neighbor is still making an annoying sound at night. Before entering the AOS department, I wanted to study the applied math. I am still most fascinated by theoretical approaches to solve problems in the atmosphere. So I'm fascinated by Sam's theoretical studies. The greatest regret I have in my grad student life is that I was not able to take his applied math class due to a time conflict.

I wish to thank Debbie, Kathy, Sonja, and Sue. I often stopped by their office to ask a favor just before the deadline. Thanks to their help, I got correct documents and reimbursement without any problems. I also want to thank all the faculty members in the AOS department. My life in this department was fantastic. I would like to thank the SSEC technical support members. Among them, I especially want to thank Jesse Stroik. Without his help, it was definitely impossible for us to finish our project. His technical support improved our productivity and computational speed tremendously.

I am grateful to all my friends in Madison, other cities, other countries, and my home town. And finally, I would like to express my deepest gratitude to my family for their eternal support and patience.

Contents

List of Tables

List of Figures

Abstract

In this dissertation work, we analyze moist static energy (MSE) budgets and associated quantities in a various ways. First, we investigate MSE budgets on four different time scales (around 2-day, 5-day, 10-day, and MJO time scales) with the TOGA COARE field campaign data set and a lag-regression analysis. This analysis reveals that the MSE budgets behave in significantly different ways on the different time scales. On the shorter time scales, the vertical MSE advection acts as a primary driver of the recharge-discharge cycle of column MSE. As the time scale gets longer, in contrast, the relative contributions of the other budget terms become greater. Vertical velocity profiles also exhibit significantly different patterns among the different time scales, leading to different behaviors of the gross moist stability (GMS) among the time scales.

Second, utilizing the same TOGA COARE data, we investigate the GMS and its relevant quantities in a unique way. In this analysis, we coined the critical GMS, which is a ratio of the diabatic MSE source to the intensity of convection, and the drying efficiency, which is defined as the GMS minus the critical GMS. Our analysis reveals that convection amplifies/decays via negative/positive drying efficiency, which is associated with a bottom-heavy/top-heavy vertical velocity profile, respectively. We also propose various ways of computing quasi-time-independent "characteristic GMS", and discuss the physical interpretations of it.

Finally, we present a novel diagnostic application of the GMS, called the "GMS

plane analysis". It is demonstrated with satellite-based data sets. The analysis reveals that the GMS plane acts as a phase plane in which each convective life-cycle can be viewed as an orbiting fluctuation around some critical line that is determined by the feedback mechanisms of the diabatic MSE source terms. The geographic variability of the characteristic GMS is depicted. We also discuss general misconceptions in the past MSE budget studies which, implicitly or explicitly, attempted to associate the temporal variability of MSE budgets with the linear moisture-mode theory.

Chapter 1

Introduction

1.1 Background

The dynamics of the tropical atmosphere is a less mature science compared to that of the extratropical atmosphere. Because most of the tropical region is covered by ocean, before the advent of satellites, the atmosphere in this region was poorly observed. And even after the advent of satellites, the amount and quality of observational data there are much poorer compared to those in mid and high latitudes. The lack of accurate observation is, even now, one of the main stumbling blocks that keeps many tropical phenomena from a better understanding.

Besides the deficiency of observation, there is a lack of simple theoretical framework that can provide us with an overall understanding of large-scale tropical motions. In middle and high latitudes, a quasi-geostrophic theory and potential vorticity thinking work well to predict the synoptic-scale motions. The primary energy source for the motions that are explained by the quasi-geostrophic theory is associated with horizontal temperature gradient, and latent heat release and radiative heating are usually secondary contributors in the extratropics. By contrast, in the tropics, horizontal temperature gradient is negligible due to small Coriolis effects. Besides, latent heat release is the primary energy source, and radiative heat-

ing also plays an important role there. Therefore, the theoretical framework that has been developed through a relatively long history of extratropical meteorology and fluid dynamics does not provide an overall understanding of tropical motions.

For a better understanding of the tropical atmosphere, we need a different theoretical framework from the one for the extratropics, and that framework must explain the mechanism of an interaction between latent heat release and large-scale motions. This interaction is, indeed, one of the key subjects that tropical meteorologists have keenly studied about for a few decades, but is yet to be fully understood. A difficulty in understanding this interaction arises from the fact that latent heat release and tropical large-scale motions are in the chicken-egg problem. The ensemble of convective clouds (that are the primary source of the latent heat) alters large-scale circulations. But those large-scale circulations, in which the convective clouds are embedded, in turn, modulate the convective clouds by changing the local favorability for convection.

One example of the manifestation of such an interaction is the convectively coupled equatorial wave (CCEW). Matsuno (1966) solved the shallow water equations in an equatorial β plane, and found that there are a couple zonally propagating waves that are trapped about the equator. At about the same time as the theoretical prediction by Matsuno, some observational studies provided strong evidence for the existence of the equatorially trapped waves in the lower stratosphere (e.g., Yanai and Maruyama, 1966; Maruyama and Yanai, 1967; Wallace and Kousky, 1968). The Matsuno model gained more attention after the advent of meteorological satellites. Takayabu (1994) and Wheeler and Kiladis (1999) performed a space-time spectral

analysis of tropical cloudiness (or IR image) and found that the wave signals are surprisingly consistent with the dispersion curves predicted by the Matsuno model except that the observed phase speeds of these waves are considerably slower than those predicted by the theory. This reduction of the phase speeds is due to an interaction between moist convection and large-scale motions, and the equatorial waves with such reduced phase speeds are called the convectively coupled equatorial waves [CCEWs; refer to a review paper by Kiladis et al. (2009)]. Many theoretical explanations about the mechanism of the CCEWs have been proposed. However, this mechanism still remains unclear, and is currently an open, active, and challenging problem.

Another example of the manifestation of an interaction between convection and large-scale motions is the Madden-Julian oscillation (MJO). The MJO was revealed by Madden and Julian (1971, 1972), who found a spectral peak in pressure and zonal wind fields with a period range of 40–50 days. It is characterized as an envelope of deep convection around 10,000 km in zonal scale, with an eastward phase speed in the rage of 4–8 m s^{-1} coupled to the large-scale circulation [see reviews by Madden and Julian (1994) and Zhang (2005)]. The MJO is currently one of the most active research subjects in tropical meteorology. Because of its significant influence on the global weather-climate (e.g., Zhang, 2005, 2013), a better understanding of the mechanism of the MJO is of great importance. However, it is notoriously difficult to simulate the MJO correctly in general circulation models (e.g., Lin et al., 2006; Kim et al., 2009; Benedict et al., 2013). The reason for the unsatisfactory skill of MJO simulations remains uncertain.

Someday in future, the advancement of computational ability may enable us to build a super-high-resolution global cloud resolving mode in which we don't need to parametrize the statistical effects of convective clouds. Such a model may be able to simulate the CCEWs, MJO, and other tropical phenomena in a realistic manner. However, simulations without a conceptual understanding can be perilous, and just provide us with an enormous series of numbers created by the model that don't tell us about the physics of the world. That is intellectually empty.

Therefore, we need to conceptually understand the mechanism of an interaction between moist convection and large-scale motions. But how can we achieve that? Recent literature consider that atmospheric moisture plays a crucial role in the tropical atmosphere, and careful diagnoses of it are of great importance. And for the diagnoses of atmospheric moisture, it has been proven that a moist static energy (MSE) budget analysis is useful. In the current dissertation work, we focus on assessments of the MSE budgets and its relevant quantities, which are briefly introduced below.

1.2 Moist static energy budget analysis in the tropics

The history of moist static energy (MSE) budget analyses can be traced back, at least, to the 1950s when Riehl and Malkus (1958) proposed a "hot tower" hypothesis based on their MSE budget analysis within the tropical convergence zone. But it may be Yanai et al. (1973), who first established a thorough diagnostic framework with the MSE budgets. Thus we start our argument following Yanai et al. (1973).

They started with the equations of the mass continuity, energy conservation, and moisture conservation, averaged over a large (a few hundred km scale) horizontal area:

$$\widehat{\nabla \cdot \mathbf{v}} + \frac{\partial \widehat{\omega}}{\partial p} = 0, \tag{1.1}$$

$$\frac{\partial \widehat{s}}{\partial t} + \widehat{\nabla \cdot s\mathbf{v}} + \frac{\partial \widehat{s\omega}}{\partial p} = \widehat{Q_R} + L(\widehat{c} - \widehat{e}), \tag{1.2}$$

$$\frac{\partial \widehat{Lq}}{\partial t} + \widehat{\nabla \cdot Lq\mathbf{v}} + \frac{\partial \widehat{Lq\omega}}{\partial p} = L(\widehat{e} - \widehat{c}), \tag{1.3}$$

where $s \equiv c_p T + gz$ is dry static energy (DSE); q is water vapor mixing ratio; Q_R is radiative heating rate; L is the latent heat of evaporation; c is the rate of condensation; e is the rate of re-evaporation of cloud droplets; and the hat denotes a horizontal average. When using these equations, we neglect the production of kinetic energy, latent heat release due to ice processes, and other residual, which is justifiable in the tropics (e.g., Johnson and Ciesielski, 2000).

With the aid of Eq. 1.1 and the Reynolds averaging technique, Eqs. 1.2 and 1.3 can be re-arranged into

$$\frac{\partial \widehat{s}}{\partial t} + \widehat{\mathbf{v}} \cdot \nabla \widehat{s} + \widehat{\omega} \frac{\partial \widehat{s}}{\partial p} = \widehat{Q_R} + L(\widehat{c} - \widehat{e}) - \nabla \cdot \widehat{s^* \mathbf{v}^*} - \frac{\partial \widehat{s^* \omega^*}}{\partial p}, \tag{1.4}$$

$$\frac{\partial \widehat{Lq}}{\partial t} + \widehat{\mathbf{v}} \cdot \nabla \widehat{Lq} + \widehat{\omega} \frac{\partial \widehat{Lq}}{\partial p} = L(\widehat{e} - \widehat{c}) - \nabla \cdot \widehat{Lq^* \mathbf{v}^*} - \frac{\partial \widehat{Lq^* \omega^*}}{\partial p}, \tag{1.5}$$

where the star mark represents deviation from the horizontal average. Traditionally, the horizontal eddy terms, $\nabla \cdot \widehat{s^* \mathbf{v}^*}$ and $\nabla \cdot \widehat{Lq^* \mathbf{v}^*}$ are ignored, and thus those

equations are written as

$$\frac{\partial s}{\partial t} + \mathbf{v} \cdot \nabla s + \omega \frac{\partial s}{\partial p} = Q_R + L(c - e) - \frac{\partial (s^* \omega^*)}{\partial p}, \tag{1.6}$$

$$\frac{\partial Lq}{\partial t} + \mathbf{v} \cdot \nabla Lq + \omega \frac{\partial Lq}{\partial p} = L(e - c) - \frac{\partial (Lq^* \omega^*)}{\partial p}. \tag{1.7}$$

From now on, we omit the hat from all of the equations for simplicity. But each term should be interpreted as one averaged over a horizontal space.

Now we take a mass-weighted vertical integration from the surface (p_S) to tropopause pressure (p_T). We know that

$$\frac{1}{g} \int_{p_T}^{p_S} L(c - e) dp \simeq LP, \tag{1.8}$$

$$\frac{1}{g} \int_{p_T}^{p_S} \partial (s^* \omega^*) \simeq H, \tag{1.9}$$

$$\frac{1}{g} \int_{p_T}^{p_S} \partial (Lq^* \omega^*) \simeq LE, \tag{1.10}$$

where P is precipitation, H is surface sensible heat flux, and E is surface evaporation. Thus we can write the vertically integrated DSE and moisture equations as

$$\frac{\partial \langle s \rangle}{\partial t} + \langle \mathbf{v} \cdot \nabla s \rangle + \left\langle \omega \frac{\partial s}{\partial p} \right\rangle = \langle Q_R \rangle + LP + H, \tag{1.11}$$

$$\frac{\partial \langle Lq \rangle}{\partial t} + \langle \mathbf{v} \cdot \nabla Lq \rangle + \left\langle \omega \frac{\partial Lq}{\partial p} \right\rangle = LE - LP, \tag{1.12}$$

where

$$\langle X \rangle \equiv \frac{1}{g} \int_{p_T}^{p_S} X dp. \tag{1.13}$$

Combining Eqs. 1.11 and 1.12 yields

$$\frac{\partial \langle h \rangle}{\partial t} + \langle \mathbf{v} \cdot \nabla h \rangle + \left\langle \omega \frac{\partial h}{\partial p} \right\rangle = \langle Q_R \rangle + LE + H, \tag{1.14}$$

where $h \equiv s + Lq$ is moist static energy (MSE). In each chapter of this dissertation work, we start the argument with Eqs. 1.11, 1.12, and 1.14.

Why is the MSE budget equation useful as a diagnostic tool in the tropics? The first reason is that it is derived from the law of conservation as shown above. It is generally beneficial to investigate any phenomena from a perspective of conserved quantities. But there is another, more crucial reason for the use of the MSE budgets, especially in the tropics.

As briefly mentioned above, atmospheric moisture plays an essential role in tropical convective disturbances. It was Raymond (2000), who first proposed a somewhat speculative hypothesis regarding tropical precipitation and moisture. He hypothesized that tropical precipitation is primarily regulated by the column relative humidity (aka. saturation fraction) that is a ratio of vertically integrated water vapor mixing ratio (known as precipitable water) to vertically integrated saturation mixing ratio. Using satellite data, Bretherton et al. (2004) showed that precipitation over the tropical ocean can be, in a statistical sense, expressed as an exponential function of precipitable water. This indicates that there is a strong positive correlation between tropical precipitation and precipitable water. Indeed,

this moisture-precipitation relationship is ubiquitous over the tropical ocean where convective systems are often embedded in a moisture-rich envelope.

Therefore, for a better understanding of tropical convective disturbances, we need to understand the mechanisms controlling moisture variations. Then, it seems that the vertically integrated moisture budget equation (Eq. 1.12) would be the best choice for diagnoses. However, efforts using this equation are often stymied by the difficult task of quantifying the small moisture tendency ($\partial\langle q\rangle/\partial t$) that is a residual of two predominant processes, vertical moisture advection ($\langle\omega\partial q/\partial p\rangle$) and the loss of water vapor due to precipitation ($-P$). Since these two processes are so dominant, the moisture budget equation is not appropriate for diagnosing moisture variations or behaviors of $\langle q\rangle$. Instead, we can use the column MSE budget equation (Eq. 1.14) for that purpose.

In the tropics, temperature anomalies are small because of weak Coriolis effects. This property was justified by a scale analysis (e.g., Charney, 1963, 1969) and by a cloud resolving model study (e.g., Bretherton and Smolarkiewicz, 1989). By contrast, moisture variations in the tropics are significant. This indicates that the variation of the column DSE tendency ($\partial\langle s\rangle/\partial t$) is much smaller that that of the precipitable water tendency ($\partial\langle Lq\rangle/\partial t$), allowing us to neglect $\partial\langle s\rangle/\partial t$ from the MSE budget equation. Therefore, we can approximate the MSE budget equation as

$$\frac{\partial\langle Lq\rangle}{\partial t} \simeq -\langle \mathbf{v}\cdot\nabla h\rangle - \left\langle \omega\frac{\partial h}{\partial p}\right\rangle + \langle Q_R\rangle + LE + H. \tag{1.15}$$

This equation tells us about the processes associated with the growth and decay of precipitable water. In the following chapters, we will thoroughly investigate this

equation using various observational data sets.

Besides this equation, we will also examine a conceptual quantity called the gross moist stability (GMS). The GMS has been studied in various contexts in the past literature. In the next section, we briefly summarize the concept and history of the GMS.

1.3 GMS mechanics

The GMS is a quantity which represents the efficiency of the advective export of MSE by convectively induced large-scale circulations. This conceptual quantity was originally coined by Neelin and Held (1987) with a simple two-layer atmospheric model as "a convenient way of summarizing our ignorance" about the relationship between moist convection and associated large-scale circulations. Two decades later, Fuchs and Raymond (2007) and Raymond et al. (2007) furthered this idea by defining a relevant quantity called the normalized GMS (NGMS) to include more general atmospheric structures. In this paper, we will use the terms, GMS and NGMS, interchangeably because these two represent the same concept; they both represent the amount of MSE exported by the unit intensity of convection.

The GMS used in this study is defined as

$$\Gamma \equiv \frac{\nabla \cdot \langle h\mathbf{v} \rangle}{\nabla \cdot \langle s\mathbf{v} \rangle}. \tag{1.16}$$

In chapters 3 and 4, we will discuss useful applications of this quantity. But before that, let us briefly explain how this concept has been used in the past literature.

As mentioned above, the GMS was originally developed in the configuration of a two-layer model. This was a reasonable starting point; if a barotropic configuration doesn't work, trying the simplest baroclinic model, which is the two-layer configuration, is absolutely reasonable. In such a configuration, the degrees of freedom of vertical velocity structures is one, defined on a staggered grid. Thus we might be able to call this kind of model a first baroclinic model. What was interesting was that this configuration predicted the reduction of the phase speed of equatorially trapped waves, and the reduced phase speed was proportional to the GMS [see a review paper by Raymond et al. (2009)]. Therefore, it was believed that the GMS explains the coupling between waves and convection. The popularity of this kind of GMS theories, however, has waned because (1) it turned out that the wave structures in the first baroclinic model were so different from the actual structures from observations [refer to a review by Kiladis et al. (2009)], and (2) alternative theories which include a second baroclinic structure explained better the wave dynamics (e.g., Mapes, 2000; Khouider and Majda, 2006; Raymond and Fuchs, 2007; Kuang, 2008b; Herman et al., 2016).

Although this GMS-wave theory became less popular, it does not necessarily mean a denial of the theory. For instance, Frierson et al. (2011) showed that the GMS predicts the reduced phase speed of the Kelvin waves produced in a relatively realistic general circulation model. It has not been elucidated whether this is a providential coincidence or the GMS plays a role in some unknown dynamics. I personally believe that this is still an open question.

Recently, the GMS has gained increasing attention from a different perspective

than the equatorial wave theories. The idea is growing and being accepted that the MJO is a moisture mode (e.g., Neelin and Yu, 1994; Sobel et al., 2001; Sobel and Gildor, 2003; Fuchs and Raymond, 2002, 2005, 2007; Raymond and Fuchs, 2007; Sugiyama, 2009a,b; Sobel and Maloney, 2012, 2013; Adames and Kim, 2016). Detailed discussions about the moisture mode theories are far beyond the scope of this study, thus we will not delve into those. But there is one property that all the theories in the papers listed above consistently possess; all of them state that the moisture mode is destabilized only when the effective GMS (i.e., a version of GMS involving a radiative feedback) is negative. Recent diagnostic studies consider that the GMS (and the effective GMS) might be a useful diagnostic tool for the MJO dynamics (e.g., Ling et al., 2013; Benedict et al., 2014; Hannah and Maloney, 2014; Sobel et al., 2014; Sentić et al., 2015).

In chapters 3 and 4, we will investigate the GMS using field campaign data and satellite data. However, in those chapters, we will look at the GMS from a different perspective from both the equatorial wave theories and moisture mode theories discussed above. Instead, we consider the GMS as a diagnostic tool which can quantify an interaction between moist convection and large-scale circulations. We will propose a novel diagnostic framework which is applicable to all kinds of data set, including satellite, field campaign, reanalysis, and numerical model data. We believe that our GMS diagnoses will facilitate a better understanding of the GMS-related theories.

1.4 Outline

In this dissertation work, we analyze the MSE budgets and GMS from a different aspect from previous studies. Through the whole chapters, we propose new diagnostic frameworks which facilitate a better understanding of the mechanism of an interaction between moist convection and large-scale circulations in the tropical atmosphere.

In chapter 2, we investigate the MSE budgets on different time scales. We utilized a data set collected during a field campaign called TOGA COARE. In that data set, the behaviors of the MSE budgets are examined on four different time scales ($\sim$2-day, $\sim$5-day, $\sim$10-day, and MJO time scales).

In chapter 3, we propose a new diagnostic application of the GMS using the TOGA COARE data set. The GMS can be used as a quantity which represents an interaction between convection and large-scale circulations. In particular, we examine the relationship between convection amplification/decay and vertical velocity profiles through the assessment of the GMS.

In chapter 4, we expand the ideas proposed in chapter 3. We analyze satellite-based products to investigate the behaviors of the GMS over the whole tropical ocean. A novel diagnostic framework called "the GMS plane analysis" is proposed here. We also discuss general misconceptions about the GMS and MSE analyses which can be found in many past MJO studies.

The three chapters of the main body of this thesis consist of three independent publications in peer-reviewed journals. Chapters 2 and 3 were published as Inoue and Back (2015a) and Inoue and Back (2015b), respectively, and are reproduced

with slight modifications in this thesis. Chapter 4 has been submitted to the *Journal of the Atmospheric Sciences*. In chapter 5, we present a summary of all of the chapters.

Chapter 2

Column-Integrated Moist Static Energy Budget Analysis on Various Time Scales during TOGA COARE

2.1 Background

In order to investigate the relationship between tropical convection and its associated large-scale circulations, past work has examined column-integrated moist static energy (MSE) budgets. These budgets tell us about the processes associated with the growth and decay of column MSE. The column MSE is useful as a diagnostic quantity in the deep tropics primarily for two reasons. First, it is approximately conserved in moist adiabatic processes, and it is often beneficial to study any phenomenon from a perspective of conserved variables. Second, the column MSE is tightly connected to tropical convective variability. Column water vapor is known to be closely linked to precipitation anomalies in the tropics (e.g., Raymond, 2000; Bretherton et al., 2004; Neelin et al., 2009; Masunaga, 2012), and

[1]Material in this chapter is a slightly edited version of: Inoue, K., and L. E. Back, 2015: Column-Integrated Moist Static Energy Budget Analysis on Various Time Scales during TOGA COARE. *J. Atmos. Sci.*, **72**, 1856–1871.

temperature anomalies are small due to the large Rossby radius (Charney, 1963, 1969; Bretherton and Smolarkiewicz, 1989; Sobel and Bretherton, 2000). Together, these two constraints mean that the evolution of column MSE is closely related to the evolution of precipitation anomalies. In this work, we explore the charging and discharging mechanisms of column MSE that are associated with precipitation anomalies for various frequencies of variability. To do this, we examine column MSE budgets using data from the Tropical Ocean Global Atmosphere Coupled Ocean-Atmosphere Response Experiment (TOGA COARE; Webster and Lukas, 1992) field campaign.

The column-integrated MSE budget equation is, following Yanai et al. (1973),

$$\frac{\partial \langle h \rangle}{\partial t} = -\langle \mathbf{v} \cdot \nabla h \rangle - \langle \omega \frac{\partial h}{\partial p} \rangle + \langle Q_R \rangle + S, \tag{2.1}$$

where $h \equiv s + Lq$ represents MSE, s represents dry static energy (DSE), L represents the latent heat of vaporization, q represents water vapor mixing ratio, Q_R represents radiative heating rate, S represents surface fluxes of MSE, and the other terms have conventional meteorology meanings. We have neglected a residual due to ice processes. The angled brackets represent a vertical integral over mass in the troposphere. Because in the deep tropics variations in the temperature field are much smaller than those of moisture, variations in h are primarily due to fluctuations of atmospheric moisture. Thus investigating the column h budget leads us to understand how moisture anomalies amplify and decay in the tropics.

Episodes of organized deep convection in the tropics are thought to generally

begin with bottom-heavy diabatic heating[2] that progressively deepens as the convection develops and eventually becomes top-heavy and stratiform. This structure has been seen in convectively-coupled equatorial waves (e.g., Takayabu et al., 1996; Straub and Kiladis, 2003; Haertel and Kiladis, 2004; Haertel et al., 2008; Kiladis et al., 2009), the MJO (e.g., Lin et al., 2004; Kiladis et al., 2005; Benedict and Randall, 2007; Haertel et al., 2008), and even individual mesoscale convective systems (e.g., Mapes et al., 2006). The vertical profile of convection also has a strong impact on numerical simulations of the MJO (e.g., Lin et al., 2004; Fu and Wang, 2009; Kuang, 2010; Lappen and Schumacher, 2012, 2014), convectively-coupled waves (e.g., Cho and Pendlebury, 1997; Mapes, 2000; Kuang, 2008b) and convective organization in general. These phenomena are presently challenging to simulate correctly, which makes numerical weather prediction difficult (e.g., Lin et al., 2006; Kim et al., 2009; Benedict et al., 2013).

Interestingly, bottom-heavy profiles of vertical motion are associated with the import of MSE by the vertical circulation (i.e., negative $\langle \omega \partial h / \partial p \rangle$). These tend to coincide with the build-up of moisture in disturbances. Conversely, top-heavy profiles of vertical motion are associated with the export of MSE by the vertical circulation and these tend to coincide with the decay of moisture in disturbances. This suggests that, as pointed out by Peters and Bretherton (2006), the vertical advection term could be playing a role in the charging and discharging of column MSE associated with disturbances. This was also seen to some degree in recent

[2]Since most of the diabatic heating is balanced by vertical DSE advection and profiles of the DSE are relatively constant in the tropics, structures of the diabatic heating are similar to those of the vertical velocity profiles.

work on the MSE budget during the Dynamics of the Madden Julian Oscillation (DYNAMO) field campaign (Sobel et al., 2014). In this work, we systematically examine the relative contribution of this vertical advective term, as well as other terms to the build-up and decay of column MSE for various frequencies of variability observed during TOGA COARE.

We also examine hypotheses about MJO dynamics that have been emerging from the most recent MJO studies (e.g., Kim et al., 2014; Sobel et al., 2014). That is, 1) the radiative heating and surface fluxes destabilize the MJO disturbance by amplifying and maintaining MJO MSE anomalies while 2) the vertical advection stabilizes the disturbance by exporting MSE, and 3) the horizontal advection plays a significant role in the eastward propagation by building up moist conditions ahead, and providing dry conditions behind the active convective phase. These points are investigated in the MJO events during TOGA COARE.

Neelin and Held (1987) introduced a normalized version of the vertical advective term, known as the gross moist stability, which "provides a convenient way of summarizing our ignorance of the details of the convection and large-scale transients." Other versions of this quantity have been used in many studies (see a review paper by Raymond et al., 2009). In this work, we examine the implications of the bottom-heavy to top-heavy evolution of vertical motion profiles for the gross moist stability. We also briefly discuss an appropriate choice of time filters for investigating relatively high frequency variability in the TOGA COARE data set.

Section 2.2 describes our data and filtering, regression methodology. In section 2.3, we show column-integrated MSE budgets for various time scales of vari-

ability, as well as vertical motion profiles. Section 2.4 has a discussion of gross moist stability and calculations of this quantity. In section 2.5, we discuss the relationship between a constant gross moist stability and the vertical motion structure being well-described by a first baroclinic mode. In this section, we estimate the gross moist stability in a different way from section 2.4 and also briefly discuss sensitivity to our filter choice. In section 2.6, we describe our conclusions.

2.2 Data and Methodology

2.2.1 Data description

We investigated the data associated with the column-integrated moist static energy budget equation during the Tropical Ocean Global Atmosphere Coupled Ocean-Atmosphere Response Experiment (TOGA COARE; Webster and Lukas, 1992). TOGA COARE is a package of various field experiments conducted in the western equatorial Pacific. The experiment provided detailed observations of the mean and transient states of the tropical variability in the western Pacific warm pool, enabling identification of the dominant dynamical and thermodynamic processes in large-scale tropical convective systems. We utilized the data during the Intensive Operative Period (IOP) starting from 1 November 1992 to 28 February 1993 with 6 hourly time resolution. Each variable was averaged over the spatial domain called the Intensive Flux Array [IFA; see Fig. 14 in Webster and Lukas (1992)].

The data set we used was objectively constructed by Minghua Zhang, who used constrained variational analysis for producing each variable. That method

guarantees the conservation of the column-integrated mass, water, and DSE. See Zhang and Lin (1997) for more detailed description about the constrained variational analysis.

2.2.2 Selection of time scales

For examining the column MSE budgets and associated terms for different frequencies of variability, we chose four time scales, ∼2 day, ∼5 day, ∼10 day, and MJO (>20 day) time scales. Those time scales are chosen based on a power spectrum of the precipitation during TOGA COARE and previous TOGA COARE studies. Figure 2.1a shows the power spectrum of the precipitation. Since the purpose of this study is not to investigate spectral signals which have been already examined by many previous studies, we will not look at statistical robustness of the signals in the power spectrum. We will use this power spectrum just for the purpose to determine which time scales should be separated to be investigated.

Figure 2.1a shows there are four peaks with different periodicities. The first one is the diurnal cycle which is not of our interest in this study, thus was removed by filtering in the analysis. The second peak can be found around 2 day period. This signal has been investigated by Takayabu et al. (1996) and Haertel and Kiladis (2004), who have pointed out that there exist westward propagating 2-day inertia gravity waves during TOGA COARE. Thus we dealt with this time scale separately. The other signals are found around 4∼5 day and 10∼13 day periods, which could be Kelvin wave signals. Because those two are obviously distinct and different from the 2-day wave signal, we also examined those time scales separately. Because the

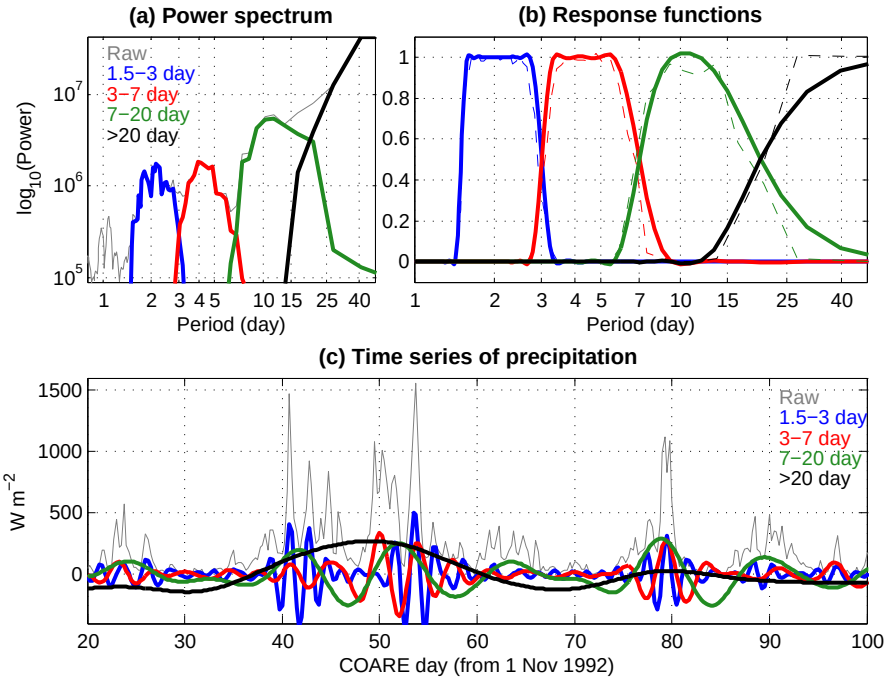

Figure 2.1: (a): Power spectra of raw and filtered precipitation. Raw, ∼2 day, ∼5 day, ∼ 10 day, and >20 day (MJO) time scales are illustrated in gray, blue, green, and black lines, respectively. (b): Response functions of Lanczos filters with different cut-off frequencies. The colors are arranged in the same way as (a). Thick solid lines represent theoretical responses of the filters and thin dash lines show computed responses from the precipitation spectra. (c): Time series of raw and filtered anomalous precipitation. The black line shows two MJO events during TOGA COARE.

signal of 10∼13 day period in the power spectra is much smaller than the other signals, we cannot negate the possibility that the signal here is just a statistical noise. Nevertheless, we investigate this signal in order to keep consistency with Mapes et al. (2006), who have also investigated this periodicity in the TOGA COARE data set. Finally, the MJO time scale was extracted because many previous studies have shown there are two MJO events during TOGA COARE (e.g., Velden and Young,

1994; Lin and Johnson, 1996; Yanai et al., 2000; Kikuchi and Takayabu, 2004) in late November to December (around 30 to 65 COARE day) and in Feburary (around 70 to 100 COARE day). Because the second MJO signal was attenuated before reaching the IFA [see Fig. 3 in Yanai et al. (2000)], most of the features in the following analyses on the MJO time scale reflect the structures of the first MJO event.

2.2.3 Filtering

In order to extract different time scale features, a Lanczos filter was utilized. This filter has been popularly used in meteorology and other areas because the responses of frequencies to the filter has been well-studied (Duchon, 1979); it has desirable behaviors with minimum Gibbs oscillations and relatively sharp cut-off slopes which prevent frequencies of interest from being contaminated by undesirable leakage of frequencies and artificial false responses produced by the Gibbs oscillations. We will briefly discuss sensitivities of the results to the choice of filtering in section 2.5.2, where we will compare the Lanczos filter with a running mean filter, especially on short time scales.

There is a common trade-off between the number of weightings, or the number of data points which have to be sacrificed, and desirable behaviors of the filter. We chose 151 as the number of the weightings for all the analyses. This number was chosen in such a way that the response function of the filter looks appropriate enough to separate the MJO signals from the other shorter time scale signals (see Fig. 2.1b). Although we could have used a smaller number for the analyses on the shorter time scales ($\sim$2 day and $\sim$5 day scales) for reducing sacrificed points, we

used the same number for all the analyses. We tried different numbers of weightings, and found those didn't make significant changes in the results. Figure 2.1c shows time-series of the raw and filtered precipitation. We can see one strong MJO signal from around 30 November 1992 to 3 January 1993 (from 30 to 65 COARE day) and one weak signal from around 8 January to 7 Feburary 1993 (from 70 to 100 COARE day).

2.2.4 Regression analysis and correlation test

Variability on the different time scales was plotted using a linear lag-regression analysis. This method has been used by many studies (e.g., Kiladis and Weickmann, 1992; Mapes et al., 2006). In this analysis, a predictand is regressed against a predictor (or a master index) to determine regression slopes at different lag times. These computed regression slopes are scaled with one standard deviation of the predictor so that the computed regression slopes have the same unit as that of the predictand. We chose precipitation as the predictor, and each variable in Eq. 3.6 as a predictand. We also computed the vertical structures of the regression slopes of vertical pressure-velocity (omega), wind divergence, and mixing ratio on the different time scales as in Mapes et al. (2006). Those slopes were computed at each lag time and each height. Both the predictor and predictands were filtered with a Lanczos filter for statistical correlation tests. (For a regression analysis, predictands don't need to be filtered.)

Statistical correlation tests were applied to test whether a given feature is statistically significant. Degrees of freedom (DOF) for the correlation tests were estimated

at each lag and height following Bretherton et al. (1999). Although the values of the estimated DOF vary among different grids and variables, those variations are small enough that we neglect them. The DOF on ∼2 day time scale is about 102 (this is an average value of the different values of the DOF) and the DOF on ∼5 day time scale is about 22. On ∼10 day time scale, the number of different realizations (convection) can be counted in Fig. 2.1c and it is about 6, thus the DOF for the correlation test on this time scale is 4. For the MJO time scale, there are only two independent events. Since those numbers of the independent samples on 10 day and the MJO time scales are too small to do statistical tests, statistical significance was tested only on ∼2 day and ∼5 day time scales.

2.3 Results: Column MSE budgets and omega profiles

2.3.1 Column MSE budgets

In the top panels of Fig. 2.2, plotted are lag auto-correlations of precipitation, lag correlations between precipitation and column-integrated MSE, and in the bottom panels, lag regression slopes of each term in Eq. 3.6 regressed against the precipitation and scaled with one standard deviation of the precipitation on the different time scales. The standard deviations of raw data, ∼2 day, ∼5 day, ∼10 day, and MJO time scales, are respectively 229 W m^{-2}, 112 W m^{-2}, 91 W m^{-2}, 121 W m^{-2}, and 123 W m^{-2}. Every variable is filtered with a Lanczos filter on the corresponding time scales. Confidence intervals of the 90% significant level of the regression

slopes are also plotted on the left bottom corners only on ∼2 day and ∼5 day time scales on which we can get enough DOF. The values of confidence intervals differ at different lags, thus average values among the lag time windows are plotted. The numbers on the right corners of each subplot are average values (among the lag time windows) of the numbers of the independent samples. Increased errors on ∼5 day time scale compared to ∼2 day time scale are primarily due to the reduced DOF.

We first acknowledge that due to the lack of DOF we are uncertain about whether or not Figs. 2.2c and 2.2d represent statistically significant features of the MSE budgets on those time scales. To examine statistical significance on those time scales, we need to investigate longer time-series than the TOGA COARE data, which is left for future work. Nevertheless, we can see that the patterns in Fig. 2.2d for the MJO events during TOGA COARE are similar to those in Fig. 10 in Benedict et al. (2014) in which 10 year long ERA-interim, TRMM precipitation, and objectively analyzed surface flux data were investigated.

Column-integrated radiative heating $\langle Q_R \rangle$ is approximately in phase with the precipitation (or the precipitation leads slightly) on all the time scales. Surface fluxes S lag the precipitation peaks on all the time scales except for ∼10 day scale on which both radiative heating and surface fluxes are nearly in phase with the precipitation. The lags of S are significant on ∼5 day and MJO time scales (>20 day).

The behaviors of column-integrated vertical MSE advection (or $-\langle \omega \partial h/\partial p \rangle$) differ among the time scales. On ∼2 day scale, positive advection (i.e., $-\langle \omega \partial h/\partial p \rangle >$

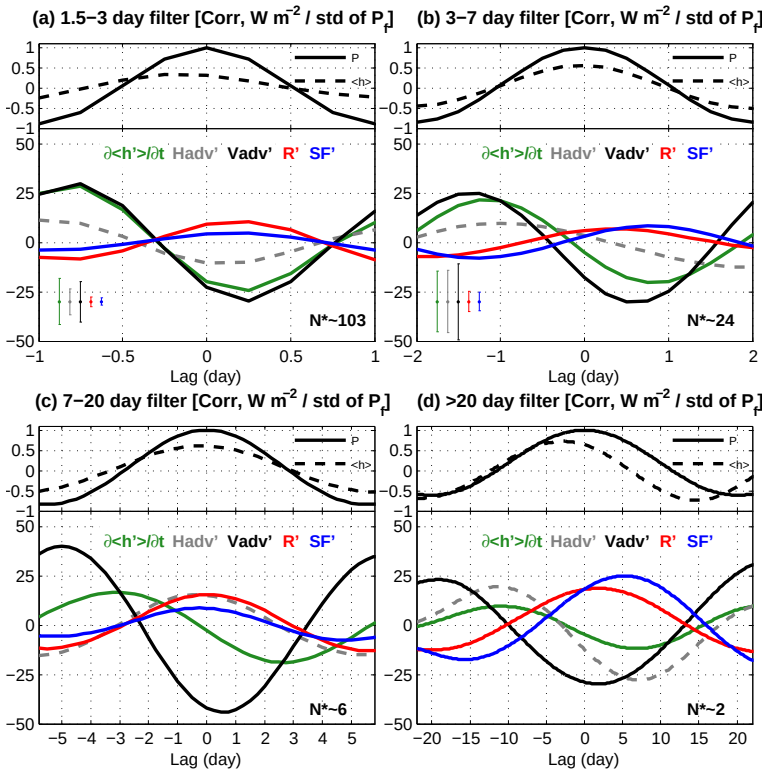

Figure 2.2: (Top panels): Lag auto-correlations of filtered precipitation (solid lines) and lag correlations between filtered precipitation and filtered column MSE (dash lines) on the four different time scales. (Bottom panels): Regression slopes of anomalies of $\partial\langle h\rangle/\partial t$ (green), $-\langle \mathbf{v}\cdot\nabla h\rangle$ (gray dash), $-\langle \omega\partial h/\partial p\rangle$ (black), $\langle Q_R\rangle$ (red), and S (blue), regressed against filtered precipitation and scaled with one standard deviation of the filtered precipitation on the different time scales. The precipitation was filtered with (a) 1.5∼3 day band-pass, (b) 3∼7 day band-pass, (c) 7∼20 day band-pass, and (d) >20 day low-pass filters. The error bars on the left bottom corners in (a) and (b) represent average values (among the lag time windows) of significant errors for each MSE budget term computed with 90% significant level. The numbers on the right bottom corners show estimated independent sample sizes on the different time scales.

0, or import of h) leads the precipitation, and the minimum value (i.e., maximum export of h) lags the precipitation peak. The tendency of column-integrated h (or

$\partial\langle h\rangle/\partial t$) agrees with the vertical advection term, which implies that on this time scale most of the recharge-discharge cycle of h is explained by the vertical advection while the other terms cancel out each other.

On the $\sim$5 day scale, the pattern of vertical advection term is similar to that of $\sim$2 day scale in which positive advection leads the precipitation and negative advection lags the precipitation peak. Unlike the $\sim$2 day scale, there is a lag between the vertical advection and tendency term on this time scale which is due to negative contributions of the radiative heating and surface fluxes in the early stage of the convection. This lag between the vertical advection and tendency term becomes larger as the time scale gets longer.

On the $\sim$10 day scale, the maximum vertical advection leads the tendency maximum by around 3 days. Furthermore, the relative amplitude of vertical advection to the tendency term becomes greater on this time scale, which is due to the other terms that work in the opposite way to the vertical advection. That is, in the early stage of the convection the vertical advection recharges h while the other terms discharge h and in the mature stage the vertical advection exports h while the other terms recharge it.

On the MJO time scale, akin to $\sim$10 day scale, the positive vertical advection leads the positive tendency term and amplitude of the vertical advection is greater than that of the tendency term because the other terms play significant roles in the h budgets. It is also worthwhile to note that as the time scale gets longer the vertical advective export of MSE (i.e., $+\langle\omega\partial h/\partial p\rangle$) becomes more in phase with precipitation peak (i.e., the lag relation becomes closer to 180 degree out of phase). On $\sim$2 day and

$\sim$5 day time-scales the vertical advective h export lags the precipitation peak, while on $\sim$10 day and the MJO time scale it becomes more in phase with the precipitation peak. This in-phase h export pattern has implications when we consider the gross moist stability (GMS), which will be discussed in section 2.4.2.

The horizontal advection (i.e., $-\langle \mathbf{v} \cdot \nabla h \rangle$) exhibits significantly different behaviors among these different frequencies. On $\sim$2 day scale, the positive horizontal advection leads the precipitation and the minimum value reaches slightly after the precipitation peak. The horizontal advection acts in almost opposite ways to the radiative heating and surface fluxes. As a result, those terms cancel out each other. On $\sim$5 day scale, the horizontal advection is almost 90 degree out of phase with the precipitation. In contrast, on the $\sim$10 day scale it is almost in phase with the precipitation. Again, since Fig. 2.2c contains only 6 independent samples we cannot conclude that this pattern is statistically robust. More detailed investigations should be done on this time scale in future work. On the MJO time scale, the horizontal advection is 90 degree out of phase with the precipitation. Before the precipitation peak the horizontal advection imports h while after the precipitation maximum it exports h. As the time scale gets longer, the amplitude of the variations of the horizontal advection become greater, which might indicate that the relative contribution of the horizontal advection to the recharge and discharge of the MSE becomes more important as the time scale gets longer.

The relative amplitudes of the differnt terms indicate which terms are the most important for these frequencies. For all the frequencies except for the MJO, the vertical advection dominates the other terms which implies that the vertical advection

is the most important h sink and source. At longer time scales of variability (lower frequencies), however, the amplitude of the vertical advection term relative to the source/sink terms becomes less. On the MJO scale, the horizontal and vertical advection, radiative heating, and surface fluxes all have relatively similar amplitudes. That indicates that all the terms in the MSE budgets play important roles in the MJO dynamics.

Furthermore, the results shown in Fig. 2.2d on the MJO time scale reinforce the view of the MJO dynamics which has been emerging from recent studies (e.g., Kim et al., 2014; Sobel et al., 2014). That is, 1) the radiative heating and surface fluxes amplify and maintain the MJO MSE anomalies while 2) the MJO disturbance is stabilized by the vertical advection which exports MSE and cancels the effect of the radiative heating and surface fluxes, and therefore 3) the eastward propagation of the MJO is primarily driven by the horizontal advection which provides moistening ahead (in the negative lags, or to the east of), drying behind (in the positive lags, or to the west of) the active convective phase. Although there are differences between the different MJO events as pointed out by Sobel et al. (2014), our results, in general, show significant consistencies with the results given by Kim et al. (2014) and, to some degree, with the results in Sobel et al. (2014).

2.3.2 Omega profiles

Figure 2.3 shows vertical structures of vertical pressure velocity (omega) and wind divergence on the different time scales. The areas surrounded by the green curves passed statistical correlation tests with 99% (on $\sim$2 day time scale) and 80% (on

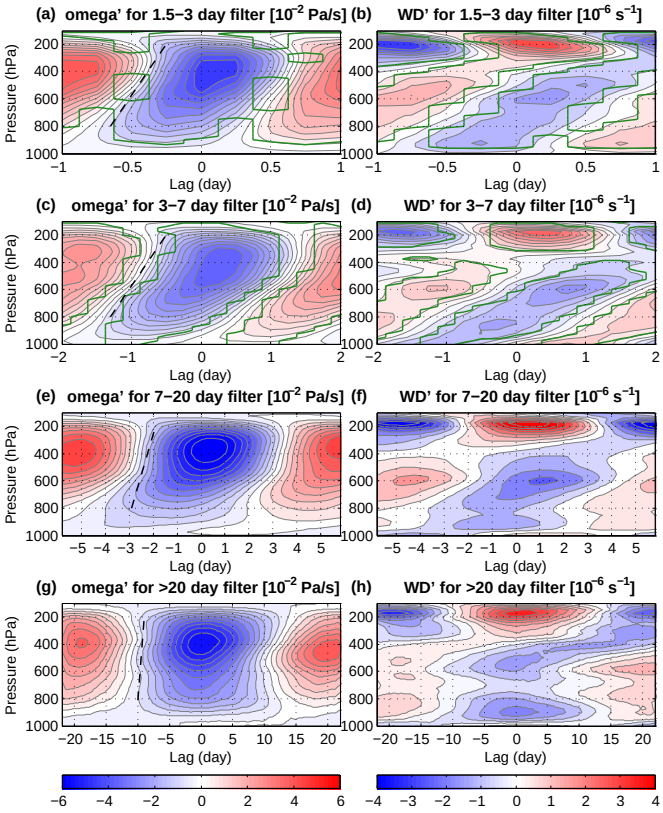

Figure 2.3: Vertical structures of anomalous omega and wind divergence fields regressed against the filtered precipitation and scaled with one standard deviation of the filtered precipiation on ∼2 day (a and b), ∼5 day (c and d), ∼10 day (e and f) and >20 day (g and h) scales. The contour interval of the omega plots is $0.6*10^{-2}$ Pa/s, and that of the wind divergence plots is $0.5*10^{-6}$ s^{-1}. The areas surrounded by the green lines in the top two row panels correspond to the grids which passed correlation significance tests with 99% (on ∼2 day scale) and 80% (on ∼5 day scale) significant levels. The black dash lines illustrate tilting structures of the omega profiles on each time scale.

∼5 day time scale) significant levels. The lower significant level used on ∼5 day time scale is because of smaller DOF on this time scale compared to ∼2 day time scale. The statistical tests were not applied for ∼10 day and the MJO time scales due to the lack of DOF. As Mapes et al. (2006) showed, we can observe tilting

structures of the omega profiles in which the profile evolves from a bottom-heavy shape into a top-heavy shape (indicated by the black dash lines), and these tilting structures are statistically significant. The figures of the wind divergence illustrate the same information as the omega figures. Height of the lower tropospheric convergence (blue shaded contours) rises as the convection develops, making the tilting divergence profiles.

However, one can notice that the tilt of the omega profile becomes steeper as the time scale gets longer. Especially, on the MJO time scale, the contour line of the omega is almost perpendicular to the isobaric surface at -10 lag day. There is a shallow convective phase on this scale, too (see from -22 to -12 lag days), but this shallow convection is more abruptly changed into deep convection compared to those on the shorter time scales in which the transitions of the convection from a bottom-heavy to a top-heavy shape happen more gradually. The divergence figures depict the differences among the time scales clearly. In the upper troposphere, the structures are qualitatively similar among the different time scales. In the inactive stage of the convection, strong convergence associated with upper tropospheric descending motion happens at the top of the troposphere. In the mature stage of the convection, in contrast, strong divergence due to deep convection happens.

In the lower half of the troposphere, differences among the time scales are prominent. On all the time scales except for the MJO time scale, in the inactive convective stage, the strongest divergence happens around 600 hPa. On the MJO time scale, in contrast, the divergence at this level is much weaker than that on the shorter time scales, and the strongest divergence happens around 900 hPa. This

lower tropospheric divergence maintains its strength until -15 lag day. As this lower tropospheric divergence disappears, the convection abruptly changes into deep convection. Therefore, on the MJO time scale, the omega profiles behave like a single deep convection mode which is often called a first baroclinic mode. This omega behavior has implications regarding the gross moist stability (GMS) of the convective system.

Before going to the next section, it should be emphasized again that the results shown in Figs. 2.3g and h reflect only two MJO events, one of which is a weak event, and thus it is almost a case study. Therefore, it is difficult to draw a general conclusion about the MJO structures from our analysis particularly because the details of the MJO structures differ significantly from event to event. However, we can at least claim that a strong tilt of the omega profile (or latent heating profile) is not necessary for the existence of the MJO even though the tilt might play a role in the MJO dynamics.

Furthermore, it should also be noted that our lag-regression methodology extracted the actual structures of the MJO event during TOGA COARE in an appropriate way. Figure 2.4 shows the time-height plot of the anomalous omega of the first MJO event during TOGA COARE, which occurs between $\sim$30 COARE day and $\sim$65 COARE day. In this plot, we simply utilized a 15-day running mean filter. Although the contour is noisy due to the noise introduced by the running mean filter, the overall structure is similar to that in Fig. 2.3g. This figure indicates that our methodology captures the MJO structures well, and negates the possibility that the result shown in Fig. 2.3g is due to a false signal introduced by the statistical method.

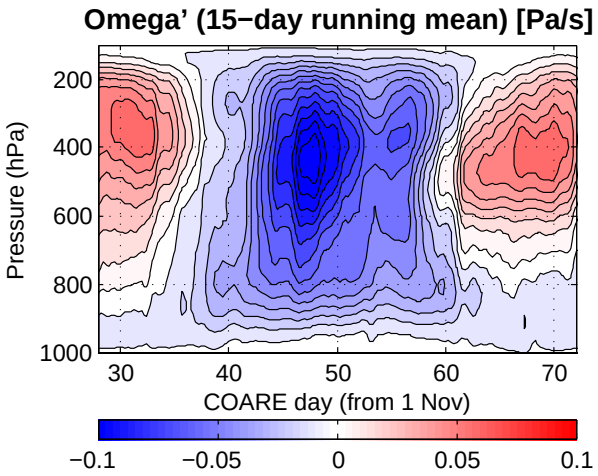

Figure 2.4: Anomalous omega profiles of the first MJO event during TOGA COARE with a 15-day running mean filter. The contour interval is 0.01 Pa/s.

2.4 More results: Gross moist stability

2.4.1 GMS with different frequencies

Now the gross moist stability (GMS) on the different time scales will be computed. Before doing actual computations, the concept of the GMS needs to be clarified. The GMS, which is a concept originated by Neelin and Held (1987), represents the efficiency of MSE export by convectively induced large-scale circulations. Raymond et al. (2009) defines a relevant quantity called normalized GMS (NGMS), which is a ratio of column MSE (or moist entropy) advection to intensity of the convection. Although different authors have used slightly different definitions of the NGMS (e.g., Fuchs and Raymond, 2007; Raymond and Fuchs, 2009; Raymond et al., 2009; Sugiyama, 2009a; Andersen and Kuang, 2011), the physical implications behind those definitions are consistent in such a way that the NGMS represents efficiency

of export of some intensive quantity conserved in moist adiabatic processes per unit intensity of the convection (Raymond et al., 2009). We employ one version of the NGMS defined as

$$\Gamma = \frac{\langle \mathbf{v} \cdot \nabla h \rangle + \langle \omega \frac{\partial h}{\partial p} \rangle}{\langle \mathbf{v} \cdot \nabla s \rangle + \langle \omega \frac{\partial s}{\partial p} \rangle}, \tag{2.2}$$

where h and s represent MSE and DSE, respectively. Since in the tropics, horizontal temperature gradients are negligible (weak temperature gradient; Sobel and Bretherton, 2000), neglecting the horizontal DSE advection in the denominator yields

$$\Gamma = \frac{\langle \mathbf{v} \cdot \nabla h \rangle + \langle \omega \frac{\partial h}{\partial p} \rangle}{\langle \omega \frac{\partial s}{\partial p} \rangle}. \tag{2.3}$$

Equation 2.3 can be separated into horizontal and vertical components as

$$\Gamma = \Gamma_H + \Gamma_V, \tag{2.4}$$

where

$$\Gamma_H = \frac{\langle \mathbf{v} \cdot \nabla h \rangle}{\langle \omega \frac{\partial s}{\partial p} \rangle},$$

$$\Gamma_V = \frac{\langle \omega \frac{\partial h}{\partial p} \rangle}{\langle \omega \frac{\partial s}{\partial p} \rangle}.$$

In some NGMS studies, the vertical component of the NGMS Γ_V is simply called NGMS (or GMS) (e.g., Sugiyama, 2009a; Kuang, 2010; Andersen and Kuang, 2011; Sobel and Maloney, 2012) while in the others, the horizontal component Γ_H is explicitly defined (e.g., Raymond and Fuchs, 2009; Raymond et al., 2009; Benedict et al., 2014; Hannah and Maloney, 2014; Sobel et al., 2014). Γ_V has been

used in various ways such as a diagnostic quantity in general circulation models (e.g., Frierson, 2007; Hannah and Maloney, 2011, 2014; Benedict et al., 2014), in observational data (e.g., Yu et al., 1998; Sobel et al., 2014)[3], as an output quantity of a MJO toy-model (e.g., Raymond and Fuchs, 2009), and as an input parameter of a MJO toy-model (e.g., Sugiyama, 2009a; Sobel and Maloney, 2012, 2013). As Hannah and Maloney (2011) and Masunaga and L'Ecuyer (2014) pointed out, values of Γ_V generally fluctuate in convective life-cycles primarily due to variations of vertical velocity profiles (as seen in Fig. 2.3). Nevertheless, when used as an input parameter of a toy-model, Γ_V is assumed to be a constant in the convective life-cycle (e.g., Sugiyama, 2009a; Sobel and Maloney, 2012). Furthermore, time-dependent fluctuations of the NGMS are also neglected when the NGMS is computed based on scatter plots between the numerator and denominator of the NGMS, which is one of the most general methods to compute the NGMS.

When considering the NGMS on different time scales in data, we have to be careful about its interpretation. First of all, we can define a mean NGMS, in which we average the numerator and the denominator of Γ before taking the ratio. This is in keeping with the spirit of the definition. We can also define an anomalous NGMS, in which perturbations from the means of numerator and denominator are taken and the ratio of these perturbations is computed. Similarly, we can define a total NGMS [4]. It can be easily shown that the total NGMS is a constant if and only if the mean NGMS is equal to the anomalous NGMS. In many of previous studies,

[3] In Yu et al. (1998), the computed quantity was GMS, and not normalized one.

[4] The phrase "total NGMS" is often used to refer to the combination of Γ_H and Γ_V. In this study, we use the phrase "total NGMS" to refer to the combination of anomaly and mean state. Γ_H plus Γ_V is simply called NGMS or Γ in this paper.

the total NGMS has been assumed to be constant. In such cases, one doesn't have to worry about the differences between the mean and anomalous NGMS. But when considering the total NGMS as a time-dependent variable, one should clarify which kinds of NGMS are being used, mean, anomalous, or total NGMS.

Furthermore, we can generalize the idea of the decomposition of the NGMS from an aspect of Fourier transformation. By taking Fourier decomposition, Eq. 3.6 can be separated into

$$\frac{\partial \langle h \rangle_i}{\partial t} = -\langle \mathbf{v} \cdot \nabla h \rangle_i - \langle \omega \frac{\partial h}{\partial p} \rangle_i + \langle Q_R \rangle_i + S_i, \tag{2.5}$$

where subscripts represent a specific range of frequencies. For instance, $i = 0$ can be defined as the mean state, and $i = ISO$ can be defined so that Eq. 2.5 represents intra-seasonal oscillations as in Maloney (2009). Therefore, we can define the NGMS on different time scales as

$$\Gamma_i = \frac{\langle \mathbf{v} \cdot \nabla h \rangle_i + \langle \omega \frac{\partial h}{\partial p} \rangle_i}{\langle \omega \frac{\partial s}{\partial p} \rangle_i}. \tag{2.6}$$

The horizontal and vertical components on different time scales can be defined similarly to Eq. 3.16.

Interpretations of the sign of the NGMS also require some attentions. When dealing with band-pass filtered variability, the denominator of Eq. 2.6 represents anomalous quantities which can be both positive and negative. With a positive denominator (this is a usual case when convection is active), positive/negative NGMS corresponds to export/import of the MSE. But, when the denominator is

negative (or when convection is inactive), the interpretation must be reversed; that is, a positive/negative value corresponds to import/export of the MSE.

2.4.2 NGMS during TOGA COARE

We estimated the time-dependent NGMS on the four different time scales using Eq. 2.6. Figure 2.5 shows the lag regression slopes of horizontal (blue), vertical (red), and combined (green) column-integrated MSE advection as a function of lag regression slopes of column-integrated vertical DSE advection on the different time scales. The elliptic shapes illustrate life-cycles of convection in which each life-cycle starts from the filled circle, going around counterclockwise, and terminates at the filled square. Γ_H, Γ_V, and Γ at different convective phases can be estimated by computing the slopes of the lines which are drawn from the origin to the periphery of the elliptic shapes. For instance, on $\sim$2 day scale, Γ_V starts with a positive value ($\sim$0.2) which becomes larger and goes infinity (this corresponds to the singularity of the NGMS). After passing through the singular point, it becomes negative which grows into a positive value and reaches about 0.2 again at the peak of the convection. After the convective peak, Γ_V increases and becomes infinity again at the singular point, followed by negative values.

One conclusion we can draw from Fig. 2.5 is that the NGMS and all the components are not constant values on all the time scales, but they vary along the convective life-cycle. But we can find that as the time scale gets longer the vertical NGMS Γ_V converges to a constant value around 0.2, which is the slope of the major axis of the elliptic shape. On the MJO time scale, the elliptic shape of

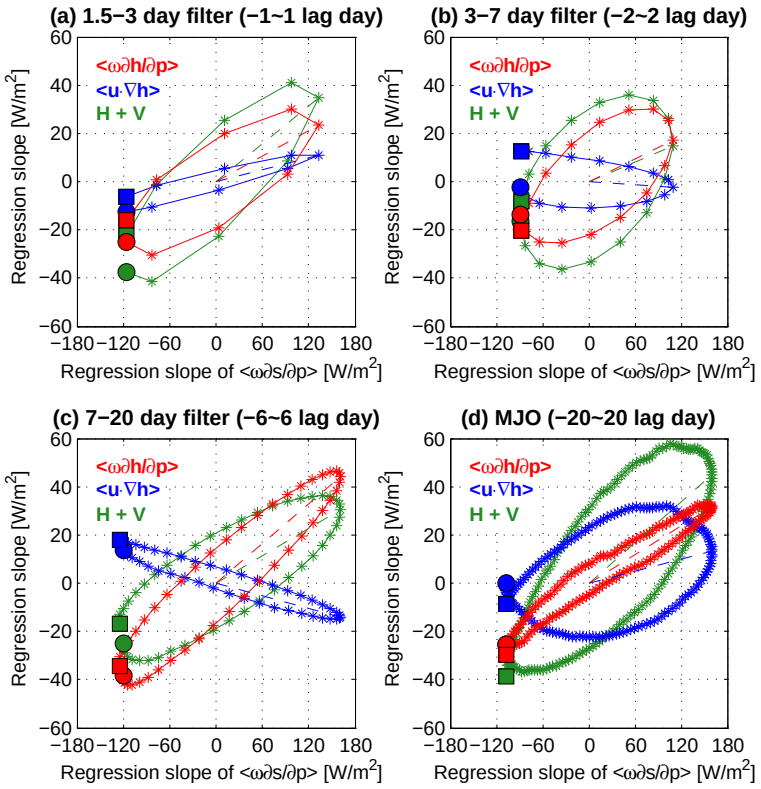

Figure 2.5: Scaled lag regression slopes of vertical MSE advection (red), horizontal MSE advection (blue), and combination of those (green) during convective life-cycles as functions of scaled lag regression slopes of vertical DSE advection on different time scales [(a)–(d)]. Each convective life-cycle starts from the filled circle, going around counterclockwise and terminates at the filled square. The dash lines illustrate Γ, Γ_H, and Γ_V at the precipitation peaks on the different time scales which can be computed as the slopes of those lines.

the vertical MSE advection becomes very close to a linear shape (i.e., constant Γ_V) with the minor axis collapsed. This more-constant Γ_V is related to the fact that the column-integrated vertical MSE advection becomes closer to 180 degree out of phase (negatively in phase) with the precipitation as the time scale gets longer. This indicates that on longer time scales, the column-integrated vertical MSE ad-

vection is more linearly correlated to the precipitation. This result might support one of the popular usages of Γ_V in a MJO toy-model in which Γ_V is assumed be a time-independent quantity (e.g., Sugiyama, 2009a; Sobel and Maloney, 2012).

Compared with the vertical advection, the horizontal advection doesn't have a consistent pattern among the different time scales. On $\sim$2 day scale, the major axis of the ellipse of the horizontal advection has a positive slope while on $\sim$5 day scale the slope is almost zero. In contrast, on $\sim$10 day scales, it has a negative slope. On the MJO scale, its slope is slightly positive, but the values of Γ_H vary significantly during the convective life-cycle. As a result, the NGMS Γ (combination of Γ_H and Γ_V) also varies significantly during the convective life-cycles on all the time scales. It should also be noted that the elliptic patterns of Γ are more similar to those of Γ_V than those of Γ_H on all the time scales except for the MJO time scale.

2.5 Discussion

2.5.1 Omega profiles and Γ_V

Most of the variations in $\langle \omega \partial h / \partial p \rangle$ are explained by the variations of the omega profiles (94% of the total variance in the TOGA COARE data), and the variations of the MSE profiles play a small role. We can use the assumption that omega profiles can be approximated by two dominant modal structures to reason about the importance of each mode for the column MSE budget. We assume

$$\omega(t,p) \approx o_1(t)\Omega_1(p) + o_2(t)\Omega_2(p), \tag{2.7}$$

where Ω_1 and Ω_2 are often called first and second baroclinic modes, respectively, and o_1 and o_2 represent the time-dependent amplitudes of those modes. These could be any two modes which do a good job of describing the variability in vertical motion profiles, like those that come from an EOF analysis of vertical motion profiles. In the TOGA COARE data, the first EOF explains 71% of the variance, and the second EOF explains 21% of the total variances of the omega profiles.

If we neglect the variations of the MSE profiles, we can represent Γ_V as

$$\Gamma_V \approx \frac{o_1\langle\Omega_1\frac{\partial\bar{h}}{\partial p}\rangle + o_2\langle\Omega_2\frac{\partial\bar{h}}{\partial p}\rangle}{o_1\langle\Omega_1\frac{\partial\bar{s}}{\partial p}\rangle + o_2\langle\Omega_2\frac{\partial\bar{s}}{\partial p}\rangle}, \tag{2.8}$$

where the bars represent the time averages.

In general, the MSE and DSE profiles, Ω_1 and Ω_2 chosen via EOF, have the structures as shown in the schematic figure, Fig. 2.6. In the first baroclinic system, convergence happens in the lower troposphere where the DSE is poor and divergence happens in the upper troposphere where the DSE is rich. Hence, in this system, strong net export of DSE happens (i.e., $\langle\Omega_1\partial\bar{s}/\partial p\rangle$ is positive and large). In contrast, in the second baroclinic system, convergence happens both in the lower and upper troposphere where the DSE is poor and rich, respectively, and divergence happens in the middle troposphere where the DSE is moderate. As a result, the upper tropospheric net import of DSE is canceled out by the lower tropospheric net export of DSE, causing small value of $\langle\Omega_2\partial\bar{s}/\partial p\rangle$. Consequently, the value of

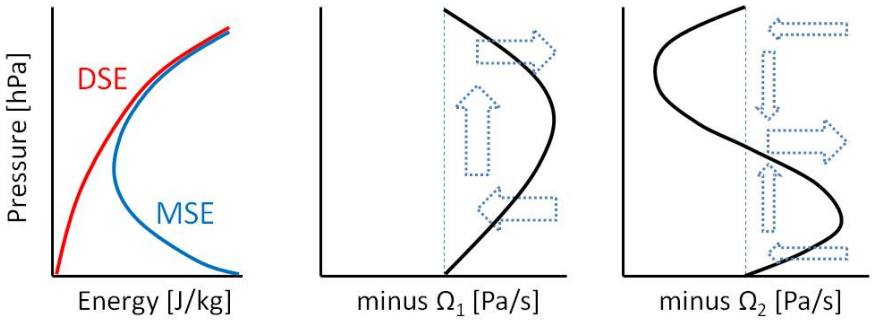

Figure 2.6: Schematic figures of typical DSE and MSE profiles and shapes of the two dominant modes, Ω_1 and Ω_2. Arrows illustrate air flows of convection and associated large-scale circulations. Leftward (rightward) arrows correspond to convergence (divergence).

$\langle \Omega_1 \partial \bar{s}/\partial p \rangle$ is much larger than $\langle \Omega_2 \partial \bar{s}/\partial p \rangle$. Neglecting $\langle \Omega_2 \partial \bar{s}/\partial p \rangle$ in Eq. 2.8 yields

$$\Gamma_V \approx \frac{\langle \Omega_1 \frac{\partial \bar{h}}{\partial p} \rangle}{\langle \Omega_1 \frac{\partial \bar{s}}{\partial p} \rangle} + \frac{o_2}{o_1} \frac{\langle \Omega_2 \frac{\partial \bar{h}}{\partial p} \rangle}{\langle \Omega_1 \frac{\partial \bar{s}}{\partial p} \rangle}. \tag{2.9}$$

This equation shows that for this set of assumptions, time-dependent fluctuations of Γ_V are due to the second term in the rhs of Eq. 2.9, which is the ratio of the amplitude of the second mode to that of the first mode times the ratio of the gross moist stability due to the second mode to the gross dry stability (the denominator of Γ_V; Yu et al., 1998) due to the first mode. In general, $\langle \Omega_2 \partial \bar{h}/\partial p \rangle$ is negative and large while $\langle \Omega_1 \partial \bar{h}/\partial p \rangle$ is positive and small (based on Fig. 2.6 and similar arguments to those for the gross dry stability $\langle \Omega_1 \partial \bar{s}/\partial p \rangle$ and $\langle \Omega_2 \partial \bar{s}/\partial p \rangle$). Thus, for this set of assumptions, the second term in the rhs of Eq. 2.9 is responsible for negative Γ_V in the early stage of the convection, as pointed out by Hannah and Maloney (2011) and Masunaga and L'Ecuyer (2014). This term is also responsible for the nonlinearity

of the vertical MSE advection with respect to the convection, making the elliptic trajectories in Fig. 2.5. If this time-dependent term disappears, Γ_V given by Eq. 2.9 is the homomorphism of the GMS given by Neelin and Held (1987).

In Fig. 2.3, we showed that as the time scale gets longer, the tilting structure of the omega profile becomes less prominent. This disappearance of tilt is likely due to smaller contributions of the second baroclinic mode on longer time scales compared to those on shorter time scales. This indicates that the second term in the rhs of Eq. 2.9 becomes smaller as the time scale gets longer, making Γ_V a more time-independent quantity. On shorter time scales where the second baroclinic mode is prominent, in contrast, the time-dependent term in Eq. 2.9 is robust, hence Γ_V on those time scales varies significantly in the convective life-cycles.

Some studies have argued for an important role of shallow convection in the convective variability including the MJO in which shallow convection enhances moisture import via enhanced surface convergence, and thus amplifies the convective system (e.g., Wu, 2003; Kikuchi and Takayabu, 2004). In our results, although it was less significant than the deep convective profile, a shallow convective phase can be observed even on the MJO time scale. That shallow convection could play a role in the MJO dynamics.

Interestingly, the elliptic trajectories shown in Fig. 2.5 have been already pointed out by Masunaga and L'Ecuyer (2014), who investigated the MSE budgets and computed the time-evolution of the NGMS on short time scales using the satellite data sets. There are a few notable differences between our analysis and their study. First, they used a different NGMS definition, which is a ratio of MSE advection to

moisture advection instead of DSE advection. Therefore, their NGMS plot is a mirror image of our NGMS plot with respect to the x-axis [see Fig. 13 in Masunaga and L'Ecuyer (2014)]. Second, they computed the total NGMS including the background state instead of the anomalous NGMS which we computed. Thus the center of the elliptic shape is shifted to the right and downward. The composite methodology is also different from our study. Nevertheless, their study has drawn a similar conclusion about the NGMS variability to ours. That is, the first/second baroclinic modes explain the larger (along the major axis)/smaller (along the minor axis) variability of the elliptic trajectory.

2.5.2 How to compute NGMS

The values of estimated NGMS depend on the method of the computation. In section 2.4, we showed the NGMS as a time-dependent variable. But in some recent NGMS studies, NGMS is computed based on a scatter plot of MSE advection as a function of DSE advection (e.g., Raymond and Fuchs, 2009). In such a case, time-dependent fluctuations are not taken into account.

If we estimate the NGMS following that method, then the values of the NGMS, the horizontal and vertical components correspond to the slopes of the major axes of the elliptic trajectories in Fig. 2.5. The values of those slopes ($\bar{\Gamma}$, $\bar{\Gamma}_H$, and $\bar{\Gamma}_V$) are summarized in Table 2.1. As discussed above, $\bar{\Gamma}_H$ varies significantly among the time scales. Consequently, $\bar{\Gamma}$ which is the combination of $\bar{\Gamma}_H$ and $\bar{\Gamma}_V$ also varies among the different time scales. Although smaller than the variations of $\bar{\Gamma}$ and $\bar{\Gamma}_H$, there are variations of $\bar{\Gamma}_V$ among the time scales, too. These might be due to

Table 2.1: Values of $\bar{\Gamma}$, $\bar{\Gamma}_H$, and $\bar{\Gamma}_V$ on each time scale

	∼2 day scale	∼5 day scale	∼10 day scale	MJO scale
$\overline{\Gamma}$	0.26	0.25	0.20	0.33
$\overline{\Gamma}_H$	0.08	−0.02	−0.10	0.10
$\overline{\Gamma}_V$	0.18	0.25	0.29	0.20

the variations of the shapes of Ω_1 among the different time scales, which could be caused by errors due to the small number of the independent samples.

2.5.3 Tilt in other work

Mapes et al. (2006, hereafter M06) proposed the "Stretched Building Block" hypothesis that ”individual cloud systems in different phases of a large-scale wave have different durations of shallow convective, deep convective, and stratiform anvil stages in their life cycles.” This hypothesis was proposed to explain the apparent multi-scale similarities of the vertical structures between the mesoscale convective systems, convectively coupled equatorial waves, and the MJO. The systematic steepening of the leading edge slopes in the omega profiles shown in Fig. 2.3 suggest that omega may not have as much multi-scale similarity as M06 suggested, especially on the MJO time scale.

The wind divergence field on the MJO time scale in our result (Fig. 2.3h) resembles that in M06 (the second panel of Fig. 8 therein), both of which contain a small amount of tilt. However, that tilt is, as shown in section 2.3.2, too small to claim the multi-scale similarity of the omega profiles, especially on the MJO time scale.

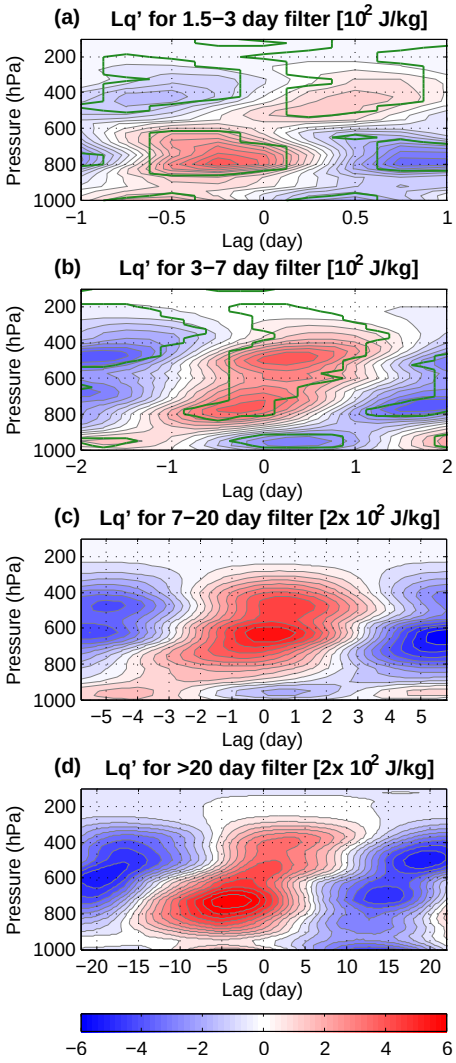

Figure 2.7: As in Fig. 2.3, but for anomalous mixing ratio. The contour intervals are 0.6*10^2 J/kg for (a) ∼2 day, (b) ∼ 5 day scales, and 1.2*10^2 J/kg for (c) ∼10 day and (d) the MJO scales.

In contrast, a significant multi-scale similarity is observed in the water vapor mixing ratio field. Figure 2.7 shows the time-height structures of the mixing ratio on the different time scales and there is significant tilt on all time scales, unlike

in vertical motion. Our figure is consistent with Fig. 7 in M06, which is given as evidence for the vertical tilt in clouds on longer time scales. Hence, we conclude that tilt in the moisture field is more robust than that in the omega field on the MJO time scale.

Previous work is also suggestive of more tilt in diabatic heating than we are finding, during the TOGA COARE MJO. Especially, our results can be compared with Fig. 9 in Lin et al. (2004, hereafter L04) and Fig. 12 in Kiladis et al. (2005, hereafter K05), in which the TOGA COARE data set was analyzed in a similar lag-regression method to ours. These studies examined diabatic heating (or Q1), which has a very similar structure to omega (not shown). The major difference in results between these studies and ours is found in the tailing edges of the event, where the L04 and K05 figures have more tilt. In Figs. 2.3 and 2.4, we show our lag-regressed plot resembles the raw structure of the MJO with a simple time filter. We believe that the relevant difference in methodology between their work and ours is that both of the other studies used spatial filters in addition to time filters to obtain their index time-series. Personal communication with Kiladis and Haertel confirmed that spatial filtering was used in their analysis and that the difference of time versus time-space filters makes non-negligible differences in the diabatic heating structures.

2.5.4 Sensitivity of choice of filter

Finally we will briefly discuss sensitivity of the choice of filters. Figure 2.8 illustrates the response functions of the >1.5 day low-pass Lanczos filter and daily running

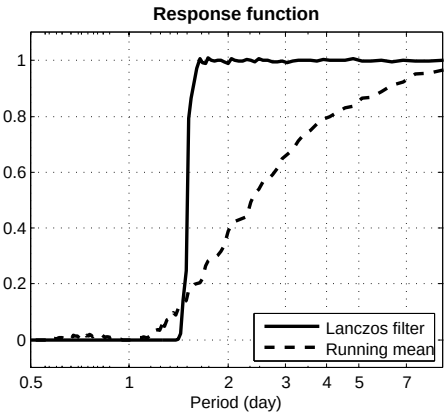

Figure 2.8: Response functions of >1.5 day low-pass Lanczos filter (with 151 points of weightings) and daily running mean filter.

mean filter. This figure shows that by using the running mean filter, about 60% of the signals on 2 day scale are lost due to the shallow slope of the response function. Even at 4 day period which corresponds to the time scale of some of the Kelvin waves, about 20% of the signals are lost. This indicates that for examining high frequency variability such as inertia gravity waves or Kelvin waves, the Lanczos filter with a steeper slope of the response function is more appropriate than the running mean filter.

2.6 Conclusions

We have examined the column-integrated moist static energy (MSE) budget during the TOGA COARE field campaign, using sounding data, and filtering the data into various frequencies of variability with $\sim$2 day, $\sim$5 day, $\sim$10 day, and >20 day periodicity. In the deep tropics, fluctuations of the column MSE are primarily

due to variations of column-integrated water vapor which are tightly connected with precipitation anomalies. Therefore, investigating the mechanisms of recharge and discharge of the column MSE leads us to a better understanding regarding the convective amplification and decay. Our analysis highlights the importance of the investigation of the column MSE on different time scales. We found that each budget term of the column MSE behaves in significantly different ways on the different time scales. As a result, dominant processes in the MSE recharge and discharge differ among the time scales. Some notable results are summarized as follows:

1. On all the time scales except for the MJO time scale, the vertical MSE advection, $-\langle\omega\partial h/\partial p\rangle$, is the most dominant process with the greatest magnitude of variations in the MSE recharge-discharge mechanism.

2. On the shorter time scales ($\sim$2 day and $\sim$5 day scales), the vertical MSE advection accounts for most of the MSE recharge and discharge, and the other terms cancel out each other so that the tendency of the column MSE $\langle\partial h/\partial t\rangle$ is primarily explained by the vertical MSE advection.

3. As the time scale gets longer, the relative importance of the other terms than the vertical advection becomes greater. Especially on the MJO time scale, all the budget terms (horizontal advection, $-\langle\mathbf{v}\cdot\nabla h\rangle$, vertical advection, $-\langle\omega\partial h/\partial p\rangle$, radiative heating $\langle Q_R\rangle$, and surface fluxes S) have nearly the same magnitude of variations.

4. The horizontal advection behaves in significantly different ways among the different time scales.

5. The amplitude of the horizontal advection becomes greater as the time scale get longer, indicating that the horizontal advection plays a more important roll in the MSE recharge-discharge mechanism on longer time scales than shorter time scales.

6. The radiative heating is approximately in phase with the precipitation (or the precipitation leads slightly) while the surface fluxes lag the precipitation except for $\sim$10 day scale on which both the radiative heating and surface fluxes are approximately in phase with the precipitation.

7. On the shorter time scales, the MSE export via vertical advection (i.e., positive $\langle \omega \partial h/\partial p \rangle$) lags the precipitation peak. As the time scale gets longer, however, the MSE export becomes more in phase with the precipitation.

The last bullet of the summary above, more in-phase MSE export via vertical advection, is primarily explained by variations in the omega profile. The tilt of the omega profile at the leading edge of the convection gets steeper as the time scale gets longer. This implies that the second baroclinic structure of the omega profile becomes less robust in the early stage of the convection. On the MJO time scale, the leading edge tilt becomes very steep, and the overall omega structure becomes closer to the first baroclinic mode. Consequently, the vertical component of the normalized gross moist stability (NGMS) becomes more a constant quantity which is nearly independent of the convective life-cycle. In contrast, on the shorter

time scales where a second baroclinic mode is prominent, the vertical NGMS has large time-dependency, thus the values of the vertical NGMS vary significantly along the convective life-cycle. The horizontal component of the NGMS doesn't have a consistent pattern among the different time scales since the horizontal MSE advection behaves in significantly different ways on the different time scales.

Furthermore, our results shown in Fig. 2.2d, the MSE budgets in the MJO event, reinforce the view of the MJO dynamics which has been emerging from recent MJO studies (e.g., Kim et al., 2014; Sobel et al., 2014) in the following ways: 1) The radiative heating and surface fluxes destabilize the MJO disturbance by amplifying and maintaining MSE anomalies. 2) The vertical advection stabilizes the disturbance by exporting the MSE and canceling the effects of the radiative heating and surface fluxes. 3) The horizontal advection plays a significant role in the eastward propagation by providing moistening ahead (in the negative lags, or to the east of), drying behind (in the positive lags, or to the west of) the active phase. Although there are differences between the different MJO events, our results in general show significant commonalities with those view points.

Finally, we should acknowledge again that we are uncertain about whether or not the results shown for the longer time scale variability ($\sim$10 day and the MJO time scales) represent statistically significant patterns because of the lack of the degrees of freedom. Our results for the MJO timescale are broadly consistent with published work on MSE budgets observed during the DYNAMO field campaign by Sobel et al. (2014), though we find the vertical NGMS less variable over an MJO life-cycle, possibly due to our use of the Lanczos filter rather than a running mean.

For more accurate and solid conclusions, we need to investigate more data sets such as ERA-Interim and TRMM which contain much longer time-series than the TOGA COARE data. We would also like to repeat our analysis using DYNAMO data in future work.

Chapter 3

Gross Moist Stability Assessment during TOGA COARE: Various Interpretations of Gross Moist Stability

3.1 Introduction

Despite decades of advancement of conceptual theories and computational ability, it has been still challenging to correctly simulate tropical convective disturbances such as convectively coupled equatorial waves (CCEWs) and the Madden-Julian oscillation (MJO) with realistic intensity and phase speed (e.g., Lin et al., 2006; Kim et al., 2009; Straub et al., 2010; Benedict et al., 2013). Current general circulation models used for climate predictions also fail to accurately simulate the position and strength of the Inter-tropical Convergence Zone, or ITCZ (e.g., Lin, 2007). We know that one of the reasons for the difficulties is our lack of fundamental understanding of the interactions between deep convection and large-scale circulations

[1]Material in this chapter is a slightly edited version of: Inoue, K., and L. E. Back, 2015: Gross Moist Stability Assessment during TOGA COARE: Various Interpretations of Gross Moist Stability. *J. Atmos. Sci.*, **72**, 4148–4166.

in the tropics. However, answering the question, "how, then, can we obtain better understanding of those interactions?", is a formidable task because the problems to solve are generally too intricate to separate different causal contributions. To simplify the complex details in convective interactions, a conceptual quantity called the gross moist stability (GMS) has been investigated, and has been proven to be useful in previous work. In this work, we utilize the GMS to look at mechanisms for convective amplification and decay in the Tropical Ocean and Global Atmosphere Coupled Ocean-Atmosphere Response Experiment (TOGA COARE) data.

The GMS, which represents efficiency of moist static energy export by large-scale circulations associated with moist convection, was originated by Neelin and Held (1987) with a simple two-layer atmospheric model. They described it as "a convenient way of summarizing our ignorance of the details of the convective and large scale transients." Raymond et al. (2007) furthered this idea by defining the relevant quantity called the normalized gross moist stability (NGMS). Although different authors have used slightly different definitions of the NGMS [see a review paper by Raymond et al. (2009)], all the NGMS represents efficiency of export of some intensive quantity conserved in moist adiabatic processes per unit intensity of the convection. In this study (or chapter), we utilize one version of the NGMS defined as

$$\Gamma \equiv \frac{\nabla \cdot \langle h\mathbf{v} \rangle}{\nabla \cdot \langle s\mathbf{v} \rangle}, \tag{3.1}$$

where s is dry static energy (DSE), h is moist static energy (MSE), $\mathbf{v}$ is horizontal wind, the del-operator represents the isobaric gradient, and the angle brackets represent a mass-weighted vertical integral from the tropopause to the surface. In

this chapter, we simply call Γ the GMS instead of the NGMS like in chapter 2. We will show that this quantity and relevant ideas can be used to diagnose mechanisms for convective amplification and decay.

Previous GMS studies can be broadly categorized into two approaches: theoretical and diagnostic approaches. Although these two approaches are looking at the same quantity, namely the GMS, it is usually difficult to compare results from those to seek agreement between them. One of the difficulties arises from the simplification of vertical structures in the theoretical GMS studies.

Most of the theoretical GMS studies are inevitably dependent on an assumption of simple vertical structures. Historically, the GMS has been proven to be a powerful tool in the version of the quasi-equilibrium framework where temperature stratification is assumed to be close to a moist adiabat (e.g. Emanuel et al., 1994; Neelin and Zeng, 2000). The perturbation vertical velocity then takes a first baroclinic mode structure and the GMS is quasi-time-independent (or nearly constant). In this framework, the values of the GMS set the phase speed of features that have commonalities with CCEWs (e.g., Emanuel et al., 1994; Neelin and Yu, 1994; Tian and Ramanathan, 2003; Raymond et al., 2009).

Recent observational studies, however, show that the vertical structures of the CCEWs are not explained only by the first baroclinic mode, but require the second baroclinic mode (e.g., Kiladis et al., 2009, and the references therein). Some theoretical studies have attempted to include the second baroclinic mode, and succeeded in producing realistic structures of the CCEWs (e.g., Mapes, 2000; Khouider and Majda, 2006; Kuang, 2008a,b). In such frameworks, however, the GMS is not attractive

as a quantity which controls phase speed and linear instability of CCEWs because the second baroclinic mode inevitably causes singularities of the GMS, making it blow up to infinity at some points (e.g., Inoue and Back, 2015a). Raymond and Fuchs (2007) and Fuchs et al. (2012) found in their simple models, which can also produce variable vertical structures, that the dependency of the phase speed of equatorial gravity waves on the GMS is subtle.

The GMS also plays an important role in theoretical MJO studies. Recently, the idea emerged that the MJO is a moisture mode (Fuchs and Raymond, 2007)[2], and some simple linear model studies demonstrated that the moisture mode becomes unstable when the GMS or "effective" GMS, including radiative or surface flux feedbacks, is negative (Fuchs and Raymond, 2007; Raymond and Fuchs, 2007; Raymond et al., 2009; Fuchs et al., 2012, and others.)

The recent diagnostic GMS studies have focused more on the highly time-dependent property of the GMS (e.g., Hannah and Maloney, 2011; Benedict et al., 2014; Hannah and Maloney, 2014; Masunaga and L'Ecuyer, 2014; Sobel et al., 2014; Inoue and Back, 2015a). Specifically, those studies have focused on the aspect of the GMS as a quantity which describes the destabilization/stabilization mechanisms of the local convective disturbances. Episodes of organized convective disturbances generally begin with a bottom-heavy vertical velocity profile which progressively evolves into a top-heavy profile as the convection develops. As in Fig. 3.1, a bottom-heavy profile with MSE-rich-lower-tropospheric convergence and

[2]Other studies (Yu and Neelin, 1994, and many others) also suggested modes which correspond to the "moisture mode" with different names. For a concise summary about the terminology, refer to the introduction in Sugiyama (2009a)

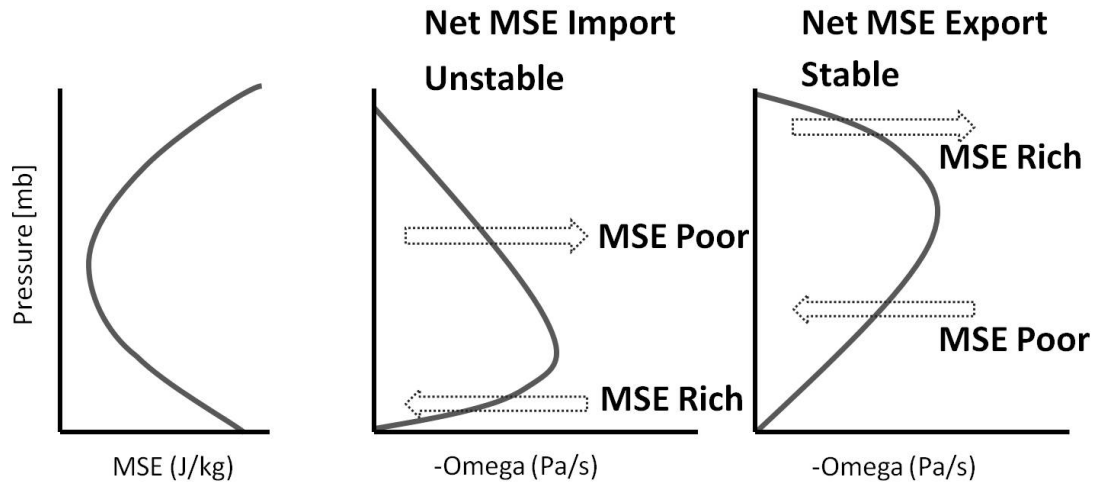

Figure 3.1: Schematic figures of a typical MSE profile and vertical velocity (omega) profiles in a bottom-heavy and a top-heavy shape. The leftward (rightward) arrows correspond to convergence (divergence).

MSE-poor-mid-tropospheric divergence leads to net import of MSE by the vertical circulation, and thus destabilizes the local convective system via column moistening; this condition is associated with negative GMS. Conversely, a top-heavy profile with MSE-poor-mid-tropospheric convergence and MSE-rich-upper-tropospheric divergence is associated with net export of MSE and positive GMS, which causes the local convection to decay. These destabilization/stabilization mechanisms play crucial roles in the dynamics of the CCEWs in cloud resolving model simulations (e.g., Peters and Bretherton, 2006; Kuang, 2008a).

In this study, we focus our attention on the diagnostic aspect of the GMS. We propose useful applications of the GMS to diagnoses of tropical convective disturbances. First, by utilizing the time-dependency of the GMS, we claim that the destabilization/stabilization mechanisms discussed above play crucial roles in

short time-scale tropical disturbances, and that those mechanisms can be extracted by investigating the GMS in observational data. Second, we propose some methods to calculate a meaningful value of the quasi-time-independent GMS whose computations and interpretations are relatively easy.

The rest of this chapter is structured as follows. Section 3.2 describes the data set we used (the TOGA COARE data set). Section 3.3 sets forth the theoretical framework of the relationship between the time-dependent GMS and amplification/decay of convection. In this section, we introduce new quantities called the critical GMS (a ratio of diabatic source to the convective intensity) and drying efficiency (a version of the effective GMS; GMS minus critical GMS). By investigating those quantities in the TOGA COARE data, we demonstrate the amplification/decay mechanisms of the convection in section 3.4. In section 3.5, we extend our arguments toward the time-independent aspect of the GMS. In this section, we suggest some methods to calculate the quasi-time-independent GMS and clarify the interpretations of that. In section 3.6, we summarize our arguments.

3.2 Data description

We investigate the field campaign data from the Tropical Ocean Global Atmosphere Coupled Ocean-Atmosphere Response Experiment (TOGA COARE; Webster and Lukas, 1992) to clarify the relationship between the GMS, vertical atmospheric structures (especially vertical velocity profiles), and convective amplification/decay. The TOGA COARE observational network was located in the western Pacific warm

pool region. In this study, we analyze the data averaged over the spatial domain called the Intensive Flux Array (IFA), which is centered at 2° S, 156° E, bounded by the polygon defined by the meteorological stations at Kapingamarangi and Kavieng and ships located near 2° S, 158° E and 4° S, 155° E. The sounding data was collected during the 4-month Intensive Observing Period (IOP; 1 November 1992 to 28 February 1993) with 6 hourly time resolution. All variables are filtered with a 24-hour running mean for a reason explained in the next section.

The data set utilized was constructed by Minghua Zhang, who analyzed the sounding data by using an objective scheme called constrained variational analysis (Zhang and Lin, 1997). In that scheme, the state variables of the atmosphere are adjusted by the smallest possible amount to conserve column-integrated mass, moisture, static energy, and momentum. See Zhang and Lin (1997) for more detailed information about the scheme.

3.3 Theoretical framework

Following Yanai et al. (1973), we start with the vertically integrated energy and moisture equations:

$$\frac{\partial\langle s\rangle}{\partial t} + \langle \mathbf{v}\cdot\nabla s\rangle + \langle \omega\frac{\partial s}{\partial p}\rangle = \langle Q_R\rangle + LP + H, \tag{3.2}$$

$$\frac{\partial\langle Lq\rangle}{\partial t} + \langle \mathbf{v}\cdot\nabla Lq\rangle + \langle \omega\frac{\partial Lq}{\partial p}\rangle = LE - LP, \tag{3.3}$$

where $s \equiv c_p T + gz$ is dry static energy (DSE); $c_p T$ is enthalpy; gz is geopotential; Q_R is radiative heating rate; L is the latent heat of vaporization, P is precipitation rate; H is surface sensible heat flux; q is mixing ratio, E is surface evaporation; the angle brackets represent mass-weighted column-integration from 1000 hPa to 100 hPa; and the other terms have conventional meteorological meanings. Each quantity is averaged over the IFA. As in Raymond et al. (2009), assuming ω vanishes at the surface and tropopause pressures, utilizing the continuity equation, and taking integration by parts yields

$$\frac{\partial \langle s \rangle}{\partial t} + \nabla \cdot \langle s\mathbf{v} \rangle = \langle Q_R \rangle + LP + H, \tag{3.4}$$

$$\frac{\partial \langle Lq \rangle}{\partial t} + \nabla \cdot \langle Lq\mathbf{v} \rangle = LE - LP. \tag{3.5}$$

In the deep tropics, temperature anomalies are small due to weak rotational constraints (Charney, 1963, 1969; Bretherton and Smolarkiewicz, 1989), and thus the DSE tendency and horizontal DSE advective terms in Eqs. 3.2 and 3.4 are often assumed to be negligible, which is called the weak temperature gradient approximation (WTG; Sobel and Bretherton, 2000; Sobel et al., 2001). When applying the WTG to observational data, however, we need to remove diurnal cycles of the temperature field, which is the primary exception to the WTG. Figures 3.2a and 3.2b illustrate the power spectra of the column DSE and column moisture tendencies. These figures show that most variance of the column DSE tendency is explained by the diurnal cycle while the diurnal cycle of the column moisture tendency is much smaller. Therefore, taking a daily running mean filter makes the column DSE

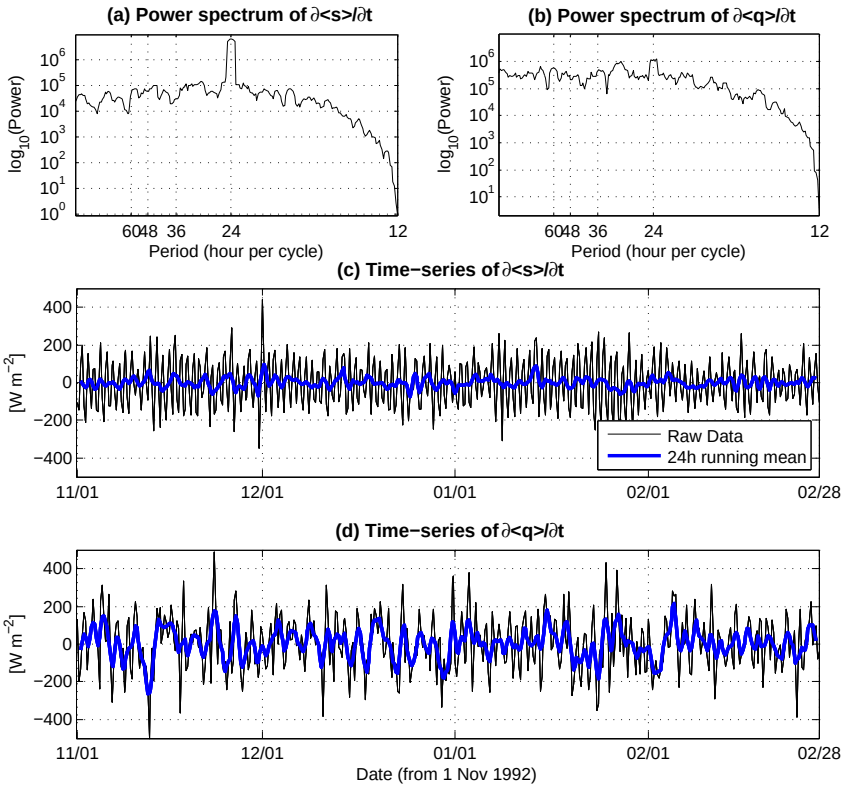

Figure 3.2: (a): Power spectrum of $\partial\langle s\rangle/\partial t$. (b): Power spectrum of $\partial\langle q\rangle/\partial t$. (c): Time-series of raw (black), and daily running averaged $\partial\langle s\rangle/\partial t$ (blue) during TOGA COARE. (d): As in (c), but for $\partial\langle q\rangle/\partial t$. The mixing ratio q is scaled by the latent heat of evaporation into the energy unit.

tendency much less significant than the column moisture tendency as illustrated in Figs. 3.2c and 3.2d, allowing us to neglect it. Neglecting the column DSE tendency and adding Eqs. 3.4 and 3.5 yield

$$\frac{\partial\langle Lq\rangle}{\partial t} \simeq -\nabla\cdot\langle h\mathbf{v}\rangle + \langle Q_R\rangle + S, \tag{3.6}$$

where $h \equiv s + Lq$ is moist static energy (MSE) and $S \equiv LE + H$ is surface fluxes.

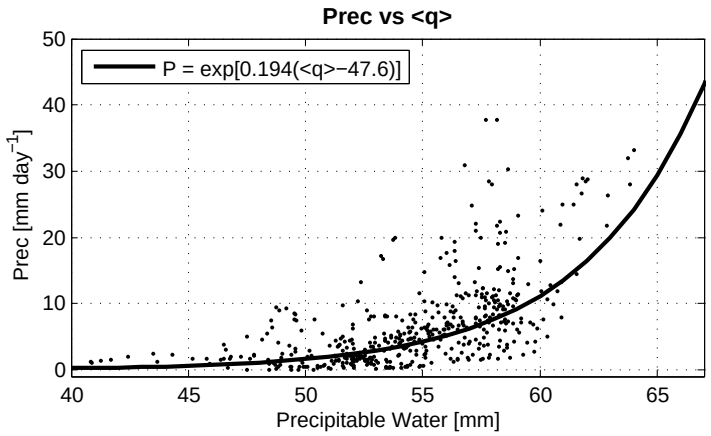

Figure 3.3: Precipitation as a function of precipitable water $\langle q \rangle$. The black line was computed by a nonlinear least squares fitting.

Generally H is negligible over the tropical ocean.

We now utilize a relationship between precipitation and column-integrated water vapor $\langle q \rangle$ (aka precipitable water or water vapor path), which was shown by Bretherton et al. (2004). They showed the relation in the form of

$$P = \exp[a(\langle q \rangle - b)], \tag{3.7}$$

where a and b are some constants calculated by nonlinear least squares fitting. Figure 3.3 illustrates the relationship between the precipitation and precipitable water during TOGA COARE. The patterns statistically agree with the proposed exponential relationship. This exponential relationship is, however, not so crucial for this study. The ideas described below are valid as long as the precipitation has positive correlation with the precipitable water, which can be observed in the figure.

Equation 3.7 can be replaced by a linearized form

$$P = \frac{\langle q \rangle}{\tau_c}, \tag{3.8}$$

where τ_c is a convective adjustment time scale as in the Betts-Miller parameterization (Betts, 1986; Betts and Miller, 1986), and the same conclusions can be drawn. Taking the natural logarithm of Eq. 3.7, and plugging it into Eq. 3.6 yields

$$\frac{L}{a}\frac{\partial \ln P}{\partial t} \simeq -\nabla \cdot \langle h\mathbf{v} \rangle + D, \tag{3.9}$$

where $D \equiv \langle Q_R \rangle + S$ is a diabatic source term.

Equation 3.9 indicates two convective phases:

$$\nabla \cdot \langle h\mathbf{v} \rangle - D < 0, \tag{3.10}$$

$$\nabla \cdot \langle h\mathbf{v} \rangle - D > 0. \tag{3.11}$$

According to Eq. 3.9, precipitation increases over time if a system is in the phase of Eq. 3.10 while it decreases in the phase of Eq. 3.11. Since the value of $\nabla \cdot \langle h\mathbf{v} \rangle - D$ is dependent on the intensity of the convection, it is advantageous to normalize it by the intensity of the convection so that we can take composites of all the convective events with different intensities in the TOGA COARE data; and from that context, the concept of the gross moist stability (GMS) appears. A similar normalization technique has been utilized by Hannah and Maloney (2011).

In this study, we define a case with positive $\nabla \cdot \langle s\mathbf{v} \rangle$ to be convectively active,

and a case with negative $\nabla \cdot \langle s\mathbf{v} \rangle$ to be convectively inactive. Since we are interested in events when convection is happening, most of the analyses given below are conducted only for convectively active times. When convection is active, dividing Eqs. 3.10 and 3.11 by $\nabla \cdot \langle s\mathbf{v} \rangle$ yields

$$\Gamma - \Gamma_C < 0, \tag{3.12}$$

$$\Gamma - \Gamma_C > 0, \tag{3.13}$$

where

$$\Gamma_C = \frac{\langle Q_R \rangle + S}{\nabla \cdot \langle s\mathbf{v} \rangle}, \tag{3.14}$$

which we name the critical GMS. Γ is the gross moist stability (GMS) defined in Eq. 3.1, and we call the quantity $\Gamma - \Gamma_C$ the drying efficiency. This drying efficiency looks similar to a quantity called the effective GMS (e.g., Su and Neelin, 2002; Bretherton and Sobel, 2002; Peters and Bretherton, 2005; Sobel and Maloney, 2012), and is close to the effective GMS used in Hannah and Maloney (2014). However, we chose not to refer to it as the effective GMS; the reason for this choice is given in chapter 4, and is not discussed in this chapter.

When $\Gamma - \Gamma_C$ is negative/positive, the system is in the amplifying/decaying phase in which convection intensifies/decays. (When convection is inactive with negative $\nabla \cdot \langle s\mathbf{v} \rangle$, those phases are reversed.) These hypotheses are not surprising because $\Gamma - \Gamma_C$ is equivalent to

$$-\frac{1}{\nabla \cdot \langle s\mathbf{v} \rangle} \frac{\partial \langle Lq \rangle}{\partial t} \sim -\frac{1}{P} \frac{\partial \langle q \rangle}{\partial t}, \tag{3.15}$$

which represents efficiency of moisture discharge/recharge per unit intensity of convection, and the GMS and the critical GMS respectively represent contributions of MSE advection ($-\nabla \cdot \langle h\mathbf{v} \rangle$) and diabatic source ($D \equiv \langle Q_R \rangle + S$) terms to that efficiency. Therefore, the phases of Eqs. 3.12 and 3.13 simply state that a moistened/dried system leads to amplification/dissipation of the convection. Despite the simplicity, this concept is useful from both diagnostic and theoretical perspectives.

We take composites of convective structures onto values of the drying efficiency. This composite method functions well because the drying efficiency is independent of the convective intensity (therefore is only a function of the convective structures), and is a good index of the local convective stability[3]. Hence by using the drying efficiency composite method, we can illustrate the connection between convective structures and the stability of moist convection.

3.4 Results and discussion

3.4.1 Drying efficiency and convective amplification/decay

First, we need to verify the hypotheses of the amplifying and decaying phases, Eqs. 3.12 and 3.13, for convectively active times during TOGA COARE. When computing Γ and Γ_C, as suggested by Raymond et al. (2009), the time filter was applied to the numerator and denominator before taking the ratio between them.

[3]In this study, we use the word "stability" to refer to the drying efficiency, and not to conventional thermodynamic stability such as convective available potential energy (CAPE), or stability of some linear modes.

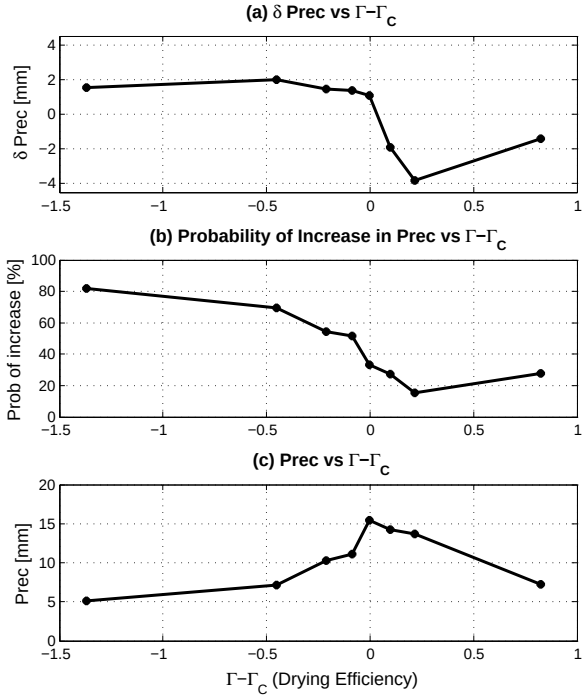

Figure 3.4: (a): Binned precipitation changes as a function of the drying efficiency $\Gamma - \Gamma_C$, averaged in 12.5-percentile bins of $\Gamma - \Gamma_C$. The precipitation changes δP were computed by center differencing. (b): Binned probabilities of increase in precipitation as a function of $\Gamma - \Gamma_C$, averaged in the same bins as (a). The values subtracted from 100 % represent probabilities of decrease in precipitation. (c): Binned precipitation as a function of $\Gamma - \Gamma_C$, computed in the same way as above.

All data points with $\nabla \cdot \langle s\mathbf{v} \rangle$ less than 10 Wm^{-2} were removed to exclude convectively inactive times and to avoid division by zero. Furthermore, since we apply a binning average method to $\Gamma - \Gamma_C$, we excluded 2.5% outliers from the left and right tails of the PDF of $\Gamma - \Gamma_C$ before taking composites in order to avoid biases due to very large and small values.

Figure 3.4a shows precipitation changes as a function of the drying efficiency $\Gamma - \Gamma_C$. The precipitation changes were calculated by center differencing, and those

were averaged in 12.5-percentile bins with respect to $\Gamma - \Gamma_C$. In the amplifying phase (i.e., negative $\Gamma - \Gamma_C$), the precipitation changes are positive, indicating the convection is enhanced; in the decaying phase (i.e., positive $\Gamma - \Gamma_C$), in contrast, the convection is attenuated. Figure 3.4b illustrates the probabilities of increase in precipitation as a function of the binned $\Gamma - \Gamma_C$. These probabilities were computed as a ratio of the number of the data points with positive precipitation changes to the total number of the data points within each 12.5-percentile bin of $\Gamma - \Gamma_C$. When $\Gamma - \Gamma_C$ is negative and large (-1.4 to -0.4) the probability of precipitation increase is greater than $\sim 70\%$ whereas when $\Gamma - \Gamma_C$ is positive and large (0.2 to 0.8) the precipitation decreases at $\sim 80\%$. As $\Gamma - \Gamma_C$ increases from -0.4 to 0.2, the probability of precipitation increase rapidly drops. Both Figs. 3.4a and 3.4b are consistent with the hypotheses of the amplification/decaying phases.

Figure 3.4c shows the precipitation as a function of the binned $\Gamma - \Gamma_C$. In the amplifying phase, the precipitation increases as $\Gamma - \Gamma_C$ becomes less negative, and reaches the maximum when $\Gamma - \Gamma_C$ is zero, or Γ is equal to Γ_C; in the decaying phase, the precipitation decreases with increase in $\Gamma - \Gamma_C$. This figure, together with Figs. 3.4a and 3.4b, indicates that values of the drying efficiency are statistically linked to convective development and dissipation; that is, convection generally begins with high efficiency of moistening (negative and large $\Gamma - \Gamma_C$), the efficiency of moistening gradually decreases (i.e., $\Gamma - \Gamma_C$ becomes less negative) as the convection develops, and eventually starts to discharge moisture (positive $\Gamma - \Gamma_C$) leading to dissipation of the convection.

When interpreting Fig. 3.4 and the other drying efficiency figures given below,

one caution is required; that is, those figures don't include any information about time. They were plotted in order of stability from the most unstable to the most stable, and not ordered in time, and so the length of the x-axis does not represent the actual duration of the corresponding structures. Nevertheless, because every phenomenon statistically evolves from unstable to stable conditions, those figures represent a statistical convective life-cycle; the convection generally evolves from negative and large $\Gamma - \Gamma_C$ to positive and large $\Gamma - \Gamma_C$.

3.4.2 Variability of drying efficiency

In the last subsection, we verified that when the drying efficiency $\Gamma - \Gamma_C$ is negative/-positive, convection is enhanced/attenuated, respectively. Now let us investigate which processes cause variability of the drying efficiency, making the convection amplify or dissipate. In other words, we examine how moist convection evolves from unstable (negative $\Gamma - \Gamma_C$) into stable (positive $\Gamma - \Gamma_C$) conditions.

Variability of $\Gamma - \Gamma_C$ is separated into contributions of the GMS (or advective terms) and of the critical GMS (or diabatic source terms). Furthermore, GMS can be divided into horizontal and vertical components as

$$\Gamma = \Gamma_H + \Gamma_V, \tag{3.16}$$

where

$$\Gamma_H = \frac{\langle \mathbf{v} \cdot \nabla h \rangle}{\nabla \cdot \langle s\mathbf{v} \rangle},$$

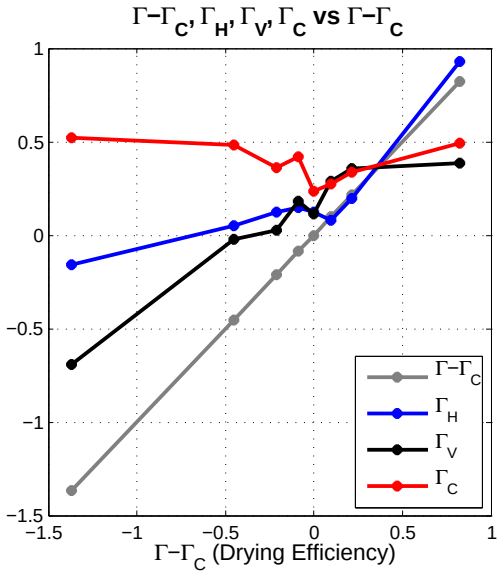

Figure 3.5: Variability of each component, horizontal GMS Γ_H (blue), vertical GMS Γ_V (black), and critical GMS Γ_C (red), decomposed from drying efficiency $\Gamma - \Gamma_C$ (gray), and averaged in the same bins as ones in Fig. 3.4.

$$\Gamma_V = \frac{\langle \omega \frac{\partial h}{\partial p} \rangle}{\nabla \cdot \langle s\mathbf{v} \rangle}.$$

Therefore, variability of the drying efficiency can be explained by three components, changes in the horizontal GMS Γ_H, the vertical GMS Γ_V, and the critical GMS Γ_C. Figure 3.5 shows those three components as a function of the binned $\Gamma - \Gamma_C$. By comparing the amount of the slope of each component with the slope of $\Gamma - \Gamma_C$, we can determine which processes explain the variability of the drying efficiency when it evolves from negative to positive values.

In this figure, Γ_C is broadly constant and maintains positive values around $0.25 \sim 0.5$ along all the values of $\Gamma - \Gamma_C$. (Although it varies some, the variations are less significant compared to the other two components.) This indicates that

Γ_C always decreases the value of $\Gamma - \Gamma_C$ toward negative values, and thus forces the convective system toward the amplifying phase. The combination of radiative heating and surface fluxes, therefore, constantly creates a tendency toward destabilization as a moisture (or MSE) source, increasing efficiency of moistening (or decreasing the drying efficiency) during both the amplifying and decaying phases, and doesn't contribute to the variability of $\Gamma - \Gamma_C$. Therefore, given a constant value of Γ_C, convection intensifies/decays when the GMS is less/greater than that critical constant. More detailed discussions about Γ_C are provided in section 3.4.4 and section 3.5.

In the amplifying phase (i.e., $\Gamma - \Gamma_C < 0$), most of the slope of $\Gamma - \Gamma_C$ is explained by Γ_V. This indicates that vertical MSE advection mainly explains the convective evolution from the amplifying into the decaying phases. In this phase, Γ_H is broadly constant and nearly zero, implying the horizontal MSE (or moisture) advection doesn't contribute to amplification of the convection. When $\Gamma - \Gamma_C$ is ~ -1.4, the values of Γ_H, Γ_V, and Γ_C are ~ -0.2, ~ -0.7, and ~ 0.5, respectively. Hence the system is primarily moistened by the vertical MSE advection, the radiative heating, and the surface fluxes. As the convection evolves towards the decaying phase, Γ_V becomes less negative, which indicates moistening via vertical advection becomes less efficient. At $\Gamma - \Gamma_C \simeq -0.5$, Γ_H and Γ_V are nearly zero while Γ_C is ~ 0.5. In this stage, only the radiative heating and the surface fluxes moisten the convective system. As the convection develops further to greater $\Gamma - \Gamma_C$, the vertical advection starts to discharge moisture (i.e., positive Γ_V), leading to dissipation of the convection. Therefore, what drives the convection from the amplifying into the

decaying phase is the vertical MSE advection (associated with Γ_V), which at the beginning moistens the system, followed by discharge of moisture. During that evolution, Γ_C constantly tends to moisten the system, resisting the drying by the vertical advection.

In the decaying phase (i.e., $\Gamma - \Gamma_C > 0$), in contrast, the slope of Γ_H nicely matches the slope of $\Gamma - \Gamma_C$. Therefore, the drying efficiency in the fastest dissipation stage is mainly explained by the horizontal MSE advection. Γ_V also keeps positive values in this phase, indicating the vertical advection also exports MSE and dries the system. But the horizontal advection dries the system more efficiently (i.e., $\Gamma_H > \Gamma_V$). Γ_C is relatively constant with positive values, making $\Gamma - \Gamma_C$ smaller. Therefore, in the decaying phase, both horizontal and vertical advection tend to dry the system while the radiative heating and surface fluxes tend to supply MSE anomalies into the convective system.

3.4.3 Variability of vertical GMS

We have shown that in the amplifying phase, most of the variability of the drying efficiency is explained by the vertical GMS Γ_V. Now we investigate how Γ_V varies. During TOGA COARE, 94% of the total variance of $\langle \omega \partial h / \partial p \rangle$ is explained by the variance of ω. Thus, the variability of Γ_V is mainly due to the fluctuations of ω profiles. The relationship between Γ_V and ω has been pointed out by previous studies (e.g., Back and Bretherton, 2006; Peters and Bretherton, 2006; Sobel and Neelin, 2006; Sobel, 2007; Raymond et al., 2009; Masunaga and L'Ecuyer, 2014; Inoue and Back, 2015a). Those studies have demonstrated that bottom-heavy ω profiles

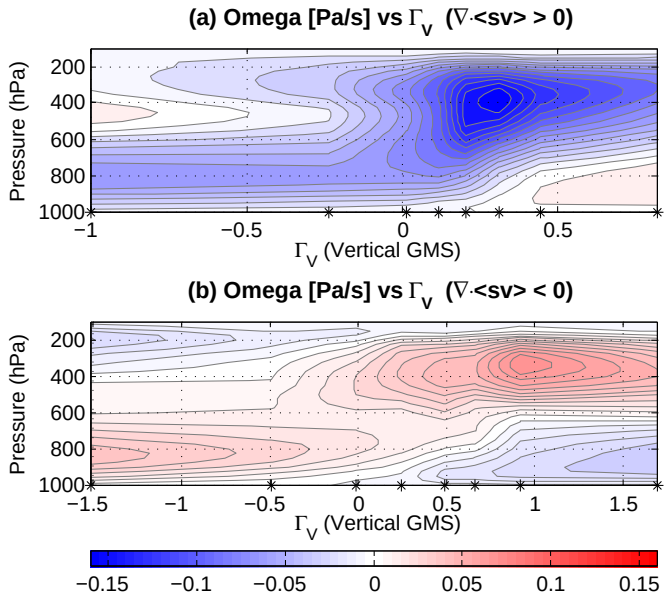

Figure 3.6: (a): Vertical ω structures with respect to the values of vertical GMS Γ_V for convectively active times ($\nabla \cdot \langle s\mathbf{v} \rangle > 0$), averaged in 12.5-percentile bins of Γ_V. The star-marks on the x-axis denote the centers of the bins. (b): As in (a), but for convectively inactive times ($\nabla \cdot \langle s\mathbf{v} \rangle < 0$). The contour interval of (a) and (b) is 2*10^{-2} Pa/s. All points with $|\nabla \cdot \langle s\mathbf{v} \rangle|$ less than 10 Wm^{-2} were removed for avoiding division by zero.

which import MSE via lower level convergence and middle level divergence are associated with negative (or close to negative) values of Γ_V while top-heavy profiles with middle level convergence and upper level divergence export MSE from the atmospheric column, causing positive and large Γ_V.

Figure 3.6a illustrates the relationship between Γ_V and ω profiles for convectively active times in the TOGA COARE data. The blue/red shaded contours represent ascending/descending motions. As described above, negative and large Γ_V is associated with bottom-heavy ω shapes, and as Γ_V increases ω becomes more top-

heavy. When the convection is inactive (i.e., $\nabla \cdot \langle s\mathbf{v} \rangle$ is negative; in Fig. 3.6b), the relation is reversed; that is, negative and large Γ_V corresponds to top-heavy ω with lower tropospheric descending motion while positive and large Γ_V is associated with bottom-heavy profiles with upper tropospheric descending motion.

Figure 3.6b, together with Fig. 3.6a, completes a life-cycle of the convection. The convection is initialized with small and positive Γ_V during negative $\nabla \cdot \langle s\mathbf{v} \rangle$ (in Fig. 3.6b), and Γ_V increases as the convection develops. After passing the singularity of Γ_V (or zero $\nabla \cdot \langle s\mathbf{v} \rangle$), it becomes a negative and large value that corresponds to bottom-heavy motion (in Fig. 3.6a), which gradually deepens with increase in Γ_V and reaches the other singularity. Again, the sign of Γ_V flips, and it becomes negative and large when the convection is in a stratiform shape (in Fig. 3.6b), and as the stratiform convection is dissipated the value of Γ_V becomes less negative, completing the life-cycle. Since our main interest in this study is convective amplification/decay mechanisms instead of initialization/termination processes, we concentrate on analyses of the data points with positive $\nabla \cdot \langle s\mathbf{v} \rangle$.

Interestingly, the anomalous temperature field is coherent with the ω profiles. Figure 3.7 shows anomalous temperature profiles with respect to the binned Γ_V, which is compared with Fig. 3.6a. When Γ_V is negative with bottom-heavy ω profiles, an anomalously warm layer can be observed around 600 hPa. The height of this stable layer matches the upper limit of the bottom-heavy ω. This temperature structure is commonly observed in CCEWs (e.g., Straub and Kiladis, 2003; Kiladis et al., 2009; Frierson et al., 2011). We speculate those temperature anomalies work like a lid which prevents the bottom-heavy ω profiles from becoming top-heavy,

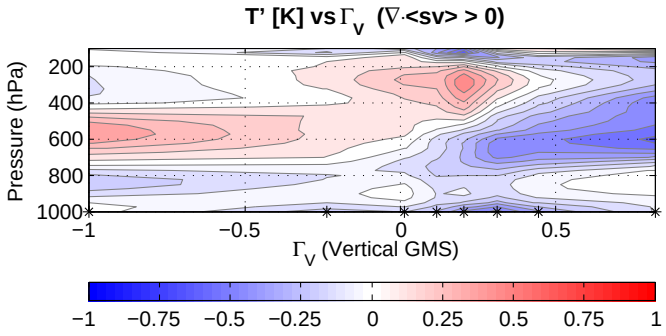

Figure 3.7: As in Fig. 3.6a, but for temperature anomalies. The contour interval is 0.125 K.

maintains the negativity of Γ_V, and destabilizes the convective system by enhancing the efficiency of moistening. This type of interaction between temperature anomalies and convection appears to be in favor of the "activation control" hypothesis of large-scale disturbances proposed by Mapes (1997).

Previous TOGA COARE studies (e.g., Johnson et al., 1996, 1999) have posited that that stable layer is associated with melting processes of cloud droplets around $0°$C, though it is not clear why that would occur preferentially during the growth phase of convection. An important role of that layer in convective dynamics has been pointed out by, for instance, Kikuchi and Takayabu (2004), who claimed that moistening below the $0°$C level may be an influential factor for development of the convection. However, cloud micro-physics may not be the only mechanism for the temperature anomalies. Raymond et al. (2014) claimed that those temperature anomalies are a balanced thermal response to the existence of mesoscale vorticity anomalies in the tropical atmosphere. This hypothesis has been verified in the case

of tropical cyclogenesis and in easterly waves (e.g., Cho and Jenkins, 1987; Jenkins and Cho, 1991).

3.4.4 Critical GMS and feedback constants

Now that we have shown the critical GMS Γ_C stays relatively constant in both the amplifying and decaying phases (in Fig. 3.5), let us investigate it in more detail. In theoretical GMS studies where a vertical structure is assumed to be a single mode, the GMS is quasi-time-independent. That is equivalent to saying that the MSE advection can be linearly parameterized with the intensity of the convection. However, Inoue and Back (2015a) demonstrated that the time-independent GMS is not an accurate approximation especially on a couple day time-scales. In this subsection, we will show that linear approximation of the diabatic source terms is, instead, more consistent with the observational data during TOGA COARE than that of the advective terms (compare Figs. 3.8c and 3.8f, which are scatter plots of D and $\nabla \cdot \langle h\mathbf{v} \rangle$ as a function of $\nabla \cdot \langle s\mathbf{v} \rangle$). This linear approximation of D provides us with a new interpretation of the quasi-time-independent GMS, which will be discussed more in section 3.5.

Generally, column radiative heating $\langle Q_R \rangle$ can be expressed as

$$\langle Q_R \rangle = r_R L P + Q_0, \tag{3.17}$$

where r_R is a cloud-radiative feedback constant and Q_0 is the clear-sky column radiative heating (e.g., Su and Neelin, 2002; Bretherton and Sobel, 2002; Peters and

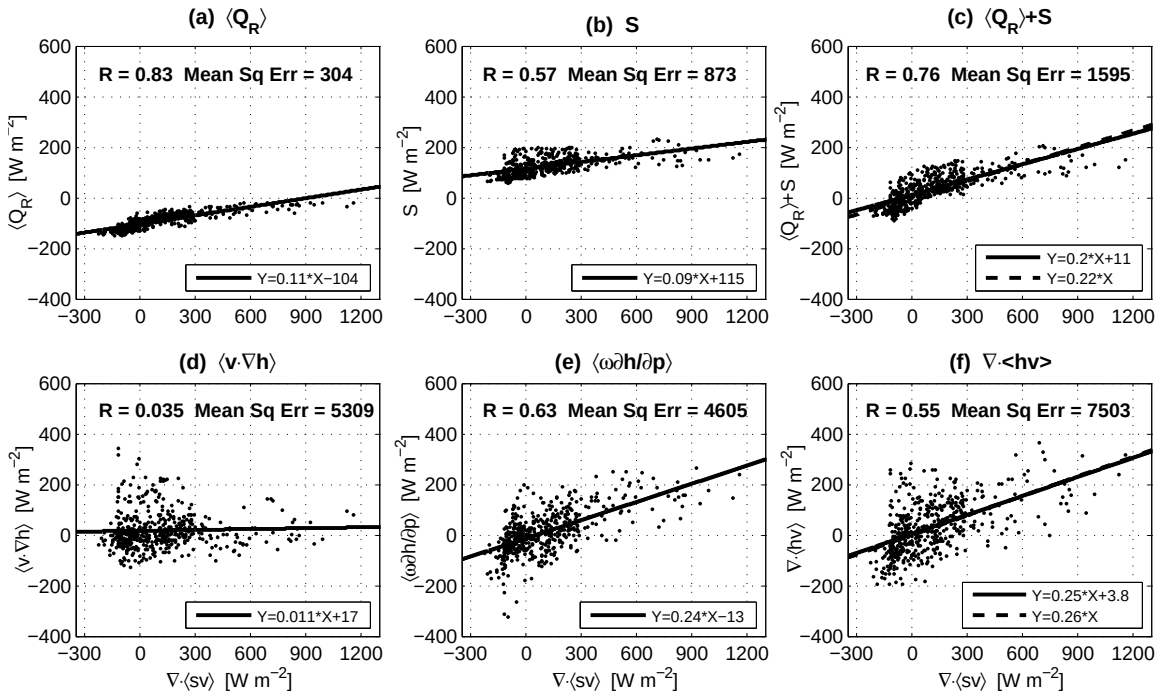

Figure 3.8: (a): Scatter plot of column radiative heating $\langle Q_R \rangle$ as a function of vertically integrated total DSE export ($+\nabla \cdot \langle s\mathbf{v} \rangle$) for all data points including convectively inactive times. The solid line was computed by a least squares fitting. The values in the upper left corner represent correlation coefficient (R) and mean square error (Mean Sq Err) from the linear fit. (b)—(f): As in (a), but respectively for surface fluxes S, diabatic source $\langle Q_R \rangle + S$, vertically integrated horizontal MSE export ($+\langle \mathbf{v} \cdot \nabla h \rangle$), vertically integrated vertical MSE export ($+\langle \omega \partial h / \partial p \rangle$), and the total MSE export ($+\nabla \cdot \langle h\mathbf{v} \rangle$). The dashed lines in (c) and (f) were computed by a regression through the origin.

Bretherton, 2005; Sobel, 2007). The DSE budget equation (Eq. 3.4) with the WTG is

$$\nabla \cdot \langle s\mathbf{v} \rangle \simeq \langle Q_R \rangle + LP. \tag{3.18}$$

Here we neglect the surface sensible heat flux. By rearranging Eq. 3.18 and plugging

it into Eq. 3.17, we obtain

$$\langle Q_R \rangle = \gamma_R \nabla \cdot \langle s\mathbf{v} \rangle + \beta_R, \tag{3.19}$$

where

$$\gamma_R \equiv \frac{r_R}{1 + r_R} \tag{3.20}$$

and

$$\beta_R \equiv \frac{Q_0}{1 + r_R}. \tag{3.21}$$

Figure 3.8a illustrates a scatter plot of $\langle Q_R \rangle$ versus $\nabla \cdot \langle s\mathbf{v} \rangle$ with the least squares fitting. $\langle Q_R \rangle$ which has a high correlation with $\nabla \cdot \langle s\mathbf{v} \rangle$ (0.83) is well represented by the linear equation (Eq. 3.19).

Similarly, applying a positive correlation between surface fluxes and precipitation (e.g., Raymond et al., 2003; Back and Bretherton, 2005; Araligidad and Maloney, 2008; Dellaripa and Maloney, 2015), we obtain

$$S = r_S LP + S_0, \tag{3.22}$$

where r_S represents an evaporation-moisture convergence feedback (e.g., Zebiak, 1986; Back and Bretherton, 2005), and S_0 is the surface fluxes at zero precipitation. In a similar way to Eq. 3.19, utilizing the DSE budget equation with the WTG, Eq. 3.22 can be rearranged into

$$S = \gamma_S \nabla \cdot \langle s\mathbf{v} \rangle + \beta_S, \tag{3.23}$$

where

$$\gamma_S \equiv \frac{r_S}{1 + r_R} \tag{3.24}$$

and

$$\beta_S \equiv \frac{S_0 + r_R S_0 - r_S Q_0}{1 + r_R}. \tag{3.25}$$

Figure 3.8b is a scatter plot of S versus $\nabla \cdot \langle s\mathbf{v} \rangle$ with the least squares fit. The linear fit seems adequate enough to express the overall pattern of S. As pointed out by previous studies, there is a positive correlation (0.57) between S and intensity of the convection ($\nabla \cdot \langle s\mathbf{v} \rangle$ in this study). However, this positive correlation is not the only reason for the validity of the linear approximation of S because the correlation between $\nabla \cdot \langle h\mathbf{v} \rangle$ and $\nabla \cdot \langle s\mathbf{v} \rangle$ is also high (0.55) and is comparable to that of S. (The correlation of $\langle \omega \partial h / \partial p \rangle$ is even higher (0.63).) For the linear approximation of S to be more accurate than that of $\nabla \cdot \langle h\mathbf{v} \rangle$, besides the positive correlation, small variance of S compared to the other MSE budget terms (especially $\nabla \cdot \langle h\mathbf{v} \rangle$) is required. That can be seen in the values of the mean square errors of the linear fits given in Fig. 3.8. The mean square error for S is about an order smaller than that for $\nabla \cdot \langle h\mathbf{v} \rangle$, indicating that the linear fit of S is better than that of $\nabla \cdot \langle h\mathbf{v} \rangle$. This smaller mean square error is simply due to the smaller variance of S than that of $\nabla \cdot \langle h\mathbf{v} \rangle$.

Hence, for Eq. 3.23 to be more valid than assuming a constant GMS, two conditions have to be satisfied: 1) S is positively correlated with $\nabla \cdot \langle s\mathbf{v} \rangle$, and 2) variance of S is much smaller than that of $\nabla \cdot \langle h\mathbf{v} \rangle$. The second condition is violated in longer time-scales such as the MJO scale, in which variance of S is comparable to the other

MSE budget terms (e.g., Maloney, 2009; Benedict et al., 2014; Inoue and Back, 2015a). Furthermore, Dellaripa and Maloney (2015) found that the relationship between S and convective intensity (or γ_S in Eq. 3.23) significantly varies along a life-cycle of the MJO. It must be noted, therefore, that although the same methodology we used in this work (or drying efficiency composite) is applicable to MJO events to look for moistening/drying mechanisms, the potential conclusions for the MJO are likely to be different from the conclusions in this study. For instance, we can make a similar figure to Fig. 3.5 for the MJO. In that figure, however, Γ_C is most likely not nearly constant due to the significant variation of γ_S in Eq. 3.23 along a MJO life-cycle. We more thoroughly discuss time-scale dependency and what time-scales we're seeing the behavior of in this study in section 3.4.7.

Since both $\langle Q_R \rangle$ and S are well represented by the least squares fittings, it is the case for D, the combination of $\langle Q_R \rangle$ and S. Adding Eqs. 3.19 and 3.23 yields

$$D \equiv \langle Q_R \rangle + S = \gamma \nabla \cdot \langle s\mathbf{v} \rangle + \beta, \tag{3.26}$$

where

$$\gamma \equiv \gamma_R + \gamma_S = \frac{r_R + r_S}{1 + r_R} \tag{3.27}$$

and

$$\beta \equiv \beta_R + \beta_S = \frac{Q_0 + S_0 + r_R S_0 - r_S Q_0}{1 + r_R}, \tag{3.28}$$

which is shown in Fig. 3.8c with a high correlation coefficient (0.76).

Interestingly, Eq. 3.26 can be simplified further because, in the TOGA COARE data, the intercept of the $\langle Q_R \rangle$ fitting (β_R; in Fig. 3.8a) cancels out the intercept of

the S fitting (β_S; in Fig. 3.8b), causing the intercept of the D fitting (β; in Fig. 3.8c) to be negligible. Hence, Eq. 3.26 becomes

$$D \simeq \gamma \nabla \cdot \langle s\mathbf{v} \rangle. \tag{3.29}$$

Therefore, the critical GMS is

$$\Gamma_C \equiv \frac{D}{\nabla \cdot \langle s\mathbf{v} \rangle} \simeq \gamma. \tag{3.30}$$

The good linear fit of D indicates the constancy of Γ_C in Fig. 3.5 in the TOGA COARE data set. (Of course, this linear approximation is not perfect, and thus Γ_C slightly varies in Fig. 3.5.) The amplifying and decaying phases, Eqs. 3.12 and 3.13, can be written as

$$\Gamma - \gamma < 0, \tag{3.31}$$

$$\Gamma - \gamma > 0. \tag{3.32}$$

These equations suggest that a convective system intensifies (decays) if the GMS is less (greater) than the feedback constant γ. Thus, how much convection can grow is tightly related to the feedback constant γ.

We do not yet understand why the intercept is close to zero. It would be interesting to examine whether this disappearance of the intercept β is just a coincidence or is due to some physical constraints. Although we are not sure if this is the case in general, we could, at least, use the simple linearization (Eq. 3.29) in a simple model framework, which gives ideas discussed in section 3.5.

When dealing with anomalous MSE budgets instead of the total budgets, the argument becomes much simpler because we don't have to worry about the intercept β. We can take anomalies of the MSE budgets to obtain the similar relations to Eqs. 3.31 and 3.32 as follows:

$$\Gamma' - \gamma < 0, \tag{3.33}$$

$$\Gamma' - \gamma > 0, \tag{3.34}$$

where

$$\Gamma' \equiv \frac{\nabla \cdot \langle h\mathbf{v} \rangle'}{\nabla \cdot \langle s\mathbf{v} \rangle'} \tag{3.35}$$

is anomalous GMS. [Interpretations of the anomalous GMS are discussed in Inoue and Back (2015a).] Equations 3.33 and 3.34 respectively correspond to the amplifying and decaying phases, and precipitation reaches the maximum when

$$\Gamma'|_{P_{max}} = \gamma. \tag{3.36}$$

In spite of the simplicity of the anomalous form, we include the mean state in our argument below in order to obtain further interesting ideas discussed in section 3.5.

Before going to the next subsection, it should be acknowledged that the arguments given above are just statistical ones, and not based on physical reasoning. In other words, we haven't discussed a-priori reasons why, for instance, S has a positive linear relationship with the convective intensity. It might be due to downdraft-enhanced gustiness (Redelsperger et al., 2000) or a convergence feedback where enhanced surface fluxes lead to enhanced precipitation; but examining

these a-priori reasons is beyond the scope of this study and more thorough studies about those are required for more general conclusions.

3.4.5 Drying efficiency and convective structures

We have thus far shown the following:

- Bottom-heaviness of ω associated with negative vertical GMS Γ_V is responsible for most of the moisture (or MSE) import in the amplifying phase.
- That bottom-heaviness might be related to middle tropospheric temperature anomalies.
- In the amplifying phase, horizontal GMS Γ_H is close to zero, indicating a small contribution of the horizontal advection to the moistening.
- Critical GMS Γ_C is broadly constant due to the linearity of $\langle Q_R \rangle$ and S and due to the cancellation of the intercept β.
- In the decaying phase, both vertical and horizontal advection export column moisture (i.e., $\Gamma_H, \Gamma_V > 0$), but the horizontal advection exports more efficiently (i.e., $\Gamma_H > \Gamma_V$).

Those points are summarized in Figs. 3.9 and 3.10, which illustrate vertical structures of ω, temperature anomalies, vertical and horizontal MSE advection as a function of the binned $\Gamma - \Gamma_C$.

When $\Gamma - \Gamma_C$ is negative, ω is in a bottom-heavy shape (Fig. 3.9a) which imports MSE from the lower troposphere (Fig. 3.10a), whereas the horizontal advection

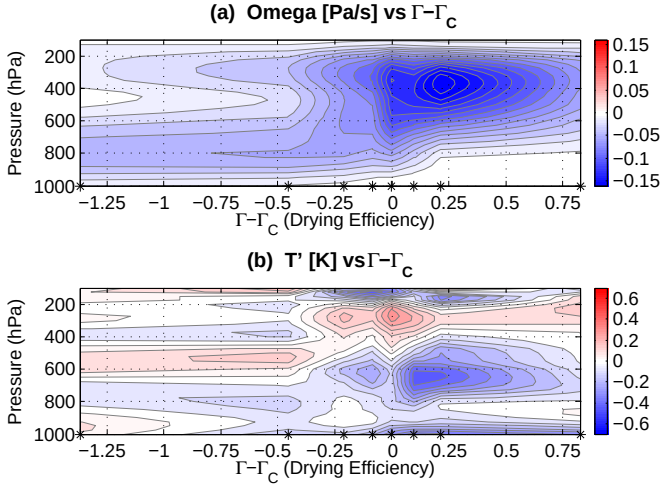

Figure 3.9: (a): Binned vertical ω structures with respect to the drying efficiency $\Gamma - \Gamma_C$ for convectively active times ($\nabla \cdot \langle s\mathbf{v} \rangle > 0$), averaged in the same bins as in Figs. 3.4 and 3.5. The star-marks on the x-axis denote the bin-centers. The contour interval is 2*10 $^{-2}$ Pa/s. (b): As in (a), but for temperature anomalies. The contour interval is 0.1 K.

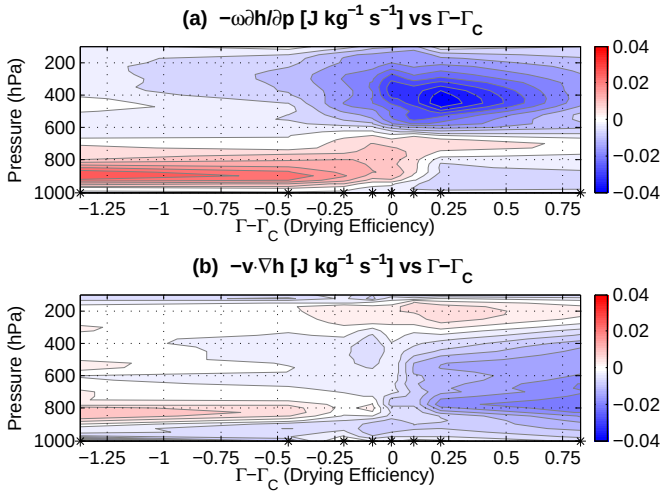

Figure 3.10: (a) and (b): As in Fig. 3.9, but for vertical and horizontal MSE advection, respectively. The contour interval is 5*10^{-3} J/kg/s.

plays only a little role in the moistening processes in this phase (Fig. 3.10b). The bottom-heaviness of ω might be related to the anomalously warm layer at about 600 hPa, observed in Fig. 3.9b. Since Γ_C is broadly constant, it doesn't change the vertical structures, but it contributes to the shift of the x-axis compared to Fig. 3.6a. For instance, in Fig. 3.6a, ω starts to become top-heavy at $\Gamma_V \simeq -0.25$, whereas in Fig. 3.9a it does at $\Gamma - \Gamma_C \simeq -0.45$. The difference between those values is due to Γ_C, which is roughly constant.

When $\Gamma - \Gamma_C$ is positive, ω with a top-heavy shape (Fig. 3.9a) exports MSE from the upper-troposphere (Fig. 3.10a). Besides that, horizontal advection also exports MSE from the lower-to-middle troposphere as depicted in Fig. 3.10b. This behavior of the horizontal advection is not surprising. Generally, at the very end of the dissipative stage of convection, the atmospheric column is anomalously moist compared to the surrounding environment. Therefore, horizontal winds in any direction lead to drying of the atmospheric column, causing positive Γ_H as shown in Fig. 3.10b.

The mechanisms described above imply that tropical convection is a self regulating system. Variability of the drying efficiency is predominantly regulated by the shape of vertical velocity profiles (in the amplifying phase) and by the atmospheric column moisture (in the decaying phase), both of which are parts of the convective system. Moreover, timing of a transition from the amplifying into the decaying phase is associated with the feedback constants between the radiation, the evaporation, and the convection. A convective episode which starts with shallow convection spontaneously enhances the convection itself via bottom-heavy ω. Deep-

ened convection, in turn, starts to dry out the system via top-heavy ω, dissipating the convection. In the decaying phase, horizontal winds also dry the system by carrying dry air from the surrounding environment into the convective system or carrying moist air from the system to the environment. Therefore, we might be able to refer to the amplifying/decaying phases as "self-amplifying/self-decaying" phases.

3.4.6 Vertical structures and resulting convective intensity

Now we investigate a qualitative relationship between vertical structures and resulting convective intensity. Utilizing the MSE budget equation (Eq. 3.6) and the linearized precipitation equation (Eq. 3.8), we obtain

$$\tau_c \frac{\partial LP}{\partial t} = -\nabla \cdot \langle h\mathbf{v} \rangle + D. \tag{3.37}$$

Dividing both sides by $\nabla \cdot \langle s\mathbf{v} \rangle$ and applying Eqs. 3.17 and 3.18 yield

$$\frac{\partial \ln(LP + \beta_R)}{\partial t} = -\frac{r_R + 1}{\tau_c}(\Gamma - \Gamma_C), \tag{3.38}$$

where r_R and β_R are the constants defined in Eq. 3.19. We neglect the sensible heat flux. This equation is only applicable to the data points with positive $\nabla \cdot \langle s\mathbf{v} \rangle$. We solve this equation for P, and obtain

$$LP = (LP_0 + \beta_R) \exp\left\{\frac{r_R + 1}{\tau_c}\Lambda\right\} - \beta_R, \tag{3.39}$$

where

$$\Lambda \equiv -\int_{t_0}^{t} (\Gamma - \Gamma_C)\, \mathrm{d}t$$

and P_0, t_0 are some reference precipitation and time. This equation demonstrates that the rate of precipitation increase is determined by Λ, a time-integration of the efficiency of moistening (negative drying efficiency). There are three ways to increase Λ: 1) decrease Γ via bottom-heavy ω, 2) increase Γ_C via enhanced feedbacks between the convection, the radiation, and the evaporation (according to Eqs. 3.27 and 3.30), and 3) increase the duration in which $\Gamma - \Gamma_C$ is negative. Therefore, those indicate that, bottom-heavy ω, strong radiative-cloud and evaporation-convergence feedbacks, long duration of shallower vertical motion profiles, can all intensify the resulting precipitation maximum. In Figs. 3.7 and 3.9b, we observed the temperature anomalies in the middle troposphere that might keep the bottom-heaviness of ω. Hence, it would be interesting to test whether there is a positive correlation between the intensity of the temperature anomalies and the intensity of the resulting convection.

3.4.7 Time-scale dependence

When examining MSE budgets in tropical variability, it is always necessary to clarify which time-scale is the target because MSE budgets behave in significantly different ways among different time-scales (e.g., Inoue and Back, 2015a). In this study, we have taken composites with respect to the values of $\Gamma - \Gamma_C$, which is, according to Eq. 3.15, equivalent to negative column water vapor tendency per unit intensity of the convection. Therefore, it is the most natural to think that our analyses herein

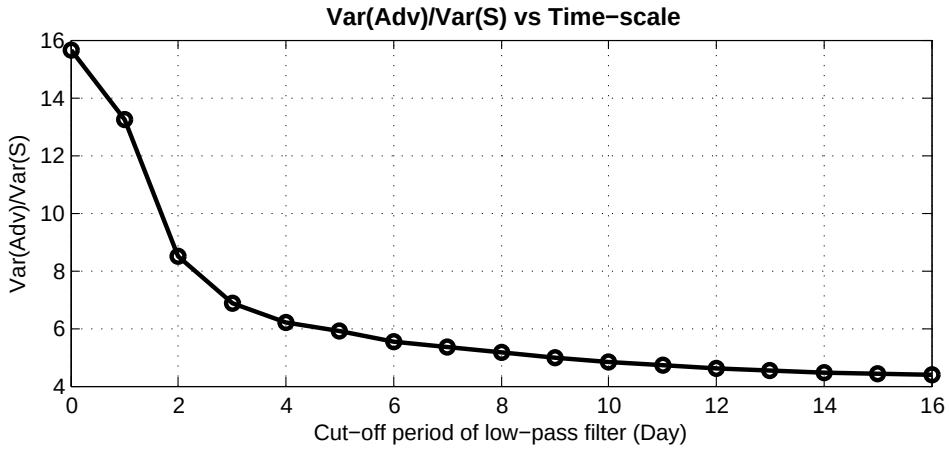

Figure 3.11: Ratio of the variance of $\nabla \cdot \langle h\mathbf{v} \rangle$ to the variance of S on different time-scales. The x-axis represents cut-off period of low-pass Lanczos filter with 151 weights, and the y-axis represents the ratio of var($\nabla \cdot \langle h\mathbf{v} \rangle$) to var($S$).

represent the convective structures with the highest frequency in the data set. We have removed the diurnal cycle, thus the highest-frequency variability in the TOGA COARE data is disturbance with $\sim$2 day periodicity [see Fig. 1 in Inoue and Back (2015a)]. We examined the structures of the high-frequency disturbances using the same data (not shown), and found significant resemblances with the structures shown in Figs. 3.6, 3.7, 3.9, and 3.10.

By using a low-pass (or band-pass) filter, we could apply this method to lower-frequency variability such as Kelvin waves and the MJO. In section 3.4.4, however, we showed that the linear approximation of S requires small variance of S compared with $\nabla \cdot \langle h\mathbf{v} \rangle$, and that condition is violated as the time-scale gets longer. Figure 3.11 illustrates the ratio of the variance of $\nabla \cdot \langle h\mathbf{v} \rangle$ to the variance of S as a function of cut-off period of the Lanczos low-pass filter with 151 weights. This figure shows the

same information as the ratio of power spectra between them. As the cut-off period increases, the periodicity of the time-series becomes longer. This figure shows that as the periodicity becomes longer, the variance of $\nabla \cdot \langle h\mathbf{v} \rangle$, which dominates S on short time-scales, becomes more comparable to the variance of S. It indicates that the linear approximation of S becomes less accurate on longer time-scales, thus we cannot assume the constancy of the critical GMS Γ_C any more.

We have discussed the convective amplification/decay mechanisms in such a way that because Γ_C is nearly constant, variability of Γ is the most important. But this may not be the case for longer time-scale disturbances such as the MJO. Therefore, although a similar methodology is applicable to the MJO, the potential conclusions may be different from that in this study. It would be interesting to perform a similar analysis to that here for longer time-scales of variability.

3.5 More discussion: characteristic GMS

As described above, the gross moist stability Γ is a highly time-dependent quantity which significantly varies from negative to positive along the convective life-cycle. Recent diagnostic studies have focused more on the time-dependent aspect of Γ (e.g., Hannah and Maloney, 2011; Benedict et al., 2014; Hannah and Maloney, 2014; Masunaga and L'Ecuyer, 2014; Sobel et al., 2014; Inoue and Back, 2015a); on the other hand, quasi-time-independent GMS has been popularly utilized in theoretical studies (e.g., Neelin and Held, 1987; Emanuel et al., 1994; Neelin and Yu, 1994; Tian and Ramanathan, 2003; Fuchs and Raymond, 2007; Raymond et al., 2009; Sugiyama,

2009a; Sobel and Maloney, 2012). Then, some natural questions will come up; that is, "How can we calculate a meaningful value of the quasi-time-independent GMS in observational data, how can we interpret it, and how can we relate it with the highly time-dependent GMS?" Fortunately, all the analyses shown so far in this paper have already provided the answers for those questions. We will clarify those answers through a couple steps.

First, we need to clarify how to calculate a single meaningful value of the quasi-time-independent GMS. There have been a couple different ways proposed in the past literature from different contexts. We now show that all of them are almost equivalent in the TOGA COARE data set. Those different definitions are listed as follows:

1. GMS defined at the maximum anomalous precipitation (e.g., Sobel and Bretherton, 2003), or

$$\Gamma'_{max} \equiv \Gamma'|_{P_{max}}; \tag{3.40}$$

2. GMS computed from a scatter plot of anomalous $\nabla \cdot \langle h\mathbf{v} \rangle$ versus $\nabla \cdot \langle s\mathbf{v} \rangle$ (e.g., Table 1 in Inoue and Back, 2015a), or

$$\tilde{\Gamma}' \equiv \frac{\overline{\nabla \cdot \langle h\mathbf{v} \rangle' * \nabla \cdot \langle s\mathbf{v} \rangle'}}{\overline{\nabla \cdot \langle s\mathbf{v} \rangle'^2}}; \tag{3.41}$$

3. GMS computed from a scatter plot of non-anomalous $\nabla \cdot \langle h\mathbf{v} \rangle$ versus $\nabla \cdot \langle s\mathbf{v} \rangle$

(e.g., Fig. 9 in Raymond and Fuchs, 2009), or

$$\tilde{\Gamma} \equiv \frac{\overline{\nabla \cdot \langle h\mathbf{v} \rangle * \nabla \cdot \langle s\mathbf{v} \rangle}}{\overline{\nabla \cdot \langle s\mathbf{v} \rangle^2}}; \tag{3.42}$$

4. climatological GMS (e.g., Eq. 7 in Kuang, 2010), or

$$\overline{\Gamma} \equiv \frac{\overline{\nabla \cdot \langle h\mathbf{v} \rangle}}{\overline{\nabla \cdot \langle s\mathbf{v} \rangle}}; \tag{3.43}$$

The bar represents time average, and the prime is perturbation from the time mean. There are a few more different methods to estimate quasi-time-independent GMS (e.g., Yu et al., 1998; Chou et al., 2013), but all of them can be qualitatively categorized in one of the above lists. We include the horizontal advection in the definitions above although it is generally not included.

From Eq. 3.36, Γ'_{max} is equal to γ, which represents a combination of the radiative-convective and the evaporation-convergence feedback constants according to Eq. 3.27. Now γ can be statistically calculated by a least squares method as

$$\gamma = \frac{\overline{D' * \nabla \cdot \langle s\mathbf{v} \rangle'}}{\overline{\nabla \cdot \langle s\mathbf{v} \rangle'^2}}. \tag{3.44}$$

But from the MSE budget equation, γ is also expressed as

$$\gamma = \frac{\overline{\{\partial \langle h \rangle / \partial t + \nabla \cdot \langle h\mathbf{v} \rangle'\} * \nabla \cdot \langle s\mathbf{v} \rangle'}}{\overline{\nabla \cdot \langle s\mathbf{v} \rangle'^2}}. \tag{3.45}$$

Since $\partial \langle h \rangle / \partial t$ and $\nabla \cdot \langle s\mathbf{v} \rangle'$ (or P') are almost out of phase (e.g., Inoue and Back,

2015a), covariance between them becomes negligible if the time-series is long enough. Therefore, we obtain

$$\Gamma'_{max} = \gamma = \tilde{\Gamma}'. \tag{3.46}$$

Moreover, in the TOGA COARE data, the intercept of the least squares fit of D (β; in Fig. 3.8c) is negligible. This indicates that the least squares fit of $\nabla \cdot \langle h\mathbf{v} \rangle$ as a function of $\nabla \cdot \langle s\mathbf{v} \rangle$ also has to go through the origin as shown in Fig. 3.8f where the least squares fit is almost identical to the regression line through the origin. Therefore, we obtain

$$\tilde{\Gamma}' = \tilde{\Gamma}, \tag{3.47}$$

and this equation can be rearranged into

$$\tilde{\Gamma}' = \overline{\Gamma}. \tag{3.48}$$

Furthermore, Fig. 3.8d shows the horizontal component of $\tilde{\Gamma}'$, $\tilde{\Gamma}'_H$, is close to zero (0.011), hence

$$\tilde{\Gamma}' \simeq \tilde{\Gamma}'_V, \tag{3.49}$$

where $\tilde{\Gamma}'_V$ is the vertical component of $\tilde{\Gamma}'$.

The above arguments demonstrate that all the quasi-time-independent GMSs defined in the different ways (1–4) are equivalent, and are all equal to γ in the TOGA COARE data. We collectively call them the characteristic GMS. From the definition of γ (Eq. 3.27), it represents a combination of the radiative-convective

and the evaporation-convergence feedback constants, and moreover, it is equal to the critical GMS Γ_C from Eq. 3.30, which is the threshold between the amplifying and the decaying phases (Eqs. 3.12 and 3.13). Therefore, we can interpret all the characteristic GMSs, Γ'_{max}, $\tilde{\Gamma}'$, $\tilde{\Gamma}$, and $\overline{\Gamma}$ as follows:

First: A critical value which determines the threshold between the amplifying and the decaying phases of the convection at a given place.

Second: A value of the time-dependent GMS at the precipitation maximum.

Third: A combination of the radiative-convective and the evaporation-convergence feedback constants.

These interpretations are useful for clarifying the mechanisms for convective amplification/decay. At a given place, convection intensifies if a value of the time-dependent GMS is below the characteristic (or climatological) GMS at that place, and that sub-critical GMS is primarily due to bottom-heavy ω profiles. Eventually, the ω profile becomes a top-heavy shape, causing the GMS to be greater than the critical value, which leads to decay of the convection. This idea is demonstrated in Fig. 3.12. Here Γ_C in Fig. 3.4 is replaced with the climatological GMS $\overline{\Gamma}$. The figure shows that when $\Gamma - \overline{\Gamma}$ is negative/positive, the convection intensifies/decays as shown in Fig. 3.4. This mechanism is consistent with what Masunaga and L'Ecuyer (2014) claimed. Furthermore, the third interpretation indicates that the feedback constant γ ($\equiv \gamma_R + \gamma_S$) is equal to the climatological GMS $\overline{\Gamma}$ which is primarily determined by climatological ω profiles. That relationship implies a tight

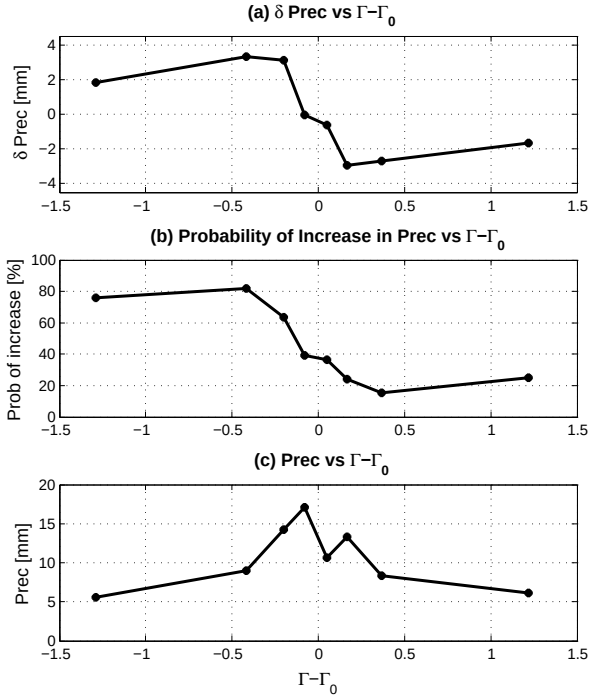

Figure 3.12: (a), (b), and (c): As in Fig. 3.4, but as a function of GMS minus climatological GMS, $\Gamma - \overline{\Gamma}$ (labelled as $\Gamma - \Gamma_0$).

connection between ω profile shapes and the linear feedback mechanisms between the radiation, the evaporation, and the convection

For facilitating conceptualization of the GMS variability, Fig. 3.12 is plotted in a different plane. In Fig. 3.13, the red/blue dots represent data points in which convection intensifies/decays, and the slope of the black solid line represents the characteristic (or critical, or climatological) GMS. This figure illustrates that when a dot is located below/above the critical line in this plane (which is equivalent to negative/positive drying efficiency), the convection intensifies/decays. Since the x-axis represents convective intensity, as convection develops, the dot moves to the right. But the GMS has to be equal to the climatological one at the convective

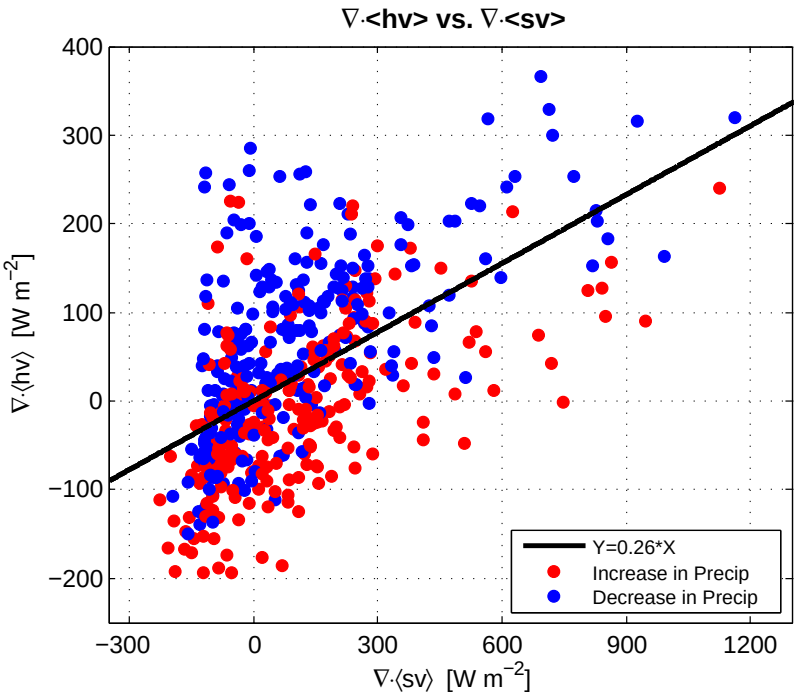

Figure 3.13: Scatter plot of $\nabla \cdot \langle h\mathbf{v} \rangle$ vs. $\nabla \cdot \langle s\mathbf{v} \rangle$ with the characteristic (or climatological) GMS line as in Fig. 3.8f. The red/blue dots represent data points when the precipitation increases/decreases.

maximum. So the dot also moves toward the characteristic GMS line. This idea is depicted in Fig. 3.14. From this figure, we can view each short time-scale convective life-cycle as a fluctuation of the rapidly varying GMS (shown in the thin light-red arrows) around the slowly varying climatological GMS line (shown as the solid blue line) in the $\nabla \cdot \langle h\mathbf{v} \rangle$–vs–$\nabla \cdot \langle s\mathbf{v} \rangle$ plane. In this study, we utilized the rapidly varying property of the GMS (shown in the thick red arrow) to extract the mechanisms for convective application/decay, ignoring the slow variation (shown in the thick blue arrows) of the climatological GMS which might be regulated by large-scale

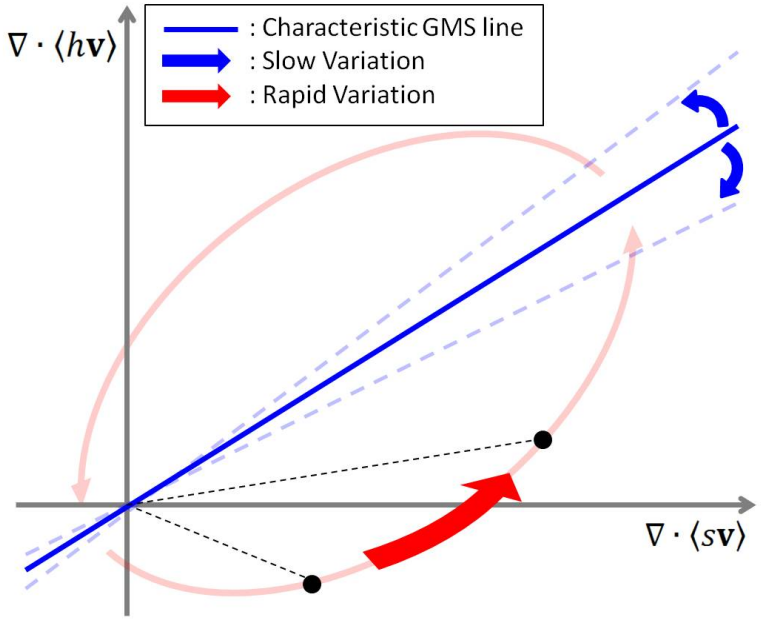

Figure 3.14: Schematic figure of a convective life-cycle (light-red arrows) in the $\nabla \cdot \langle h\mathrm{v} \rangle$–vs–$\nabla \cdot \langle s\mathrm{v} \rangle$ plane. The thick red arrow represents variation of highly time-dependent GMS; the blue thick arrows represent variation of slowly changing climatological GMS.

phenomena such as a planetary boundary layer contribution controlled by SST gradient (e.g., Sobel and Neelin, 2006; Back and Bretherton, 2009a,b).

3.6 Summary

We have investigated the convective amplification/decay mechanisms in short time-scale disturbances by examining the gross moist stability (GMS; Γ) and its relevant quantities in the TOGA COARE data set. We coined two quantities, namely the critical GMS (Γ_C) and the drying efficiency ($\Gamma - \Gamma_C$). $\Gamma - \Gamma_C$ represents negative

precipitable water tendency per unit intensity of convection. Γ and Γ_C respectively represent the contributions of the advective terms ($\nabla \cdot \langle h\mathbf{v} \rangle$) and the diabatic source terms ($D \equiv \langle Q_R \rangle + S$) to the drying efficiency.

First, we verified that the convection is amplified/attenuated via negative/positive drying efficiency; Figures 3.4a and 3.4b show that the precipitation intensifies/decays when $\Gamma - \Gamma_C$ is negative/positive. Therefore, we call the phases with negative/positive $\Gamma - \Gamma_C$ the amplifying/decaying phases. We also found that the precipitation reaches the maximum when $\Gamma - \Gamma_C$ is zero, or the GMS is equal to the critical GMS (Fig. 3.4c).

Next, we investigated which processes explain the variability of $\Gamma - \Gamma_C$. By doing so, we can clarify which processes destabilize the convection, and how the convection is forced to transition from the amplifying into the decaying phases. In the amplifying phase (i.e., $\Gamma - \Gamma_C < 0$), most of the variability of $\Gamma - \Gamma_C$ is explained by the vertical GMS Γ_V (Fig. 3.5), which indicates that the convective transition from the amplifying into the decaying phases is primarily controlled by the vertical MSE advection. Convection with a bottom-heavy ω profile efficiently imports MSE via low level convergence (negative Γ_V), which leads to further enhancement of the convection via column moistening. Positive temperature anomalies in the middle-troposphere might play a role in controlling the bottom-heaviness of ω. As the convection develops, the ω profile gradually becomes top-heavy, starting export of the column MSE from the upper troposphere (positive Γ_V), which leads to dissipation the convection, finishing the amplifying phase. During the amplifying phase, the horizontal GMS Γ_H broadly stays close to zero, indicating that the

horizontal MSE advection doesn't contribute the column moistening in this phase. In the decaying phase ($\Gamma - \Gamma_C < 0$), in contrast, the variability of $\Gamma - \Gamma_C$ is mainly explained by Γ_H. In this phase, the vertical advection also exports MSE (i.e., $\Gamma_V > 0$), but the horizontal advection exports more efficiently (i.e., $\Gamma_H > \Gamma_V$), leading to decay of the convection via column drying.

Throughout the convective life-cycle, the critical GMS Γ_C broadly stays constant with positive values (Fig. 3.5). This indicates that the column radiative heating and surface fluxes always tend to destabilize the convective system by supplying the MSE sources in a constant manner. The constancy of Γ_C is due to the linearity of the diabatic source with respect to the intensity of the convection (which is the case only in short time-scale disturbances), and also due to the disappearance of the intercept β in Eq. 3.26. Although we are not sure whether or not the negligible β is the case in general, the linear approximation of the diabatic source provides us with a simple framework in which we can interpret the GMS in novel ways.

In section 3.5, we extended our arguments toward the quasi-time-independent GMS. We demonstrated that all of the following definitions of the quasi-time-independent GMSs are equivalent in the TOGA COARE data: 1) anomalous GMS at the precipitation maximum (Γ'_{max}), 2) GMS computed from a scatter plot of anomalous $\nabla \cdot \langle h\mathbf{v} \rangle$ versus $\nabla \cdot \langle s\mathbf{v} \rangle$ ($\tilde{\Gamma}'$), 3) GMS computed from a scatter plot of non-anomalous $\nabla \cdot \langle h\mathbf{v} \rangle$ versus $\nabla \cdot \langle s\mathbf{v} \rangle$ ($\tilde{\Gamma}$), 4) climatological GMS ($\overline{\Gamma}$); all of which are collectively called the characteristic GMS. The characteristic GMS can be interpreted as follows: I) a critical value which determines the threshold between the amplifying and the decaying phases, II) a value of the GMS at the precipitation

maximum, and III) a combination of the radiative-convective and the evaporation-convergence feedback constants. These interpretations, together with Fig. 3.14, facilitate conceptualization of the GMS variability. From this figure, we can view a short time-scale convective life-cycle as a fluctuation of rapidly changing GMS around a slowly changing climatological GMS line in the $\nabla \cdot \langle h\mathbf{v} \rangle$–vs–$\nabla \cdot \langle s\mathbf{v} \rangle$ plane. In this study, we utilized the rapidly changing property of the GMS to diagnose the convective amplification/decay mechanisms.

Chapter 4

Gross Moist Stability Analysis. Part I: Assessment of Satellite-based Products in the GMS Plane

4.1 Introduction

It is well known that tropical convection and column-integrated water vapor (aka. precipitable water) are tightly related. Past work showed that there is a positive correlation between precipitable water and precipitation (e.g., Raymond, 2000; Bretherton et al., 2004; Neelin et al., 2009; Masunaga, 2012). This moisture-precipitation relationship plays a key role in an interaction between convection and associated large-scale circulations in the tropics; the ensemble of subgrid-scale convection alters large-scale circulations, and the large-scale circulations, in turn, change the local environment to be favorable or unfavorable for the convection via changing the local moisture condition. In this study, we present new diagnostic applications of a conceptual quantity called the gross moist stability (GMS) to investigate an

[1]Material in this chapter is a slightly edited version of the submitted draft: Inoue, K., and L. E. Back, 2016: Gross Moist Stability Analysis. Part I: Assessment of Satellite-based Products in the GMS Plane. *J. Atmos. Sci.*, submitted.

interaction between convection and large-scale circulations.

For investigating it, it has been proven that column-integrated moist static energy (MSE) budgets are useful. Temperature anomalies are small in the deep tropics owing to a large Rossby radius (e.g., Charney, 1963; Bretherton and Smolarkiewicz, 1989), which leads to a conceptual framework called the weak temperature gradient approximation (WTG; Sobel and Bretherton, 2000; Sobel et al., 2001). This property of the tropics indicates that analyses of column MSE budgets approximately tell us about the processes associated with the growth and decay of precipitable water. And these analyses are most likely if not always accompanied by a quantity called the GMS.

The GMS, which represents the efficiency of the advective export of MSE by large-scale circulations associated with convection, was originally coined by Neelin and Held (1987) with a simple two-layer atmospheric model. Two decades later, Fuchs and Raymond (2007) and Raymond et al. (2007) expanded this idea by defining a relevant quantity called the normalized GMS (NGMS) to include more general atmospheric structures. Since then, different authors have used slightly different definitions of the NGMS [see a review by Raymond et al. (2009)], but the philosophies behind them are the same; they all represent the amount of water vapor (or MSE or moist entropy) exported by the unit intensity of convection. In this study, the NGMS is simply called the GMS.

For the beginning of this study, let us first pose a fundamental question: "Why should we look at the GMS?" By this question, we mean, "Why do we look at the GMS rather than just the MSE budgets?" Of course, there is no unique answer for it,

but there have been "popular" answers among meteorological communities. And some confusion as to GMS studies has arisen because the popular answer has been changing over the past three decades. So let us briefly describe the history of the GMS, specifically in the context of tropical convection.

The GMS had gained attention in a framework of the version of quasi-equilibrium called the strict quasi-equilibrium (SQE) where temperature stratification is assumed to be sufficiently close to a moist adiabat, which constrains the perturbation vertical velocity profile to take a first baroclinic mode structure (Emanuel et al., 1994). In this kind of framework, the GMS is quasi-time-independent and determines the phase speed of eigen-modes that have commonalities with convectively coupled equatorial waves (CCEWs) (e.g., Emanuel et al., 1994; Neelin and Yu, 1994; Tian and Ramanathan, 2003). So the GMS in those days was examined for CCEW dynamics. The popularity of this kind of GMS studies, however, has waned[2] because (i) many observational studies found that the contribution of a second baroclinic mode to CCEWs is significant [see a review by Kiladis et al. (2009)], (ii) some studies pointed out that the SQE is not an accurate assumption specifically in the spatial-temporal scales of CCEWs (e.g., Brown and Bretherton, 1997; Raymond and Herman, 2011), and (iii) alternative theories explained better CCEW dynamics (e.g., Mapes, 2000; Khouider and Majda, 2006; Raymond and Fuchs, 2007; Kuang, 2008b; Herman et al., 2016). Although one GMS theory waned, the GMS itself has, in contrast, flourished more than ever because another theory was engendered; that is a moisture-mode

[2]Although this GMS-wave theory became less popular, it doesn't necessarily mean a denial of the theory. For instance, Frierson et al. (2011) found the GMS predicts the phase speed of the Kelvin waves produced in a relatively realistic model framework. It has not been elucidated whether this is a providential coincidence or is controlled by some unknown mechanisms.

theory.

Recently, the GMS has gained increasing attention because the idea is growing and being accepted that the Madden-Julian oscillation (MJO) is a moisture mode (e.g., Neelin and Yu, 1994; Sobel et al., 2001; Sobel and Gildor, 2003; Fuchs and Raymond, 2002, 2005, 2007; Raymond and Fuchs, 2007; Sugiyama, 2009a,b; Sobel and Maloney, 2012, 2013; Adames and Kim, 2016). This theory states that a moisture mode (thus the MJO) is destabilized only[3] when the GMS is effectively negative. So now, the motivation for GMS analyses has been changed from the CCEW-oriented one into the moisture-mode-oriented one. Because the diminishment of one GMS theory and the birth of the other GMS theory were happening simultaneously, it caused some confusion as to GMS studies in general.

Furthermore, the association between the GMS and moisture-mode stability is also rather confusing. The moisture-mode theory is based on linear stability analysis. The method of the linear stability analysis consists of introducing sinusoidal disturbances on the "background" state to be examined and determining whether the background state demands the growth or decay of the introduced disturbances. Thus, what determines the stability of some modes are its background state, and the GMS relevant to the moisture-mode stability has to be background GMS as the words "gross" and "stability" imply[4]. But, what is the background GMS, and how can we estimate it in the real world? Some previous studies employed field campaign data conducted over a large spatial domain, and computed the GMS

[3]In some studies, the effectively negative GMS is both the necessary and sufficient conditions for the destabalization.

[4]Hannah et al. (2016) claimed that the name "gross moist stability" is misleading because computed GMS doesn't necessarily represent "gross" properties or "stability" of the system.

with it (e.g., Sobel et al., 2014; Inoue and Back, 2015b; Sentić et al., 2015), but does it represent the background properties appropriately? Those questions, which have not fully answered yet, make the GMS a vexing concept.

In this study, we first let ourselves step back a little and look at the GMS from a different perspective than both the CCEW-oriented one and the moisture-mode-oriented one. Instead of considering the wave propagation or instability, we will answer a fundamental question about the GMS: "Provided we have some observational data and we can compute the GMS with it, then what does it physically represent, and how can it be useful?" We believe answering this question will help us better understand the GMS-related theories. We will then, further our argument toward a theoretical aspect, and discuss how our results are relevant or irrelevant to the moisture-mode theory.

There are two main purposes of this study:

1. to clarify a way in which the GMS is useful as a diagnostic tool,

2. to propose a new diagnostic framework for examining transitions of the GMS throughout a convective life-cycle.

The GMS has a crucial pitfall as a diagnostic tool. The GMS is defined as a fractional quantity whose denominator can switch its sign, causing singularities involving blow-ups. Thus, the values of the GMS generally don't make any sense when the denominator is small or the convection is weak. In order to avoid this pitfall, the past studies took two approaches for investigating temporal variability of the GMS: (i) smoothing data and removing points with small values of the denominator (e.g.,

Sobel et al., 2014; Benedict et al., 2014; Sentić et al., 2015; Inoue and Back, 2015b), or (ii) taking a binning average of the numerator and denominator separately and computing the ratio between them (e.g., Hannah and Maloney, 2011, 2014). In this study, we will propose an alternative diagnostic framework which we refer to as the "GMS plane" in which a transition of the GMS can be illustrated in a meaningful way throughout the whole convective life-cycle. This idea was outlined in the summary section of Inoue and Back (2015b). The methodology presented here is applicable to all kinds of data sets, including field observations, re-analysis data, model outputs, and satellite data with which we demonstrate in this study.

The rest of this paper is structured as follows. Since this study is verification and extensions of the ideas proposed by Inoue and Back (2015b), we briefly summarize them in the next section. Section 4.3 presents the descriptions about the data sets and the choice of the spatial domains for the analyses. Using those data sets, we verify the proposed ideas in section 4.4. We also propose a novel diagnostic framework which we refer to as the GMS plane to better illustrate transient properties of the GMS throughout a convective life-cycle. Furthermore, in the same section, we extend our arguments toward the properties of quasi-time-independent GMS, and show geographic variability of it. A thorough discussion about the GMS plane analysis is presented in section 4.5, and a comparison between our results and the moisture-mode theory is discussed in section 4.6. Section 4.7 summarizes this study.

4.2 Summary of Inoue and Back (2015b)

Following Yanai et al. (1973), we start with the vertically integrated energy and moisture budget equations:

$$\frac{\partial \langle s \rangle}{\partial t} = -\nabla \cdot \langle s\mathbf{v} \rangle + \langle Q_R \rangle + LP + H, \tag{4.1}$$

$$\frac{\partial \langle Lq \rangle}{\partial t} = -\nabla \cdot \langle Lq\mathbf{v} \rangle + LE - LP, \tag{4.2}$$

where $s \equiv c_p T + gz$ is dry static energy (DSE); $c_p T$ is enthalpy; gz is geopotential; Q_R is radiative heating rate; L is the latent heat of vaporization; P is precipitation; H is surface sensible heat flux; q is water vapor mixing ratio; E is surface evaporation; the angle brackets represent a mass-weighted column-integration from surface pressure to 100 hPa; and the other terms are in accordance with the meteorological conventions. We neglected the residual of those equations.

Since column DSE anomalies are much smaller than precipitable water anomalies in the deep tropics, adding Eqs. 4.1 and 4.2 approximately yields

$$\frac{\partial \langle Lq \rangle}{\partial t} \simeq -\nabla \cdot \langle h\mathbf{v} \rangle + \langle Q_R \rangle + S, \tag{4.3}$$

where $h \equiv s + Lq$ is moist static energy (MSE) and $S \equiv LE + H$ is surface fluxes (generally H is negligible).

As claimed by past studies, there is a positive correlation[5] between precipitation

[5]The actual relationship is in a nonlinear form (exponential or power law). This study is not sensitive to those details.

and precipitable water. Thus we have the following proportionality:

$$\frac{\partial P}{\partial t} \sim \frac{\partial \langle q \rangle}{\partial t}. \tag{4.4}$$

This relationship indicates that when the RHS of Eq. 4.3 is positive/negative, the convection amplifies/decays. Although this seems to be an oversimplification, we will show it predicts convective amplification and decay very well. It must be cautioned here that the words "amplification" and "decay" in this study are used in such a way that they are distinct from the words "destabilization" and "stabilization" of linear modes, and thus those must not be confused with each other.

Inoue and Back (2015b) did not examine Eq. 4.3 as it is, but they divided it by $\nabla \cdot \langle s\mathbf{v} \rangle$, which represents the intensity of convection (or convective heating), converting the MSE budget equation into an efficiency equation:

$$\nabla \cdot \langle s\mathbf{v} \rangle^{-1} \frac{\partial \langle Lq \rangle}{\partial t} \simeq -\left(\Gamma - \Gamma_C\right), \tag{4.5}$$

where

$$\Gamma \equiv \frac{\nabla \cdot \langle h\mathbf{v} \rangle}{\nabla \cdot \langle s\mathbf{v} \rangle}, \tag{4.6}$$

$$\Gamma_C \equiv \frac{D}{\nabla \cdot \langle s\mathbf{v} \rangle}, \tag{4.7}$$

$D \equiv \langle Q_R \rangle + S$ is the diabatic source[6]. Γ is the (normalized) GMS, and Γ_C is an

[6]In Inoue and Back (2015b), this was called the diabatic "forcing". But the word "forcing" might be misleading because radiative heating and surface fluxes are, to some extent, an intrinsic property of convection instead of external "forcing". Thus we simply call it the diabatic (MSE) source in this

analogue of the GMS named the critical GMS by Inoue and Back (2015b), which represents the contribution of the diabatic source to column moistening. $\Gamma - \Gamma_C$ is collectively called the drying efficiency because it represents the efficiency of the loss of water vapor due to convection. This drying efficiency seems to be a version of the effective GMS (e.g., Su and Neelin, 2002; Bretherton and Sobel, 2002; Peters and Bretherton, 2005; Sobel and Maloney, 2012; Adames and Kim, 2016), and is close to the effective GMS used by Hannah and Maloney (2014). However, the drying efficiency computed in this study must be viewed as a different quantity from the effective GMS used in theoretical studies. We clarify the distinction between them, together with the distinction between the GMS computed diagnostically and the theoretical GMS, in section 4.6.

Equation 4.5 has two benefits that Eq. 4.3 doesn't possess. First, because Eq. 4.5 is independent of a convective intensity, we can take composites of all convective events with different intensities. According to Eqs. 4.4 and 4.5, we can define two convective phases:

$$\Gamma - \Gamma_C < 0, \tag{4.8a}$$

$$\Gamma - \Gamma_C > 0, \tag{4.8b}$$

namely, the amplifying phase and the decaying phase, respectively. These relationships hold only when the denominator of the drying efficiency, $\nabla \cdot \langle s\mathbf{v} \rangle$, is positive. We generalize this condition to include the whole convective life-cycle by introducing the "GMS plane" in section 4.4.3.

study.

The second benefit, which we verify in section 4.4.2, is that the critical GMS Γ_C turns out to be relatively constant compared to the GMS and drying efficiency. That simplifies the phases of Eqs. 4.8a and 4.8b into

$$\Gamma - \gamma < 0, \tag{4.9a}$$

$$\Gamma - \gamma > 0, \tag{4.9b}$$

where γ is some constant that is explained in more detail in sections 4.4.2 and 4.4.4. Those phases indicate that when the GMS is smaller/bigger than some critical constant, the convection amplifies/decays.

4.3 Data description

From satellite views, we can observe the RHSs of the following equations:

$$\nabla \cdot \langle s\mathbf{v} \rangle \simeq \langle Q_R \rangle + LP + H, \tag{4.10}$$

$$\nabla \cdot \langle h\mathbf{v} \rangle \simeq \langle Q_R \rangle + S - \frac{\partial \langle Lq \rangle}{\partial t}. \tag{4.11}$$

In these equations, the column DSE tendency, which is much smaller than the other terms (e.g., Inoue and Back, 2015b), was neglected. By using satellite-based data, we can compute the GMS Γ, critical GMS Γ_C and drying efficiency $\Gamma - \Gamma_C$ as follows:

$$\Gamma = \frac{\langle Q_R \rangle + S - \partial \langle Lq \rangle / \partial t}{\langle Q_R \rangle + LP + H}, \tag{4.12}$$

$$\Gamma_C = \frac{\langle Q_R \rangle + S}{\langle Q_R \rangle + LP + H}, \tag{4.13}$$

$$\Gamma - \Gamma_C = -\frac{\partial \langle Lq \rangle / \partial t}{\langle Q_R \rangle + LP + H}. \tag{4.14}$$

The values of $\nabla \cdot \langle s\mathbf{v} \rangle$ and $\nabla \cdot \langle h\mathbf{v} \rangle$ were computed as the residual of Eqs. 4.10 and 4.11. The procedures of the data treatments are summarized in Fig. 4.1, which consist of three steps: removal of diurnal cycles, spatial average, and removal of seasonality.

Diurnal cycles need to be removed from all the budget terms otherwise we cannot neglect the column DSE tendency (e.g., Inoue and Back, 2015b). The methodologies of diurnal-cycle removal depend on the data sets, which are described more specifically in the next subsection. The spatial grid size was changed into $2^\circ \times 2^\circ$ by taking a spatial average in order to minimize sampling errors. Furthermore, we removed seasonality (or variability with periodicity longer than a month) from all the terms because this study's primary interests are the mechanisms of convective disturbances in the tropical convergence zones that move meridionally along seasons, and because we want to minimize the effects of the seasonal convergence-zone shift. More detailed descriptions of the data procedures are presented in the following.

4.3.1 Data source and procedure

Precipitable water The precipitable water retrievals used in this study are derived from the TRMM Microwave Imager (TMI), a series of Special Sensor Microwave Imager (SSM/I F13, F14, F15, and F16) on Defense Meteorological Satellite Program (DMSP) satellites, and Advanced Micro-wave Scanning Radiometer-Earth Observ-

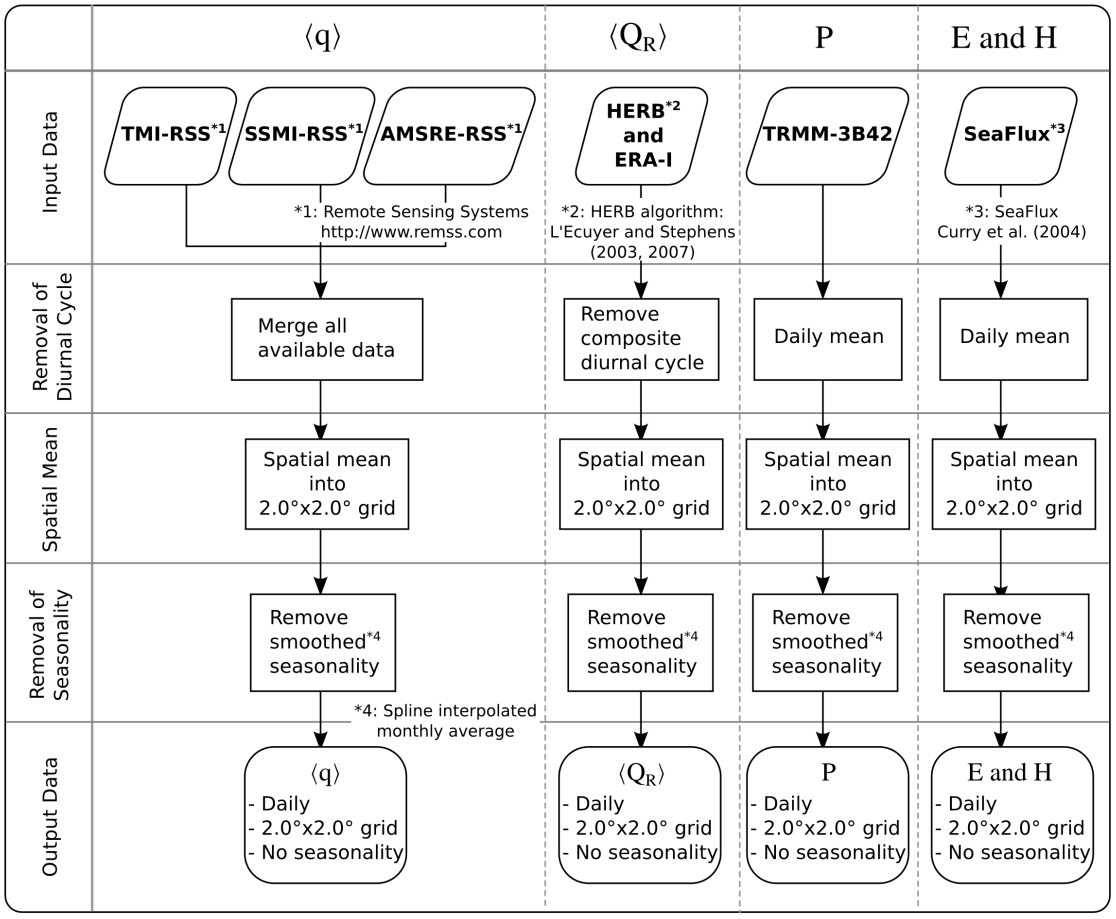

Figure 4.1: Flowchart of the data procedures. See the text for detail.

ing System (AMSR-E) on *Aqua*. The data sets are provided by Remote Sensing Systems (RSS; Wentz et al., 2012, 2014, 2015).

For removing the diurnal cycles, we took an ensemble average of all the precipitable water data from the different satellite sensors listed above. Since each sensor flies over a given place at different local time, and diurnal cycles of precipitable water are not so large (not shown here), we expect this method minimizes the

contamination due to the diurnal cycles. This method also allows us to obtain daily precipitable water data over the entire tropical ocean so that we can compute a snapshot of precipitable water tendency with center differencing over two days at any time and place over the whole tropical ocean. The precipitable water tendency data ($0.25^\circ \times 0.25^\circ$ grids) was spatially averaged into $2^\circ \times 2^\circ$ grids.

Next, we removed variability with periodicity longer than one month as follows. First, we took a monthly average of the anomalies of the data to construct a monthly anomalous time-series. Then by applying a spline interpolation to that monthly time-series, we constructed a smoothed seasonality time-series at each day, which was subtracted from the daily data. By this method, we expect the effects associated with the seasonal ITCZ shift are minimized. This methodology also removed most of the MJO variability from the data set. Analyses of MJO variability will be done separately in our future work.

Radiative heating The radiative heating estimates based on the TMI are derived with the algorithm called the Hydrologic cycle and Earth's Radiation Budget (HERB: L'Ecuyer and Stephens, 2003, 2007). The raw data used here, which exists only over the TMI swath, is instantaneous, $0.5^\circ \times 0.5^\circ$ averages. For a vertical integration, we used the geopotential data from the Interim European Center for Medium-Range Weather Forecasts Re-analysis (ERA-Interim; Dee et al., 2011), which is the only non-satellite data we used in this study. The grid size of the geopotential ($\sim 0.7^\circ \times 0.7^\circ$) was changed into the same one as the radiative heating with a linear interpolation.

The diurnal cycles of the column radiative heating were computed based on the property of a sun-asynchronous TRMM orbit. We constructed the climatological

diurnal cycles at each place by sorting the data array into 6-hourly bins, and taking an average within those bins. Those constructed diurnal cycles were removed from the raw data at each place. The column radiative heating data with diurnal cycles removed was spatially averaged into $2^\circ \times 2^\circ$ grids. Finally, the seasonality computed with a spline interpolation was removed in the same way as for the precipitable water.

Precipitation For precipitation, we used version 7 of daily TRMM Multi-satellite Precipitation Analysis (TMPA) known as the 3B42 product (Huffman et al., 2007, 2010). The daily raw data given in $0.25^\circ \times 0.25^\circ$ grids was spatially averaged into $2^\circ \times 2^\circ$ grids, and a smoothed seasonality was removed in the same way as described above.

Surface fluxes The surface flux data including surface sensible heat flux and surface evaporation was obtained from SeaFlux (Curry et al., 2004), which is a data set relying almost exclusively on satellite observations. The 6-hourly, $0.25^\circ \times 0.25^\circ$ raw data was regridded into daily, $2^\circ \times 2^\circ$ grids with a daily and spatial average. Similarly to the other variables, a spline-interpolated seasonality was removed.

4.3.2 Spatial domain for analysis

For the analyses, we chose four spatial domains, depicted in Fig. 4.2, from the basins of the Indian Ocean (IO), the western Pacific Ocean (WP), the central-eastern Pacific Ocean (EP), and the Atlantic Ocean (AO). The regions surrounded by the polygons in Fig. 4.2 are analyzed separately in the following sections.

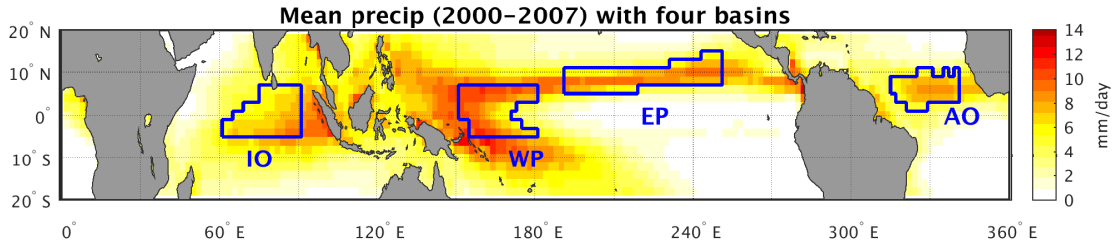

Figure 4.2: Spatial domains for analyses and mean precipitation from 2000 to 2007. Investigated were the grids surrounded by the polygons that were defined as the regions with the mean precipitation greater than 5 mm/day in each oceanic basin: the Indian Ocean (IO), the western Pacific Ocean (WP), the central-eastern Pacific Ocean (EP), and the Atlantic Ocean (AO).

First, we set the rectangular boxes defined by (5°S–5°N, 60°E–90°E), (5°S–5°N, 150°E–180°E), (0°–15°N, 190°E–250°E), (0°–15°N, 300°E–360°E) for IO, WP, EP, and AO, respectively. And the regions with the mean precipitation (from 2000 to 2007) greater than 5 mm/day were chosen for the analyses.

There are 70, 74, 88, and 47 grids surrounded by the boundaries for IO, WP, EP, and AO, respectively. In each domain, we concatenated all 8-yr long time-series from 2000 to 2007 at different grid points into a long data array. This means each data array has, at least, # of grids $\times$ 8-yr $\times$ 365-day $\times$ TMI swath coverage rate ($\sim$ 70%) data points.

4.4 Results

4.4.1 Convective amplification and decay

As in Inoue and Back (2015b), we first verify the idea of the convective amplification/decay phases defined by Eqs. 4.8a and 4.8b. In doing so, we plotted in Fig. 4.3, (a) changes of precipitation over two days, (b) probabilities of increase in precipitation, and (c) precipitation, as a function of the drying efficiency $\Gamma - \Gamma_C$. Because the phases of Eqs. 4.8a and 4.8b hold only when convection is active or $\nabla \cdot \langle s\mathbf{v} \rangle$ is positive, we removed all the data points with $\nabla \cdot \langle s\mathbf{v} \rangle$ less than 50 Wm^{-2} in order to exclude convectively inactive times and to avoid division by zero. Furthermore, 2.5 % outliers from the left and right tails of the PDF of $\Gamma - \Gamma_C$ were also removed to avoid biases due to very large and small values of $\Gamma - \Gamma_C$. In section 4.4.3, we generalize this condition and investigate the whole convective life-cycle.

Figure 4.3a, which shows precipitation changes as a function of $\Gamma - \Gamma_C$, was made as follows. First, we sorted the data array of precipitation changes, computed with a centered difference over two days, in accordance with the order of $\Gamma - \Gamma_C$, and all the data points corresponding to $\nabla \cdot \langle s\mathbf{v} \rangle$ less than 50 Wm^{-2} and 2.5 % outliers of $\Gamma - \Gamma_C$ were removed. That sorted data array was averaged within 5-percentile bins of $\Gamma - \Gamma_C$ to render Fig. 4.3a. Figure 4.3b, which illustrates probabilities of increase in precipitation against $\Gamma - \Gamma_C$, was made similarly. We computed the ratio of the number of events with positive precipitation changes to the total event number within the 5-percentile bins of $\Gamma - \Gamma_C$.

Both Figs. 4.3a and 4.3b strongly support the hypothesis of the convective ampli-

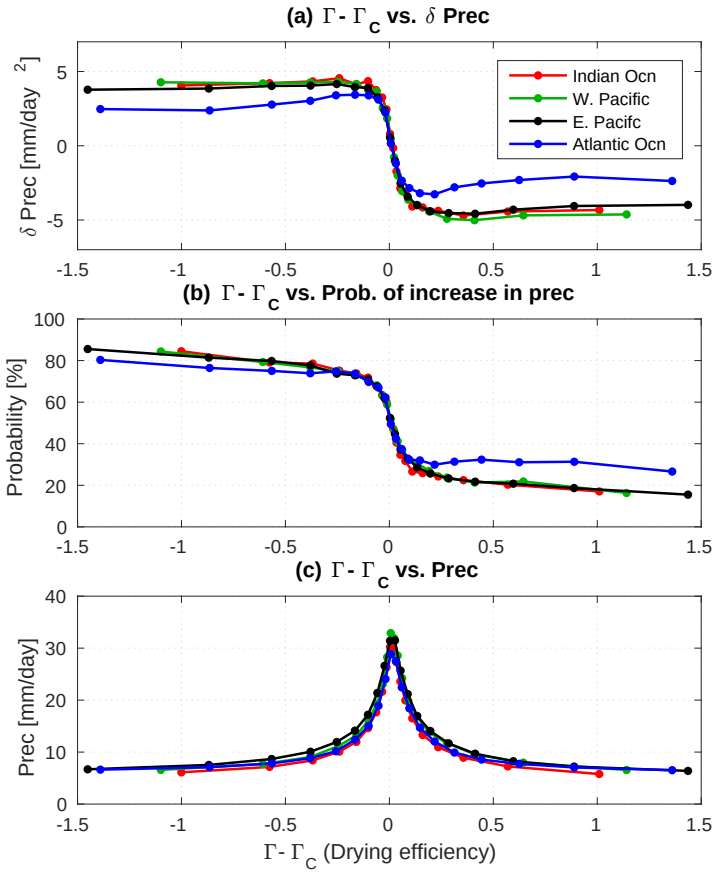

Figure 4.3: (a) Binned precipitation changes as a function of the drying efficiency $\Gamma - \Gamma_C$, averaged in 5-percentile bins of $\Gamma - \Gamma_C$. Temporal precipitation changes δPres were computed with a centered difference over two days. (b) Probabilities of increase in precipitation as a function of $\Gamma - \Gamma_C$, computed in the same bins as (a). (c) Binned precipitation as a function of $\Gamma - \Gamma_C$, computed in the same way as above. Each analysis was conducted over the four oceanic basins, IO (red), WP (green), EP (black), and AO (blue).

fication/decay phases. When the drying efficiency $\Gamma - \Gamma_C$ is negative/positive, the precipitation amplifies/decays in the next day (i.e., positive/negative precipitation changes) at high probability ($\sim$ 80 %), and when $\Gamma - \Gamma_C$ changes its sign, the phase

abruptly switches. This pattern is robust among all the oceanic basins.

When considering significant scatters in P-vs-$\langle q \rangle$ scatter plots in general, the assumption of the positive correlation between P and $\langle q \rangle$ in Eq. 4.4 seems to be an oversimplification. In spite of the seemingly oversimplified assumption, the amplifying/decaying phases defined by $\Gamma - \Gamma_C$ were far more robust than we expected. In fact, we found the relationship between $\partial P/\partial t$ and $\partial \langle q \rangle/\partial t$ in Eq. 4.4 holds at 74.4% in the data set we used (i.e., increase/decrease in precipitable water predicts amplification/decay of convection at 74.4%). This significant predictability is not obvious from scatter plots of P-vs-$\langle q \rangle$ in general.

Figure 4.3c illustrates precipitation as a function of $\Gamma - \Gamma_C$, rendered with the same binning method as the others. In the amplifying phase (i.e., $\Gamma - \Gamma_C < 0$), the precipitation increases as $\Gamma - \Gamma_C$ becomes less negative and reaches the maximum when $\Gamma - \Gamma_C$ is zero, or Γ is equal to Γ_C; in the decaying phase (i.e., $\Gamma - \Gamma_C > 0$), the precipitation decreases with increase in $\Gamma - \Gamma_C$. The occurrence of the maximum precipitation at $\Gamma = \Gamma_C$ is obvious from Figs 4.3a and 4.3b; when Γ is smaller/greater than Γ_C convection amplifies/decays, thus the local maximum must happen at $\Gamma = \Gamma_C$. This is simply rooted in the fact that the local maximum of precipitation happens when precipitable water tendency is close to zero.

In the next subsection, we show that Γ_C can be approximated as a constant in the satellite data used. This indicates that the phase of convection is determined by the criticality of the GMS (i.e., whether Γ is greater or less than some critical constant). This is why we refer to Γ_C as the critical GMS.

4.4.2 Constancy of critical GMS

Figure 4.4 shows scatter plots for the diabatic source ($D \equiv \langle Q_R \rangle + S$) and divergence of column MSE ($+\nabla \cdot \langle h\mathbf{v} \rangle$) as a function of divergence of column DSE ($+\nabla \cdot \langle s\mathbf{v} \rangle$) over the four oceanic basins. The color shade represents the base-10 logarithm of the number of occurrences within 12.5 Wm^{-2} $\times$ 25.0 Wm^{-2} grids of D (or $\nabla \cdot \langle h\mathbf{v} \rangle$) and $\nabla \cdot \langle s\mathbf{v} \rangle$. The black dashed line in each panel was computed with regression through the origin, and the gray line was computed with the binning average within 200 Wm^{-2}-wide bins of $\nabla \cdot \langle s\mathbf{v} \rangle$.

It can be seen in the left column of Fig. 4.4 that the scatter of D is concentrated along the regression line through the origin, and this pattern is similar among all the oceanic basins with sightly varying regression slopes. This linear trend of D appears to be robust especially when compared with the scatter of $\nabla \cdot \langle h\mathbf{v} \rangle$ in the right column. Thus, we can approximate D as

$$D \simeq \gamma \nabla \cdot \langle s\mathbf{v} \rangle. \tag{4.15}$$

Strictly speaking, γ is not a constant, but slightly varies depending on the value of $\nabla \cdot \langle s\mathbf{v} \rangle$ as depicted in the gray binned lines. But the regression lines capture well the overall trend of the scatter of D. Therefore, as proposed in section 4.2, we can approximate the critical GMS (Eq. 4.7) to be γ, which is a constant relevant to the characteristic GMS defined by Inoue and Back (2015b) that is discussed in section 4.4.4.

Now we can replace Γ_C in the drying efficiency $\Gamma - \Gamma_C$ with γ, and define the

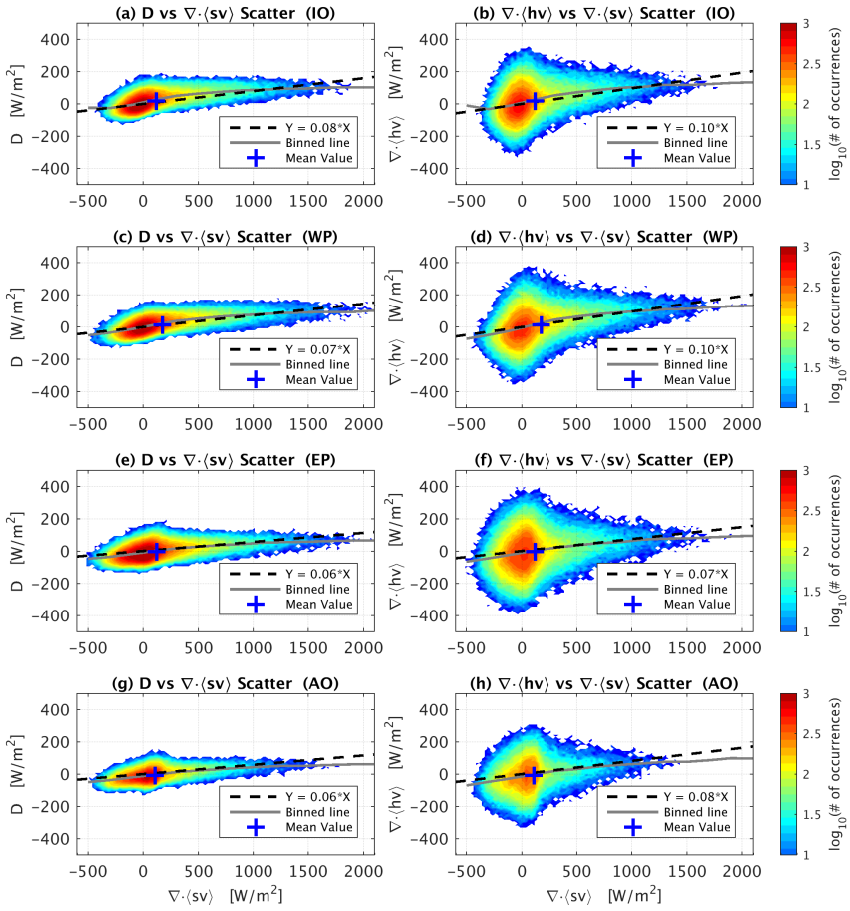

Figure 4.4: (Left column) Scatter plots of diabatic source ($D \equiv \langle Q_R \rangle + S$) against divergence of column DSE ($+\nabla \cdot \langle s\mathbf{v} \rangle$) over the four oceanic basins: (a) IO, (c) WP, (e) EP, and (g) AO. (Right column) As in the left panels, but for divergence of column MSE ($+\nabla \cdot \langle h\mathbf{v} \rangle$). In each panel, the black dashed line was computed with the regression through the origin, and the gray line was computed with the binning average. The blue cross mark indicates the mean value.

amplifying/decaying phases in terms of $\Gamma - \gamma$ as Eqs. 4.9a and 4.9b: Negative/positive $\Gamma - \gamma$ corresponds to the amplifying/decaying phase, respectively. Figure 4.5 verifies this idea, which was made in the same way as Fig. 4.3 but as a function of $\Gamma - \gamma$ instead of $\Gamma - \Gamma_C$. This figure illustrates that $\Gamma - \gamma$ works well to predict the

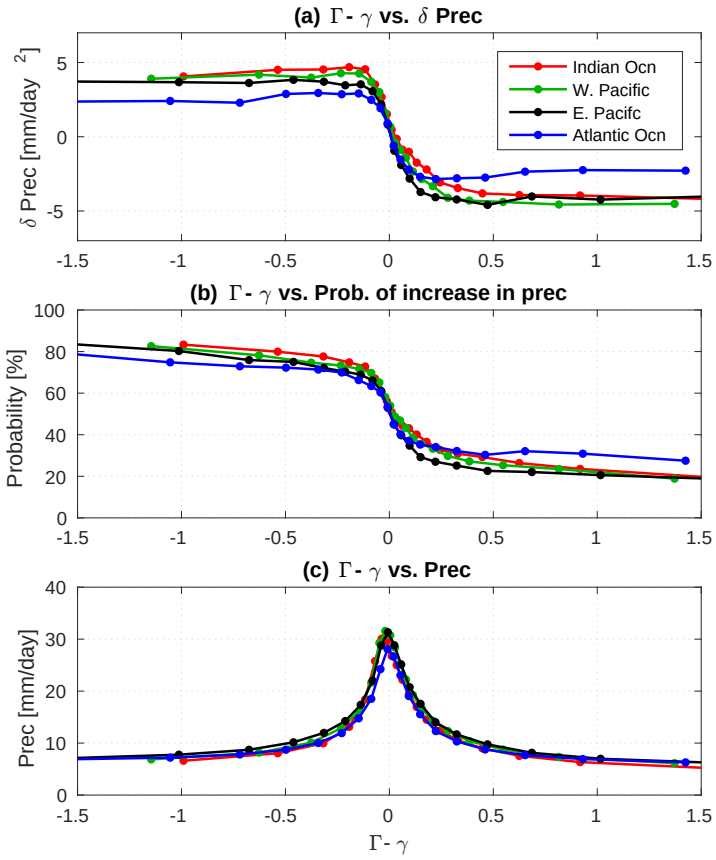

Figure 4.5: As in Fig. 4.3, but the critical GMS Γ_C was replaced with the slopes of the regression lines γ in the left panels of Fig. 4.4.

convective amplification and decay phases among all the oceanic basins. Thus, we can claim that convection will most likely amplify/decay when Γ is less/greater than γ and the local maximum happens at $\Gamma = \gamma$. This means that, if the value of γ is given, the GMS is telling us about whether the convection is amplifying or decaying.

As discussed in sections 4.2 and 4.4.1, the phase relationships in terms of $\Gamma - \gamma$

hold only when $\nabla \cdot \langle s\mathbf{v} \rangle$ is positive. Now we generalize this condition to include the whole convective life-cycle in the next subsection. This can be done by utilizing the linear trend in Eq. 4.15 and introducing a new diagnostic framework which we refer to as the GMS plane.

4.4.3 GMS plane

By assuming the positive correlation between P and $\langle q \rangle$ in Eq. 4.4 and the linear trend of D in Eq. 4.15, we can derive a simple model:

$$\frac{\partial P}{\partial t} \sim \frac{\partial \langle Lq \rangle}{\partial t} \simeq -\nabla \cdot \langle h\mathbf{v} \rangle + \gamma \nabla \cdot \langle s\mathbf{v} \rangle. \tag{4.16}$$

This model is a generalization of the amplifying/decaying phases in Eqs. 4.9a and 4.9b; when $\nabla \cdot \langle s\mathbf{v} \rangle$ is positive, we can divide this by $\nabla \cdot \langle s\mathbf{v} \rangle$ and yield the same relationships as Eqs. 4.9a and 4.9b.

We bear out the validity of this model in Fig. 4.6, in which probabilities of increase in precipitation are plotted in the plane of $\nabla \cdot \langle h\mathbf{v} \rangle$-vs-$\nabla \cdot \langle s\mathbf{v} \rangle$ that we call the "GMS plane". In this plane, the tangent of an phase angle corresponds to the GMS. The probabilities were computed similarly to Fig. 4.3, but now within 2D bins instead of 1D bins. We computed the ratio of the number of events with positive precipitation changes (over two days) to the total event number within 50 Wm^{-2} $\times$ 50 Wm^{-2} bins of $\nabla \cdot \langle h\mathbf{v} \rangle$ and $\nabla \cdot \langle s\mathbf{v} \rangle$. The regression lines through the origin and the binned lines are identical to those in the left column of Fig. 4.4. The slopes of the regression lines correspond to γ, which is the approximated critical GMS Γ_C.

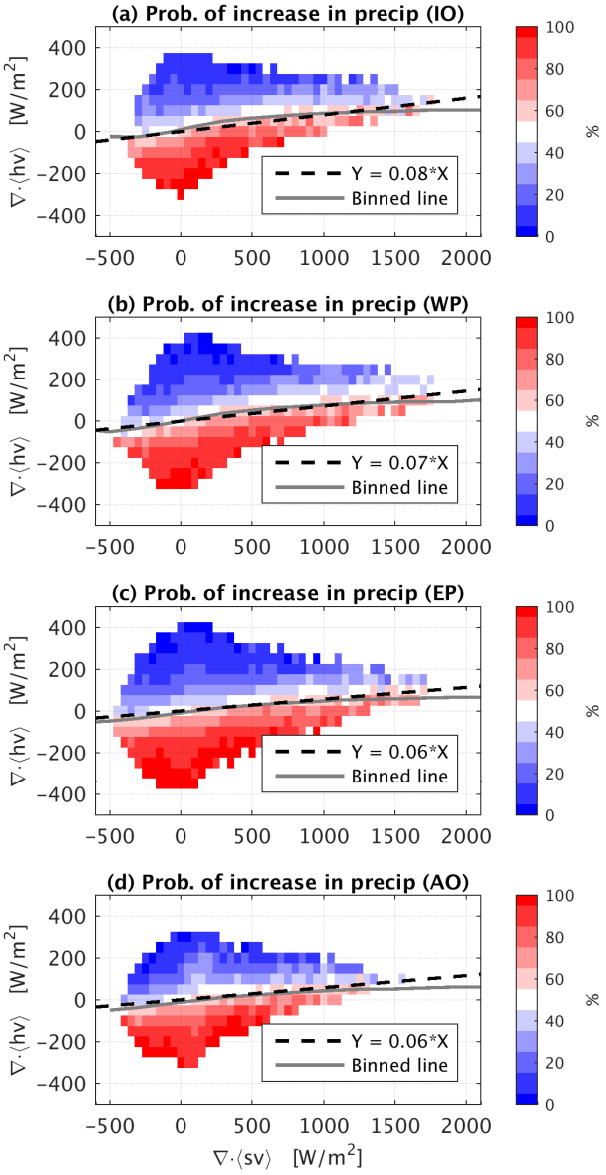

Figure 4.6: (a)–(d) Probabilities of increase in precipitation within grids of $\nabla \cdot \langle h\mathbf{v} \rangle$ and $\nabla \cdot \langle s\mathbf{v} \rangle$ over the four oceanic basins. The probabilities were calculated within 50 Wm^{-2} $\times$ 50 Wm^{-2} grids. The black dashed lines and the gray lines are identical to those in the left panels of Fig. 4.4.

It is clear in this figure that the grids below/above the critical line (or the regression line) exhibit high/low probabilities of convective amplification, and there is an abrupt transition near the critical line. This figure strongly supports the validity of the model in Eq. 4.16; the grids below/above the critical line correspond to positive/negative RHS of Eq. 4.16, thus to the amplification/decay of convection, respectively. Figure 4.6 is a generalized version of Fig. 4.3b.

This GMS plane is useful particularly because it acts like a phase plane. If a data point lies below the critical line, the convection will most likely intensify in the next day, thus the data point will move toward the right in the GMS plane; in contrast, a data point above the critical line will move toward the left. Furthermore, we know that precipitation reaches the maximum on the critical line (i.e., $\Gamma = \gamma$) from Fig. 4.5c. Thus, we expect that convective life-cycles in the GMS plane look like orbiting fluctuations around the critical line. This idea is illustrated in Fig. 4.7, which shows the mean values of temporal changes of $\nabla \cdot \langle h\mathbf{v} \rangle$ and $\nabla \cdot \langle s\mathbf{v} \rangle$ as vector arrorws at each grid in the GMS plane. The mean values were computed within 100 $\mathrm{Wm^{-2}} \times 100\ \mathrm{Wm^{-2}}$ bins. This figure illustrates that the GMS plane is a phase plane in which each convective life-cycle tends to orbit around the critical GMS line. This is an alternative depiction of a GMS transition to plotting a time-series of it. In general, computation of the GMS becomes troublesome when its denominator is small. Depicting a GMS transition as a phase transition in the GMS plane can avoid the computational problem of the GMS, thus we can apply this methodology to the whole convective life-cycle. Another meaningful method of depicting a GMS transition is plotting a time-series of the arc-tangent of the GMS rather than the

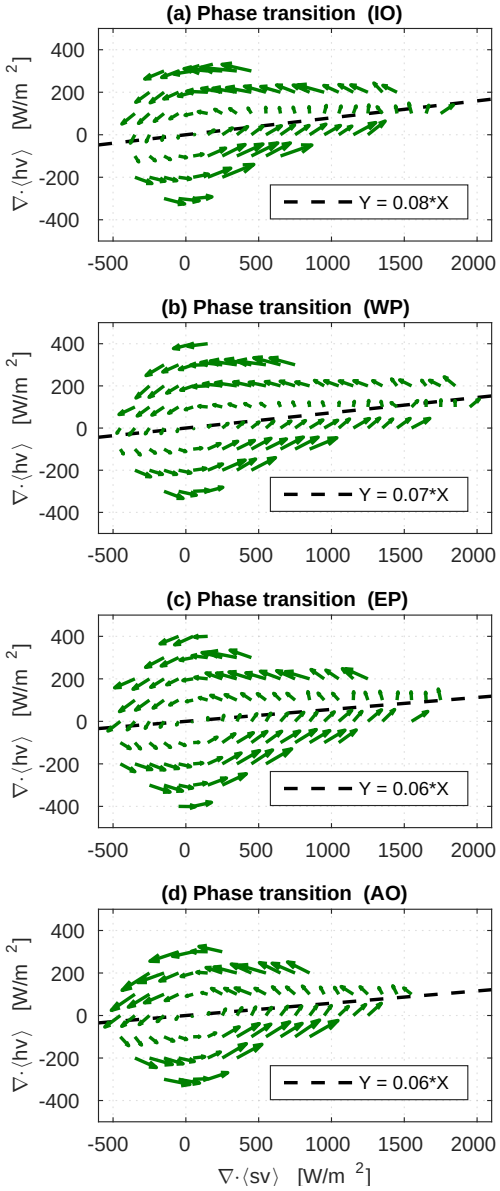

Figure 4.7: (a)–(d) Mean values of temporal changes of $\nabla \cdot \langle h\mathbf{v} \rangle$ and $\nabla \cdot \langle s\mathbf{v} \rangle$ (with a centered difference) at each grid in the GMS plane, represented in vector arrows, over the four domains. The mean values were calculated within 100 Wm^{-2} $\times$ 100 Wm^{-2} grids. The dashed lines are identical to those in the left panels of Fig. 4.4 and Fig. 4.6.

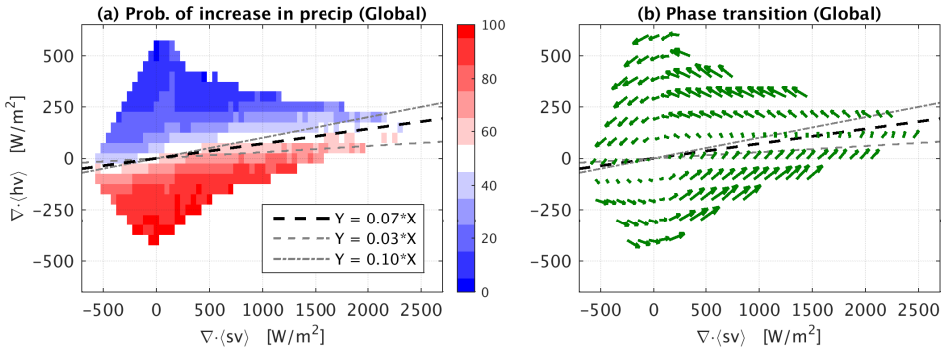

Figure 4.8: (a) As in Fig. 4.6, but for the whole tropical convergence zone with the mean precipitation greater than 5 mm/day (the colored regions in Fig. 4.9). (b) As in Fig. 4.7, but for the whole tropical convergence zone. The slope of the black dashed line was computed similarly to that in Figs. 4.6 and 4.7, and the two gray lines represent the geographic variability of the critical GMS.

values of the GMS. The arc-tangent of the GMS, which also avoids the singularities of the GMS, represents a phase angle in the GMS plane, thus depicts the same information as the phase plane plot.

Since the behaviors illustrated in Figs. 4.6 and 4.7 are robust among all the oceanic basins with slightly varying regression slopes, we plotted in Fig. 4.8 those for the whole oceanic regions where the mean precipitation is greater than 5 mm/-day. The gray dashed and dotted lines in it represent the range of the geographic variability of a regression slope γ. This figure summarizes important aspects of the GMS: When considering $\nabla \cdot \langle s\mathbf{v} \rangle > 0$ and $\nabla \cdot \langle s\mathbf{v} \rangle < 0$ cases separately, the value of the GMS (i.e., phase position in the GMS plane) has a capability to predict the subsequent convective evolution, and that law is quite universal throughout the whole tropical ocean. In the next subsection, we discuss the geographic variability of a regression slope γ, which is relevant to the characteristic GMS defined by Inoue

and Back (2015b).

4.4.4 Characteristic GMS

Thus far, we have discussed a time-dependent aspect of the GMS. Now let us discuss the quasi-time-independent GMS, which we refer to as the characteristic GMS. We have shown that the diabatic source ($D \equiv \langle Q_R \rangle + S$) can be approximated as $\gamma \nabla \cdot \langle s\mathbf{v} \rangle$. This linear relation can be decomposed into two equations:

$$\langle Q_R \rangle \simeq \gamma_R \nabla \cdot \langle s\mathbf{v} \rangle + \beta_R, \tag{4.17}$$

$$S \simeq \gamma_S \nabla \cdot \langle s\mathbf{v} \rangle + \beta_S, \tag{4.18}$$

where the former equation represents the cloud-radiation feedback and the latter represents the convection-evaporation feedback[7]. In those equations, the intercept β_R that is negative roughly cancels out the other intercept β_S, resulting in small $\beta_R + \beta_S$. Therefore, the value of the critical GMS ($\Gamma_C \simeq \gamma$) is equal to the summation of the cloud-radiation feedback constant γ_R and the convection-evaporation feedback constant γ_S.

[7]While the cloud-radiation feedback is well verified by the past literature, the mechanism of the convection-evaporation feedback is less certain. A positive correlation between P and S was pointed out by some observational studies (e.g., Back and Bretherton, 2005; Araligidad and Maloney, 2008; Dellaripa and Maloney, 2015) and cloud resolving model studies (e.g., Bretherton et al., 2005). But as claimed by Back and Bretherton (2005) and Bretherton and Khairoutdinov (2015), this correlation depends on an environmental moisture condition, and sometimes it can be negative.

We compute γ with the regression through the origin as

$$\gamma \equiv \frac{\overline{D * \nabla \cdot \langle s\mathbf{v} \rangle}}{\overline{\nabla \cdot \langle s\mathbf{v} \rangle^2}}, \tag{4.19}$$

where the bar represents a time average. From the MSE energy budget equation (Eq. 4.3) and the fact that covariance between $\partial\langle q \rangle/\partial t$ and $\nabla \cdot \langle s\mathbf{v} \rangle$ is small (because P and $\partial\langle q \rangle/\partial t$ are almost out of phase), we obtain

$$\gamma \simeq \frac{\overline{\nabla \cdot \langle h\mathbf{v} \rangle * \nabla \cdot \langle s\mathbf{v} \rangle}}{\overline{\nabla \cdot \langle s\mathbf{v} \rangle^2}} \equiv \tilde{\Gamma}. \tag{4.20}$$

At the same time, the negligible intercept ($\beta_R + \beta_S \simeq 0$) indicates

$$\tilde{\Gamma} \simeq \frac{\overline{\nabla \cdot \langle h\mathbf{v} \rangle' * \nabla \cdot \langle s\mathbf{v} \rangle'}}{\overline{\nabla \cdot \langle s\mathbf{v} \rangle'^2}} \equiv \tilde{\Gamma}' \tag{4.21}$$

$$\simeq \frac{\overline{\nabla \cdot \langle h\mathbf{v} \rangle}}{\overline{\nabla \cdot \langle s\mathbf{v} \rangle}} \equiv \overline{\Gamma} \tag{4.22}$$

where the prime represents departure from the time mean. Furthermore, we showed that precipitation reaches the local maximum at $\Gamma = \gamma$, thus

$$\gamma \simeq \Gamma_{max}, \tag{4.23}$$

where Γ_{max} is the GMS at the precipitation maximum. In summary, all the GMSs given above, γ, $\tilde{\Gamma}$, $\tilde{\Gamma}'$, $\overline{\Gamma}$, and Γ_{max}, should be close to each other, and we collectively call them the characteristic GMS as in Inoue and Back (2015b).

Now we investigate the geographic variability of the characteristic GMSs. Fig-

ure 4.9 shows the map of the critical GMS γ, computed with Eq. 4.19, only over the oceanic regions with the mean precipitation greater than 5 mm/day. This map exhibits a distinct geographic pattern; the values of γ are slightly higher in the Indian and western Pacific Oceans than in the central-eastern Pacific and Atlantic Oceans.

The other characteristic GMSs, $\tilde{\Gamma}'$ and $\tilde{\Gamma}$, are also plotted in Figs. 4.10a and b, both of which exhibit similar geographic patterns to that of γ in Fig. 4.9. Indeed, the correlations of the spatial pattern of Fig. 4.9 with Fig. 4.10a and b are 0.848 and 0.737, respectively. This agreement is consistent with the argument above. It should be noted that the color scales in Fig. 4.10 are shifted by 0.01 compared with that in Fig. 4.9. That small departure is due to nonzero covariance between $\partial\langle q\rangle/\partial t$ and $\nabla\cdot\langle s\mathbf{v}\rangle$ owing to slight lags between P and $\langle q\rangle$.

The geographic patterns shown in Figs. 4.9 and 4.10 are, to some extent, consistent with the geographic variability of vertical velocity profiles. In general, vertical-velocity-profile shapes are top-heavier (associated with greater GMS) in the Indian and western Pacific Oceans with weaker SST gradient, and bottom-heavier (associated with smaller GMS) in the central-eastern Pacific and Atlantic Oceans with strong SST gradient (e.g., Back and Bretherton, 2006; Sobel and Neelin, 2006; Back and Bretherton, 2009a,b). But it should be noted that the definitions of the characteristic GMSs used here include both the horizontal and vertical components of the GMS, and thus their values cannot be determined solely by vertical velocity profiles. It would be interesting to investigate further the mechanisms which control the geographic patterns of the characteristic GMS.

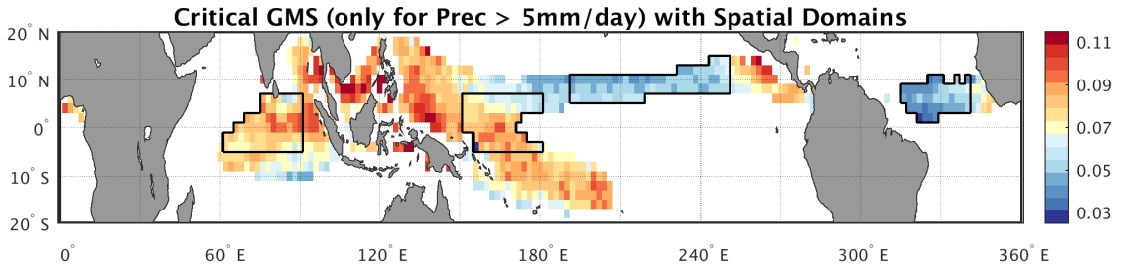

Figure 4.9: Critical GMS (i.e., a regression slope of D against $\nabla \cdot \langle s\mathbf{v} \rangle$) map with the domains for analyses (black polygons) only over the regions with the mean precipitation greater than 5 mm/day.

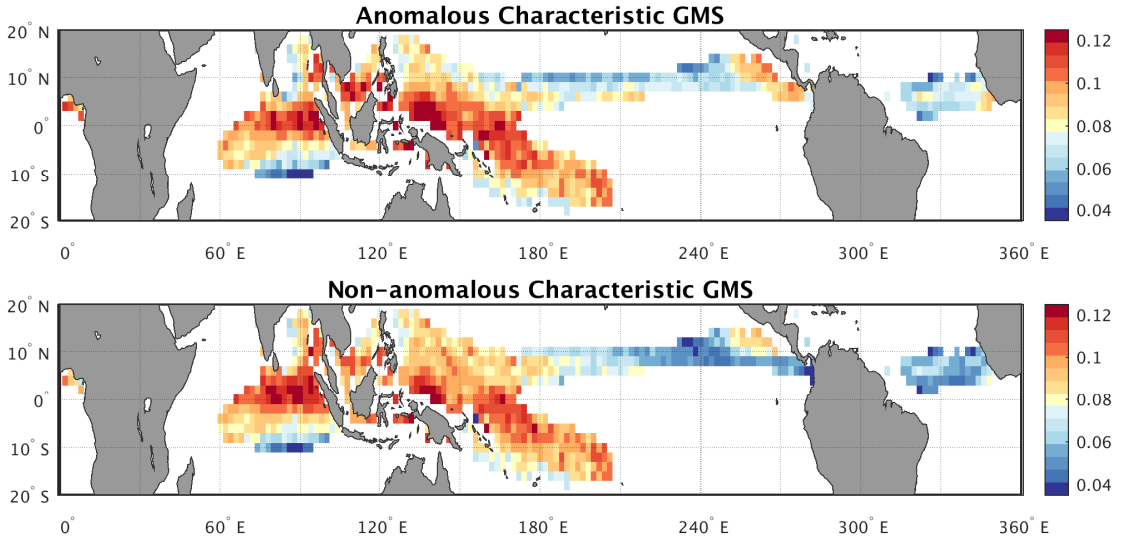

Figure 4.10: (top) Map of anomalous characteristic GMS ($\tilde{\Gamma}'$) over the same regions as shown in Fig. 4.9. (bottom) As in (top), but for non-anomalous characteristic GMS ($\tilde{\Gamma}$). See the text for the definitions of those. It should be noted that the color scales are shifted by $+0.01$ compared with Fig. 4.9.

Although the values of the three characteristic GMSs, γ, $\tilde{\Gamma}'$, and $\tilde{\Gamma}$, are consistent with each other, the climatological GMS $\overline{\Gamma}$ exhibits a quite different geographic pattern as depicted in Fig. 4.11. It shows that $\overline{\Gamma}$ is negative in the eastern Pacific and

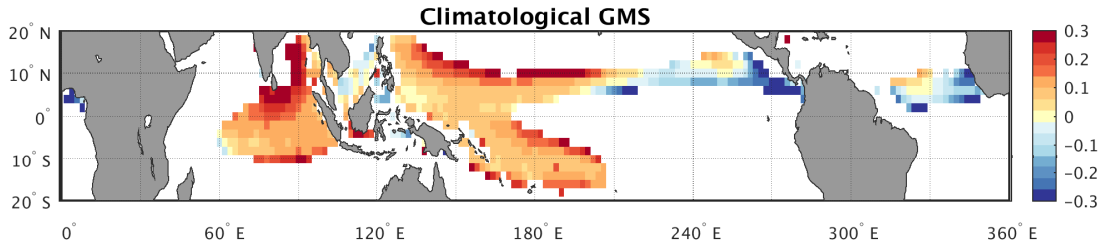

Figure 4.11: As in Fig. 4.10, but for the climatological GMS ($\overline{\Gamma}$). It should be cautioned that the color scale is rather different from those in Figs. 4.9 and 4.10.

Atlantic Oceans and the color scale is far different from those in Figs. 4.9 and 4.10. We claim that this significant discrepancy is due to the sensitivity of this metric to data errors. In Fig. 4.4, the mean values of $(\nabla \cdot \langle h\mathbf{v} \rangle, \nabla \cdot \langle s\mathbf{v} \rangle)$ are plotted with the blue cross-marks. The values of those are (19.3 Wm^{-2}, 118.0 Wm^{-2}), (15.3 Wm^{-2}, 174.9 Wm^{-2}), (-2.1 Wm^{-2}, 120.9 Wm^{-2}), and (-5.9 Wm^{-2}, 107.1 Wm^{-2}), respectively, for IO, WP, EP, and AO. One can notice that the numerator of $\overline{\Gamma}$, $\overline{\nabla \cdot \langle h\mathbf{v} \rangle}$, is a tiny number especially in EP and AO. Thus even a few Wm^{-2} of its errors can cause crucial errors in $\overline{\Gamma}$ with a sign flip. Therefore, we conclude that the metric of the climatological GMS $\overline{\Gamma}$ is so sensitive to data errors that it should not be used as a diagnostic tool especially with observational data involving non-negligible biases.

4.4.5 Underestimation of characteristic GMS

In order to check the reliability of the values of the characteristic GMSs computed with the satellite data, we compared those to the values computed with field campaign data. Two field campaign data sets were investigated: (i) the TOGA

COARE field campaign data constructed by Minghua Zhang with an objective scheme called the constrained variational analysis (Zhang and Lin, 1997), and (ii) version 3a of the Colorado State University quality controlled observations from the DYNAMO field campaign (Johnson and Ciesielski, 2013; Ciesielski et al., 2014a,b; Johnson et al., 2015).

Three characteristic GMSs, $\tilde{\Gamma}'$, $\tilde{\Gamma}$, and γ, defined in the previous subsection, were computed using both the field campaign data sets and the satellite data in the same regions, and compared with each other. It should be noted that there are no overlaps of the observational time periods; the TOGA COARE and DYNAMO field campaigns were conducted, respectively, from 1 November 1992 to 28 February 1993, and from 1 October to 31 December 2011, and the satellite data used here is from 1 January 2000 to 31 December 2007. This inter-comparison is implicitly dependent on the assumption that the characteristic GMSs are quasi-time-independent in the ITCZ.

Another important note is that the surface flux data in the TOGA COARE and DYNAMO data sets were derived in different ways. During TOGA COARE, the surface meteorology was collected from a buoy moored near the center of the domain (Weller and Anderson, 1996) whereas the surface flux data during DYNAMO was obtained from TropFlux (Kumar et al., 2011) whose surface meteorology was derived from the corrected ERA-Interim. Discussion about the differences of those data sets is beyond the scope of this study. In this study, we simply assumed the field campaign data as the "true" data with which the satellite estimates are compared. But it should be noted that Hannah et al. (2016) demonstrated that the field

Table 4.1: Characteristic GMSs. The top two rows were computed with the field campaign data, and the bottom two rows were computed with the satellite data in the same regions as TOGA COARE and DYNAMO, respectively. See the text for the definition of each quantity.

Characteristic GMS	$\tilde{\Gamma}'$	$\tilde{\Gamma}$	γ
TOGA COARE (sounding)	0.257	0.263	0.217
DYNAMO (sounding)	0.171	0.195	0.187
TOGA COARE Region (satellite)	0.110	0.102	0.085
DYNAMO Region (satellite)	0.095	0.106	0.083

campaign sounding array is sometime less accurate due to sparse sampling stations.

The values of the characteristic GMSs are summarized in Table 2.1. Roughly speaking, the values of the different characteristic GMSs are consistent with each other as claimed in the previous subsection. The table shows that the satellite-based ones are approximately half of those computed with the field campaign data. This result indicates that the characteristic GMSs shown in Figs. 4.9 and 4.10 might be underestimated.

This underestimation is associated with the underestimation of both the cloud-radiation feedback and the convection-evaporation feedback. As argued above, γ can be decomposed into the cloud-radiation feedback constant γ_R and the convection-evaporation feedback constant γ_S; the former and the latter are plotted as scatter plots in the left and right columns in Fig. 4.12. The red lines in the first and second row panels were computed with the DYNAMO and the TOGA COARE data, respectively. They show that the satellite-based data used in this study underestimates

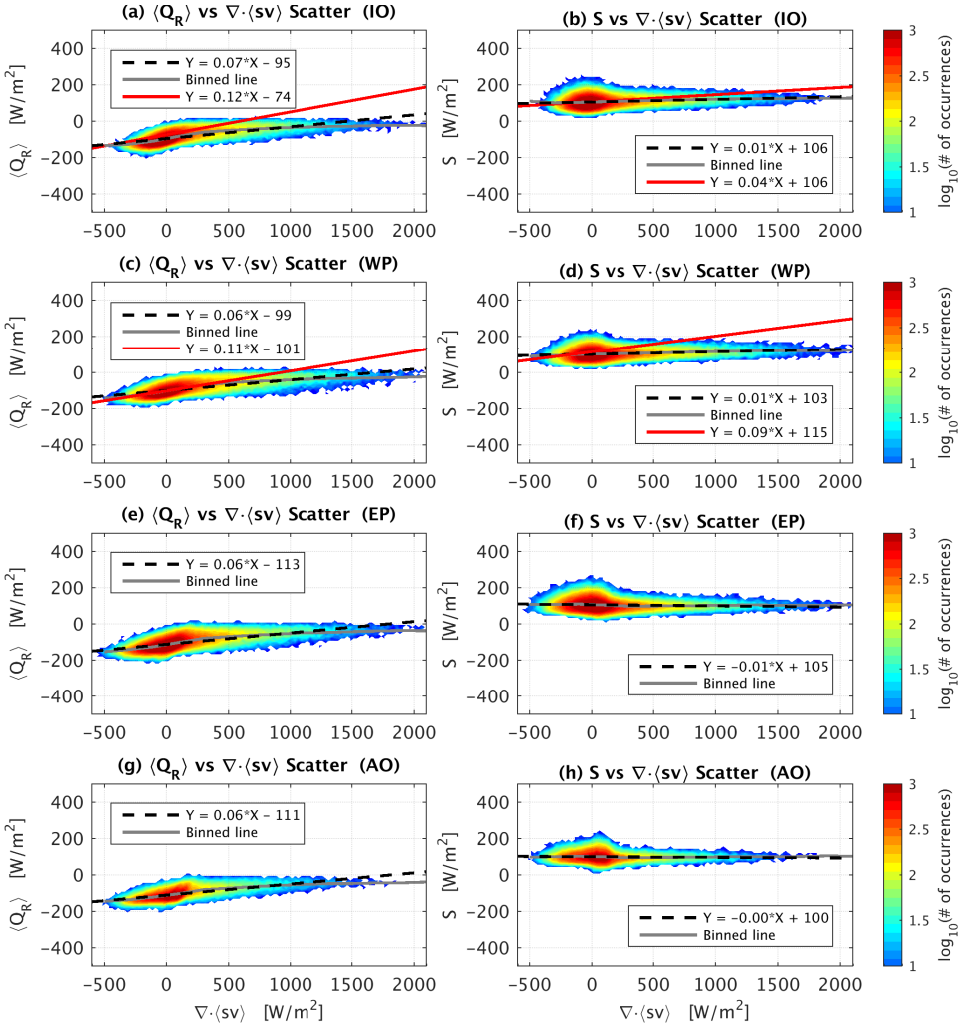

Figure 4.12: (Left column) As in Fig. 4.4, but for $\langle Q_R \rangle$ versus $\nabla \cdot \langle s\mathbf{v} \rangle$ over the four domains: (a) the Indian Ocean (IO), (c) the western Pacific Ocean (WP), (e) the central-eastern Pacific Ocean (EP), and (g) the Atlantic Ocean (AO). (Right column) As in the left column, but for S versus $\nabla \cdot \langle s\mathbf{v} \rangle$. In each panel, the black dashed line was calculated with the least squares method and the binned line (the gray line) was computed in the same way as in Fig. 4.4. The red lines in the panels for IO [(a) and (b)] and WP [(c) and (d)] were computed with the TOGA COARE and DYNAMO field campaign data, respectively.

the linear feedback constants in both the TOGA COARE and DYNAMO regions. And because we estimated $\nabla \cdot \langle h\mathbf{v} \rangle$ and $\nabla \cdot \langle s\mathbf{v} \rangle$ as the residual of the MSE and DSE budget equations, the underestimation of the linear trends of $\langle Q_R \rangle$ and S directly results in the underestimation of the other characteristic GMSs.

However, this underestimation does not change the general conclusions presented in this study; for instance, the underestimated characteristic GMS changes the slopes in Fig. 4.4, but the behavior of the GMS plane discussed previously is still valid. This was verified using the ERA-interim (not shown here).

It should be briefly noted that the values of the characteristic GMSs with the DYNAMO field campaign data are smaller than those given by Sentić et al. (2015), who used the same data as ours. This is simply because they computed the GMS with moist/dry entropy instead of moist/dry static energy. Generally, the GMSs computed with those different metrics exhibit different values, thus should not be compared with each other.

4.5 Discussion: Why is the GMS useful?

4.5.1 Applicability of the GMS plane analysis

The results shown in this study are based on the four simple assumptions:

1. MSE budgets are closed.

2. Column-integrated DSE anomalies are much smaller than precipitable water anomalies.

3. Precipitation is positively correlated with precipitable water.

4. The diabatic source terms can be approximated in a linear form[8] with respect to divergence of column DSE (or precipitation).

The second assumption doesn't rule out the possibility that small temperature anomalies play crucial roles in the dynamics.

As long as those assumptions are satisfied, the GMS phase transitions shown in Figs. 4.6 and 4.7 hold in any types of convective disturbances. The first three assumptions are generally well verified in the tropics. The validity of the last assumption, which is rooted in the linear feedbacks of the cloud-radiation and the convection-evaporation, is partially less certain than the others. The cloud-radiation feedback has been well verified in the past observational studies (e.g., Lin and Mapes, 2004; Inoue and Back, 2015a; Johnson et al., 2015) and implemented in many theoretical models (Sobel and Gildor, 2003; Fuchs and Raymond, 2002; Raymond and Fuchs, 2007; Sugiyama, 2009a; Sobel and Maloney, 2012; Adames and Kim, 2016, and many others). In contrast, the mechanism of the convection-evaporation feedback is not well understood. Nevertheless, both the current study and the study by Inoue and Back (2015b) with the TOGA COARE field campaign data seem to bear out the validity of the fourth assumption, and the results by Sentić et al. (2015) using the DYNAMO field campaign data also supported it even in the MJO time-scale.

[8]The cancellation of the intercepts ($\beta_R + \beta_S \simeq 0$) discussed in section 4.4.4 is not necessary for the results in Figs. 4.6 and 4.7. We can take anomalies of all the budget terms, then the idea of the GMS phase transition in those figures still holds with some x- and y-directional shifts.

Therefore, we believe that the GMS plane analysis has a wide range of applicability, including analyses of convectively coupled equatorial waves (CCEWs) and MJO life-cycles. Another benefit of this analysis is that it is applicable to all kinds of data, involving satellite, reanalysis, field campaign data, and outputs of numerical models. Thus we expect it will provide us with one of standard frameworks of diagnostics for tropical convective disturbances. Furthermore, as suggested in section 4.4.3, depicting a GMS transition as a phase transition in the GMS plane instead of plotting a time-series of it can avoid the computational problem of the GMS due to its singularities, which allows us to investigate the GMS throughout the whole convective life-cycle. Alternatively, it might be meaningful to plot a time-series of the arc-tangent of the GMS. This plot also illustrates a phase transition in the GMS plane in a meaningful way without the singularity problem of the GMS.

4.5.2 What we can learn from the GMS: time-dependent aspect

The GMS can be studied in two ways: as a phase transition in the GMS plane, and as the characteristic GMS. The former is highly time-dependent and the latter is quasi-time-independent. We showed in Figs. 4.6 and 4.7 that the value of the GMS (or phase position in the GMS plane) can predict the subsequent convective evolution. This property is rooted in the model in Eq. 4.16. This model indicates that the pair of $\nabla \cdot \langle h\mathbf{v} \rangle$ and $\nabla \cdot \langle s\mathbf{v} \rangle$ (if γ is given) can estimate $\partial \langle q \rangle / \partial t$, and thus approximate $\partial P / \partial t$ because of the positive correlation between P and $\langle q \rangle$. Now, $\nabla \cdot \langle s\mathbf{v} \rangle$ represents the intensity of convection, and thus can be converted into P.

Therefore, we can claim that the information which the pair of $\nabla \cdot \langle h\mathbf{v} \rangle$ and $\nabla \cdot \langle s\mathbf{v} \rangle$ possess is close to the information deduced from the pair of P and $\partial P/\partial t$ (or $\partial \langle q \rangle/\partial t$). The latter pair has been used in phase plane analyses[9] of convective life-cycles (e.g., Riley et al., 2011; Yasunaga and Mapes, 2012). One important note is that the former pair is both diagnostic terms whereas the latter pair contains a prognostic term. This is theoretically important because it indicates that the advection induced by the current dynamical field predicts the subsequent convective evolution. Furthermore, the former pair is tightly related to large-scale circulations associated with convection. Therefore, we can say that the GMS is an alternative representation of a convective phase, expressed in terms of the quantities relevant to large-scale circulations associated with convection.

In Fig. 4.13, snapshots of $\partial \langle q \rangle/\partial t$, $\langle q \rangle$, and P are plotted. We want to point out that the map of $\partial \langle q \rangle/\partial t$ is rich in structures; charge and discharge of moisture tend to happen in organized systems, some of which exhibit wave-like structures (for instance, in the eastern Pacific around 10°N) and have spatial scales of a few thousand kilometers. This study suggests that the GMS plane analysis is useful for better understanding such moistening processes.

4.5.3 What we can learn from the GMS: quasi-time-independent aspect

The GMS can be also computed in time-independent ways as the characteristic

[9] Hannah et al. (2016) also found that the plane of Lagrangian precipitable water tendency versus precipitable water behaves like a phase plane (see Fig. 15 therein). And its behavior has some commonalities with that of the GMS plane in this study.

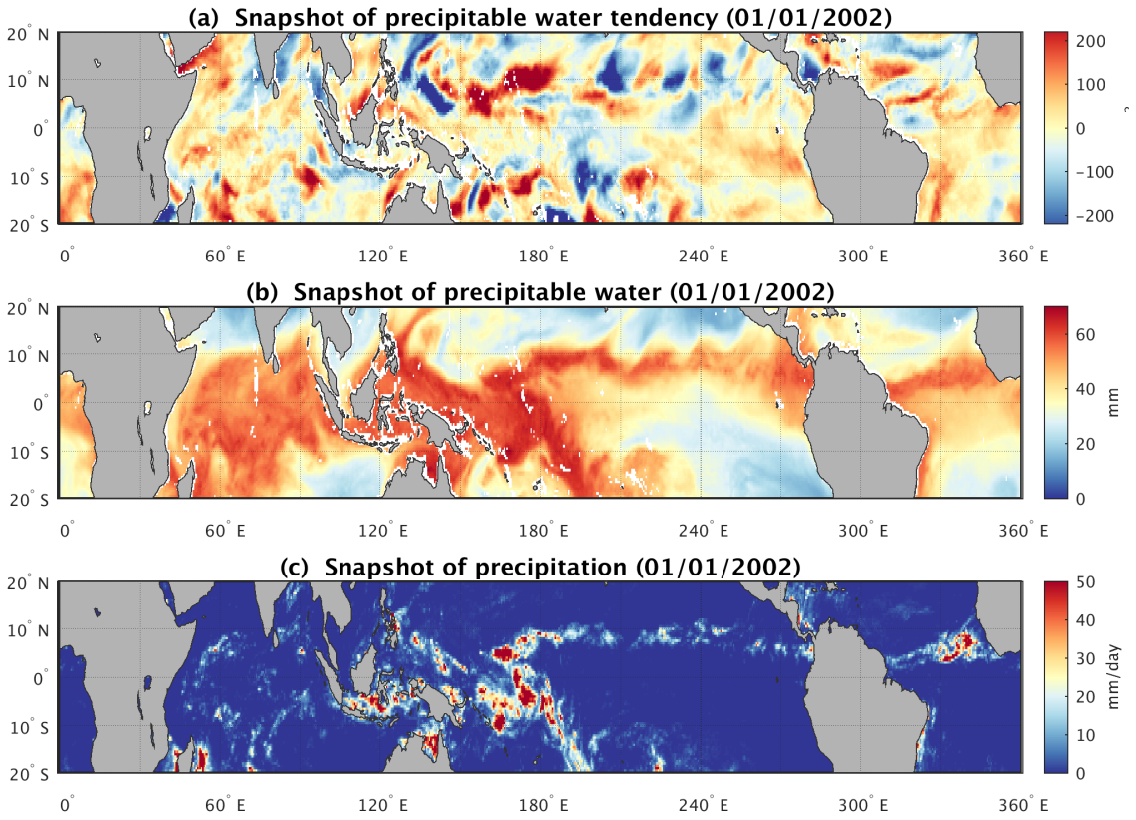

Figure 4.13: (a) Snapshot of precipitable water tendency on 01/01/2002. The unit was converted into the energy unit by multiplying by the latent heat of evaporation. (b) and (c) Snapshots of precipitable water and precipitation on the same day.

GMS. As argued in section 4.4.4, the characteristic GMS can be interpreted as the follows:

1. the threshold value between the amplifying and decaying phases of convection,

2. summation of the cloud-radiation feedback constant and the convection-evaporation feedback constant.

If we ignore horizontal advection for simplicity of the argument, the first interpretation is associated primarily with shapes of vertical velocity profiles at the convective maximum, and secondarily with vertical profiles of MSE. On the other hand, the second interpretation is mainly related to the thermodynamic quantities or the diabatic MSE source terms. These facts imply that vertical velocity profiles and the feedbacks of the diabatic MSE source are very tightly intertwined.

Usually, the (time-independent) GMS is discussed only in the context of MSE advection. But this study suggests that it has a counterpart which also should be discussed; that is the feedbacks between the diabatic source and convection.

4.6 More discussion

In this section, we discuss how our GMS analyses are relevant or irrelevant to the moisture-mode theory. The moisture-mode theory generally states that effectively negative GMS is necessary for the destabilization of the mode (Fuchs and Raymond, 2002; Sobel and Maloney, 2013; Adames and Kim, 2016, among many others). However, unlike this study, the effective GMS is set to be a constant parameter which is determined by the background conditions and model physics. Then, is the temporal variability of the drying efficiency shown in this study, which seems like the effective GMS, relevant to the stability of the moisture mode? The answer is “no”, and “why this is so” is explained below. This discussion is linked to the interpretations of the two distinct GMSs: diagnostic, time-dependent GMS and theoretical, time-independent GMS.

4.6.1 Diagnostic GMS and theoretical GMS

For proceeding with the discussion, we crudely summarize the moisture-mode theory, ignoring some details. The model of the linear moisture mode can be expressed as

$$\frac{\partial P'}{\partial t} = -\left[\Gamma_{\text{eff,r}} + i\Gamma_{\text{eff,i}}\right] P', \tag{4.24}$$

where P' is a precipitation anomaly, and the real component $\Gamma_{\text{eff,r}}$ and the imaginary component $\Gamma_{\text{eff,i}}$ are determined by the model parameters. The choice of these annotations implies that they are associated with the effective GMS. The minus sign is there for consistency with the past literature. We assume P' has the form

$$P'(x,t) = \hat{P}\exp\left[ikx + (\sigma_r + i\sigma_i)t\right], \tag{4.25}$$

where $\hat{P}$ is an amplitude, k is a zonal wavenumber, σ_r and σ_i are real and imaginary frequencies respectively. Plugging Eq. 4.25 into Eq. 4.24 yields $\sigma_r = -\Gamma_{\text{eff,r}}$ and $\sigma_i = -\Gamma_{\text{eff,i}}$. Thus, when $\Gamma_{\text{eff,r}}$ is negative, the mode is destabilized ($\sigma_r > 0$); $\Gamma_{\text{eff,i}}$ is associated with the wave propagation. In all the moisture-mode models, it turns out that $\Gamma_{\text{eff,r}}$ is equal to or close to the effective GMS, indicating the effectively negative GMS is necessary for the destabilization of the moisture mode.

The model parameters, $\Gamma_{\text{eff,r}}$ and $\Gamma_{\text{eff,i}}$, consists of the parametrization of four different components: horizontal MSE advection, vertical MSE advection, radiative heating, and surface fluxes. For elucidating the behavior of the GMS, let's just look at the vertical MSE advection and ignore the horizontal advection for simplicity.

In the context of a linear model, we can express the column-integrated vertical

MSE advection as

$$\langle \omega \partial h/\partial p \rangle' = \left[\Gamma_{\mathrm{v,r}} + i\Gamma_{\mathrm{v,i}} \right] P', \tag{4.26}$$

where ω is vertical pressure velocity. $\Gamma_{\mathrm{v,r}}$ contributes to the stability of the system (i.e., $\Gamma_{\mathrm{eff,r}} = \Gamma_{\mathrm{v,r}} + \text{other terms}$); $\Gamma_{\mathrm{v,i}}$ represents the contribution of the vertical MSE advection to the propagation (i.e., $\Gamma_{\mathrm{eff,i}} = \Gamma_{\mathrm{v,i}} + \text{other terms}$), which is parametrized as frictionally induced moisture convergence or vertical advection by bottom-heavy ω [see Eq. (12) in Sobel and Maloney (2013) or Eq. (4a) in Adames and Kim (2016)]. $\Gamma_{\mathrm{v,r}}$, which is set to be a constant, corresponds to the GMS[10] in the theoretical work. We show below that Eq. 4.26 is enough to represent the GMS plane behavior shown in Figs. 4.6 and 4.7.

Since this study investigated the MSE budget in Eulerian columns at fixed locations, we can set $x = 0$ in Eq. 4.25 without loss of generality. Because only the real component of Eq. 4.26 makes physical sense, plugging Eq. 4.25 into Eq. 4.26 and extracting the real component yields

$$\langle \omega \partial h/\partial p \rangle' = \hat{P} \exp\left(-\Gamma_{\mathrm{eff,r}} t\right) \left[\Gamma_{\mathrm{v,r}} \cos\left(\Gamma_{\mathrm{eff,i}} t\right) + \Gamma_{\mathrm{v,i}} \sin\left(\Gamma_{\mathrm{eff,i}} t\right) \right], \tag{4.27}$$

where we set $\sigma_r = -\Gamma_{\mathrm{eff,r}}$ and $\sigma_i = -\Gamma_{\mathrm{eff,i}}$, and we assume $\hat{P}$ is a real number. Similarly, the real components of P' and $\partial P'/\partial t$ are expressed as

$$P' = \hat{P} \exp\left(-\Gamma_{\mathrm{eff,r}} t\right) \cos\left(\Gamma_{\mathrm{eff,i}} t\right), \tag{4.28}$$

[10]Precisely speaking, $\Gamma_{\mathrm{v,r}}$ corresponds to $\langle \omega \partial h/\partial p \rangle / P$. But this can be easily converted into $\langle \omega \partial h/\partial p \rangle / \nabla \cdot \langle s\mathbf{v} \rangle$ using the DSE budget equation with the WTG.

$$\frac{\partial P'}{\partial t} = \hat{P}\exp\left(-\Gamma_{\mathbf{eff,r}}t\right)\left[-\Gamma_{\mathbf{eff,r}}\cos\left(\Gamma_{\mathbf{eff,i}}t\right) - \Gamma_{\mathbf{eff,i}}\sin\left(\Gamma_{\mathbf{eff,i}}t\right)\right]. \tag{4.29}$$

Now we want to estimate the values of $\Gamma_{\mathbf{v,r}}$ and $\Gamma_{\mathbf{v,i}}$ using observations. First, in a long time-series, we can approximate $\Gamma_{\mathbf{eff,r}} \simeq 0$ otherwise the precipitation grows infinitely or converges to zero. Therefore, we can write Eqs. 4.27, 4.28, and 4.29 as

$$\langle\omega\partial h/\partial p\rangle' \simeq \hat{P}\left[\Gamma_{\mathbf{v,r}}\cos\left(\Gamma_{\mathbf{eff,i}}t\right) + \Gamma_{\mathbf{v,i}}\sin\left(\Gamma_{\mathbf{eff,i}}t\right)\right], \tag{4.30}$$

$$P' \simeq \hat{P}\cos\left(\Gamma_{\mathbf{eff,i}}t\right), \tag{4.31}$$

$$\frac{\partial P'}{\partial t} \simeq -\hat{P}\Gamma_{\mathbf{eff,i}}\sin\left(\Gamma_{\mathbf{eff,i}}t\right). \tag{4.32}$$

For estimating $\Gamma_{\mathbf{v,r}}$, we want to multiply Eq. 4.30 with $\cos\left(\Gamma_{\mathbf{eff,i}}t\right)$ and take an integration with respect to time from 0 to 2π. In such a way, $\Gamma_{\mathbf{v,r}}$ can be estimated in observational data as

$$\Gamma_{\mathbf{v,r}} \simeq \frac{\overline{\langle\omega\partial h/\partial p\rangle' * P'}}{\overline{P'^2}}, \tag{4.33}$$

where the bar, which represents a time average, can be considered as an integration from 0 to 2π if a time-series is long enough. This is similar to the characteristic GMS defined by Eq. 4.21, indicating the theoretical GMS, which is relevant to the instability, can be estimated as the characteristic GMS. Similarly, we can estimate $\Gamma_{\mathbf{v,i}}$ as

$$\Gamma_{\mathbf{v,i}} \simeq -\Gamma_{\mathbf{eff,i}} * \frac{\overline{\langle\omega\partial h/\partial p\rangle' * \partial P'/\partial t}}{\overline{(\partial P'/\partial t)^2}}. \tag{4.34}$$

Similar (but not the same) methods were used by Andersen and Kuang (2011) to compute the contributions of each MSE budget term to the stabilization and to the

propagation of the MJO-like variability.

For a demonstration, we set the frequency to be $\Gamma_{\mathrm{eff,i}} = 2\pi/40$ (day^{-1}). And using the TOGA COARE data, we estimated $\Gamma_{\mathrm{v,r}}$ to be ~ 0.25 and $\Gamma_{\mathrm{v,i}}$ to be ~ 0.05. But for the illustrative purpose, we used $\Gamma_{\mathrm{v,i}} = 0.15$ instead of 0.05. Using these values of the parameters, the temporal evolutions of Eqs. 4.27 and 4.28 are plotted in Fig. 4.14. Figure 4.14a illustrates one cycle (from day 0 to day 40) of $\langle \omega \partial h/\partial p \rangle'$ versus P' in the neutral condition (i.e., the effective GMS is zero or $\Gamma_{\mathrm{eff,r}} = 0$). The cycle starts from the red dot, goes around counter-clockwise, and terminates at the blue dot. This behavior is similar to that shown in the GMS plane[11] in Fig. 4.7, indicating that the temporal variability of the GMS shown in this study is not necessarily relevant to the instability of the moisture mode; the orbiting pattern in the GMS plane can happen even in the neutral condition where $\Gamma_{\mathrm{eff,r}} = 0$ if the advection terms contribute to the propagation (i.e., $\Gamma_{\mathrm{v,i}} \neq 0$).

This figure clarifies why the GMS is a vexing quantity. In this figure, we can find out two distinct GMSs:

$$\text{GMS (theoretical)} \sim \Gamma_{\mathrm{v,r}}, \tag{4.35}$$

$$\text{GMS (diagnostic)} \sim \Gamma_{\mathrm{v,r}} + \Gamma_{\mathrm{v,i}} \tan\left(\Gamma_{\mathrm{eff,i}} t\right), \tag{4.36}$$

where the former represents the slope of the major axis of the elliptic trajectory, and the latter was computed by simply dividing Eq. 4.27 by Eq. 4.28. The distinction between these two GMSs is the same as the distinction between the time-dependent

[11] The x-axis in Fig. 4.14 is P that is similar to $\nabla \cdot \langle s\mathbf{v} \rangle$, thus Fig. 4.14 is almost the same as the GMS plane when we ignore the horizontal MSE advection.

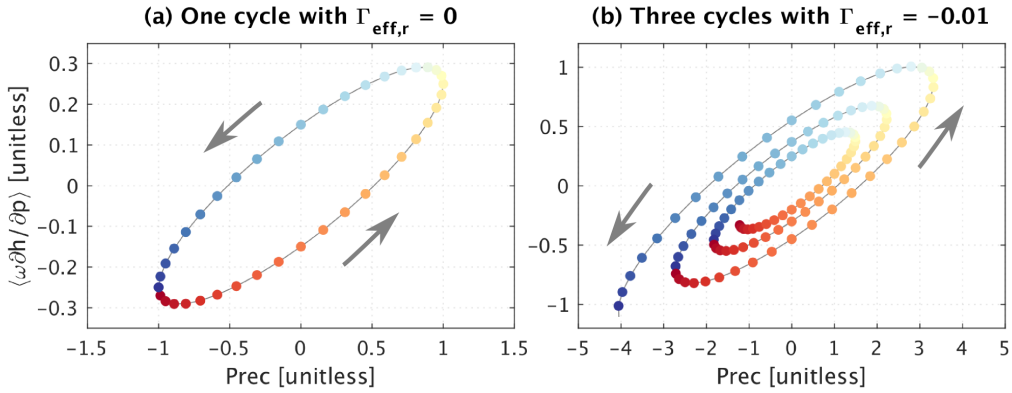

Figure 4.14: (a) one cycle [the start (red dot) to the end (blue dot)] of $\langle \omega \partial h/\partial p \rangle'$ and P' expressed as Eqs. 4.27 and 4.28. For an illustrative purpose, plotted are from day 20 to day 60. $\Gamma_{v,r}$ and $\Gamma_{v,i}$ were set to be 0.25 and 0.15, respectively, with $\Gamma_{eff,r} = 0$. (b) Three cycles (from day 20 to day 140) with $\Gamma_{eff,r} = -0.01$.

and quasi-time-independent GMSs discussed in section 4.5. When we compute the GMS as a time-dependent quantity using time-series, it corresponds to Eq. 4.36. This diagnostic GMS can easily become negative, but that negative GMS is not relevant to the stability of the moisture mode; only $\Gamma_{v,r}$ is associated with the stability (or $\Gamma_{eff,r}$).

Figures 4.14b illustrates the GMS plane behavior in an unstable condition where the effective GMS is set to be slightly negative ($\Gamma_{eff,r} = -0.01$). This condition occurs when the radiative feedback effect exceeds the (theoretical) GMS. There is a growing spiral due to an exponentially amplifying oscillation, which is a characteristic of destabilized linear waves. In the real world, however, this kind of growing spiral does not happen because nonlinear effects generally keep a disturbance from growing infinitely.

The distinction between the theoretical and diagnostic GMSs defined in Eqs. 4.35

and 4.36 becomes crucial when the size of an observational domain is smaller than that of a MJO envelope. In such a case, the contribution of the MSE advection to the propagation (i.e., nonzero $\Gamma_{v,i}$) easily makes the diagnostic GMS negative via Eq. 4.36. But that negative GMS must not be confused with the negative theoretical GMS for the destabilization. This fact points out general misconceptions in the past MSE budget studies which, implicitly or explicitly, tried to associate the temporal variability of the MSE budgets with the destabilization of the moisture mode. If the spatial domains of those analyses are smaller than the size of the MJO, for the reason discussed above, the values of the estimated GMS do not necessarily represent the "gross stability" of the system.

There is a speculation that the values of $\Gamma_{v,r}$ vary over time, which turn on and off the moisture mode (e.g., Ling et al., 2013). We want to emphasize that the discussion above does not deny this speculation. Our main point is that, for investigating such GMS variability, the choice of the domain size and how to compute the values of it are crucial. If we use a wrong domain size and computation method, the GMS might not provide us with any meaningful information about the MJO dynamics. Regarding the domain size, we need to integrate large areas, at least, over the whole tropical Indian Ocean as Ling et al. (2013) did in their analyses, and the sizes of the TOGA COARE and DYNAMO regions are not large enough to examine the instability of the MJO.

4.6.2 Terminology of GMS

The diagnostic, highly time-dependent GMS (Eq. 4.36) is distinct from the theoretical, quasi-time-independent GMS (Eq. 4.35). In the same sense, the drying efficiency used in this study is not the same as the effective GMS in the past theoretical literature. This distinction cannot be emphasized too much because the terminology "GMS" is now used to mean both the diagnostic and theoretical ones. Since this terminology is so widely accepted, it is not a good idea to coin a new terminology for the diagnostic, time-dependent GMS. However, it is crucial to keep in mind that those two must be interpreted differently: The quasi-time-independent GMS represents the stability of the background condition, thus is relevant to the moisture mode. On the other hand, the highly time-dependent GMS does not represent the background stability, but it represents "advective drying efficiency" via convectively induced large-scale circulations, which expresses local favorability for convection due to large-scale circulations.

4.7 Summary

We investigated the GMS and its related quantities utilizing satellite-based products over the tropical ocean. In the data sets used, we found the diabatic source ($D \equiv \langle Q_R \rangle + S$) can be expressed as a linear function of the divergence of column MSE ($+\nabla \cdot \langle s\mathbf{v} \rangle$) with a slope of γ. This linear relationship, together with a positive correlation between precipitation and precipitable water, indicates that when the GMS is less/greater than the critical constant γ the convection amplifies/decays.

This means that, if the value of γ is given, the GMS tells us whether the convection will amplify or decay. But this statement is only true when the denominator of the GMS, $\nabla \cdot \langle s\mathbf{v} \rangle$, is positive. We generalized this condition by introducing the "GMS plane" analysis.

We refer to the $\nabla \cdot \langle h\mathbf{v} \rangle$-vs-$\nabla \cdot \langle s\mathbf{v} \rangle$ plane as the GMS plane. In this plane, we can easily determine whether convection is in the amplifying phase or in the decaying phase. First, we draw a critical line going through the origin whose slope is the critical GMS γ. Then, if a data point lies below/above the critical line, the convection is most likely in the amplifying/decaying phase. Furthermore, the GMS plane behaves like a phase plane in which each convective life-cycle seems like an orbiting fluctuation around the critical line. This GMS plane behavior indicates that the value of the GMS (or phase position in the GMS plane) qualitatively predicts the subsequent convective evolution. This predictability is rooted in the fact that the GMS (or the pair of $\nabla \cdot \langle h\mathbf{v} \rangle$ and $\nabla \cdot \langle s\mathbf{v} \rangle$) possesses similar information to that deduced from the pair of P and $\partial P/\partial t$. Therefore, we can say that the GMS is an alternative representation of a convective phase, expressed in terms of the quantities relevant to convectively induced large-scale circulations.

We also investigated a quasi-time-independent aspect of the GMS. We plotted the geographic variability of the characteristic GMSs defined by Eqs. 4.19–4.22. All the characteristic GMSs, except for the climatological GMS $\overline{\Gamma}$, exhibit robust and consistent geographic patterns; the values of the characteristic GMSs are consistently higher in the Indian and western Pacific Oceans than in the central-eastern Pacific and Atlantic Oceans. These geographic patterns might be intertwined with those

of vertical-velocity-profile shapes. We found that the climatological GMS $\overline{\Gamma}$ is so sensitive to data errors that it should not be used as a diagnostic tool for data involving non-negligible errors.

In section 4.6, we demonstrated the behaviors of the GMS plane with a simple linear model with a fixed GMS. This model shows that the GMS plane behaviors presented in this study can be qualitatively reproduced even in a linear model with a constant GMS if we include a propagation component in the model. Furthermore, we pointed out that, in that linear model, it is possible to define two distinct GMSs: diagnostic, highly time-dependent GMS and theoretical, quasi-time-independent GMS. These two GMSs have distinct interpretations and must not be confused with each other. The theoretical GMS represents the background stability, thus is relevant to the moisture-mode theory. In contrast, the diagnostic, time-dependent GMS represents an "advective drying efficiency" via convectively induced large-scale circulations, which expresses local favorability for convection, and does not represent the stability of the linear moisture mode. This fact suggests that attempts to associate MSE budget time-series with the moisture-mode stability may not be meaningful if the choice of observational domain sizes and the means of GMS computations are not appropriate.

Chapter 5

Summary and discussion

In this dissertation work, we analyzed the MSE budgets and its relevant quantities using field campaign and satellite-based data sets. Since tropical convection is tightly related to atmospheric moisture, and temperature anomalies are negligible in the tropics due to weak Coriolis constrains, the MSE budget equation has been widely used for investigating the mechanism of tropical convective disturbances. In this study, we proposed a few novel diagnostic applications of the MSE budgets and a conceptual quantity called the gross moist stability (GMS).

In chapter 2, we examined vertically integrated MSE budgets on different time scales, and showed that they behave in significantly different ways among the different time scales. Our analyses highlight the importance of the investigation of the MSE budgets on different time scales. We believe that this type of analysis will facilitate a better understanding of the mechanism of an interaction between atmospheric moisture and tropical convection.

In the tropics, how moisture fields modulate the dynamics is an important question. However, there has been no consensus about the answer for this question. For instance, Yasunaga and Mapes (2012) analyzed the relationship between precipitation and precipitable water using a composite analysis, and found that it varies significantly among the different types of convectively coupled equatorial waves

(CCEWs). They showed that the coherence between precipitation and precipitable water is high in a "rotational" type of CCEWs such as equatorial Rossby waves and mixied Rossby-gravity waves whereas it is relatively low in a "divergent" type of CCEWs such as equatorial Kelvin waves and westward inertia-gravity waves. By contrast, Peters and Bretherton (2006) examined equatorial Kelvin waves produced by a cloud resolving model, and found that "moisture is a dominant regulator of convection" in the simulated Kelvin waves. Those two studies seem to contradict each other. Therefore, careful diagnoses of precipitable water in different types of convective disturbances are of great importance. And as we discussed again and again in this dissertation work, the column MSE budgets are useful for that purpose. We believe that the analyses presented in chapter 2 can be extended to answer the question about the relationship between precipitation and precipitable water among the different types of CCEWs. We can apply, as in chapter 2, a lag-regression analysis to different types of CCEWs so as to investigate how the MSE budgets behave in those waves.

We also found an interesting pattern in vertical velocity profiles with the same lag-regression analysis; as the time scale gets longer, the shape of vertical velocity profiles becomes closer to a first baroclinic structure. This result suggests that the importance of a second baroclinic structure differs significantly among time-scales or frequencies. It would be interesting to repeat this analysis using another data sets such as the ERA-Interim in order to obtain more general conclusions about the vertical velocity profiles.

In chapter 3, we investigated the convective amplification/decay mechanisms

by examining the GMS and its relevant quantities in the TOGA COARE data set. We coined two quantities, the critical GMS, and the drying efficiency. The critical GMS is a ratio of the diabatic source to the intensity of convection, and the drying efficiency, defined as GMS minus critical GMS, represents the loss of water vapor due to convection. We found that the convection amplifies/decays when the drying efficiency is negative/positive. Negative drying efficiencies are associated with bottom-heavy vertical velocity profiles, which import MSE via low-level convergence, leading to further enhancement of the convection. As the convection develops, the vertical velocity profile gradually becomes top heavier, starting export of MSE from the upper troposphere (which is associated with a positive drying efficiency), which leads to dissipation of the convection. Throughout the convective life-cycle, the critical GMS stays relatively constant with a positive value. This indicates that the diabatic source term always tends to destabilize the convective system by supplying the MSE sources in a positive feedback loop.

We also defined the quasi-time-independent GMS called the characteristic GMS, and discussed the physical interpretations of it. The characteristic GMS can be interpreted (1) as a threshold value of the GMS between the amplifying and decaying phases, and (2) as a combination of the radiative-convective feedback constant and the evaporation-convection feedback constant.

In chapter 4, we extended the ideas presented in chapter 3 using satellite-based data sets. In these data sets, we found the diabatic source can be expressed as a linear function of the intensity of convection. Utilizing this linear trend, we proposed a novel diagnostic framework which we refer to as the “GMS plane”.

We call the $\nabla \cdot \langle h\mathbf{v} \rangle$-vs-$\nabla \cdot \langle s\mathbf{v} \rangle$ plane as the GMS plane. In this plane, one can easily determine if the convection is in the amplifying phase or in the decaying phase. In this plane, we first draw a critical line through the origin whose slope is a constant which represents a positive feedback between the diabatic source and convection. And if a data point is located below/above this critical line, the convection is most likely in the amplifying/decaying phase. We also found that the GMS plane is a phase plane in which each convective life cycle goes around the critical line counterclockwise. This phase plane behavior indicates that the value of the GMS predicts the subsequent convective evolution. And the phase plane behavior can be expressed graphically by plotting the arc-tangent of the GMS.

We also investigated the geographic variability of the characteristic GMS, which exhibits a distinct pattern; the values of the characteristic GMS are slightly higher in the Indian and western Pacific Oceans than the central-eastern Pacific and Atlantic Oceans. This distribution is, to some extent, consistent with the geographic variability of vertical velocity profiles.

Finally, we demonstrated the behaviors of the GMS plane with an empirical linear model, and pointed out a crucial distinction between theoretical, quasi-time-independent GMS and diagnostic, highly time-dependent GMS. The former is relevant to the moisture mode stability, but the latter is not. Our demonstration pointed out general misconceptions in the past MSE budget studies which, implicitly or explicitly, attempted to associate the temporal variability of MSE budgets with the stability of the moisture mode.

References

Adames, Á. F. and D. Kim, 2016: The MJO as a Dispersive, Convectively Coupled Moisture Wave: Theory and Observations. *J. Atmos. Sci.*, **73**, 913–941, doi:10.1175/JAS-D-15-0170.1.

Andersen, J. A. and Z. Kuang, 2011: Moist static energy budget of MJO-like disturbances in the atmosphere of a zonally symmetric aquaplanet. *J. Climate*, **25**, 2782–2804, doi:10.1175/JCLI-D-11-00168.1.

Araligidad, N. M. and E. D. Maloney, 2008: Wind-driven latent heat flux and the intraseasonal oscillation. *Geophys. Res. Lett.*, **35**, L04 815, doi:10.1029/2007GL032746.

Back, L. E. and C. S. Bretherton, 2005: The relationship between wind speed and precipitation in the pacific ITCZ. *J. Climate*, **18**, 4317–4328, doi:10.1175/JCLI3519.1.

Back, L. E. and C. S. Bretherton, 2006: Geographic variability in the export of moist static energy and vertical motion profiles in the tropical Pacific. *Geophys. Res. Lett.*, **33**, L17 810, doi:10.1029/2006GL026672.

Back, L. E. and C. S. Bretherton, 2009a: On the Relationship between SST Gradients, Boundary Layer Winds, and Convergence over the Tropical Oceans. *J. Climate*, **22**, 4182–4196, doi:10.1175/2009JCLI2392.1.

Back, L. E. and C. S. Bretherton, 2009b: A Simple Model of Climatological Rainfall and Vertical Motion Patterns over the Tropical Oceans. *J. Climate*, **22**, 6477–6497, doi:10.1175/2009JCLI2393.1.

Benedict, J. J., E. D. Maloney, A. H. Sobel, D. M. Frierson, and L. J. Donner, 2013: Tropical intraseasonal variability in version 3 of the GFDL atmosphere model. *J. Climate*, **26**, 426–449, doi:10.1175/JCLI-D-12-00103.1.

Benedict, J. J., E. D. Maloney, A. H. Sobel, and D. M. W. Frierson, 2014: Gross moist stability and MJO simulation skill in three full-physics GCMs. *J. Atmos. Sci.*, **71**, 3327–3349, doi:10.1175/JAS-D-13-0240.1.

Benedict, J. J. and D. A. Randall, 2007: Observed characteristics of the MJO relative to maximum rainfall. *J. Atmos. Sci.*, **64**, 2332–2354, doi:10.1175/JAS3968.1.

Betts, A. K., 1986: A new convective adjustment scheme. Part I: Observational and theoretical basis. *Quart. J. Roy. Meteor. Soc.*, **112**, 677–691, doi:10.1002/qj.49711247307.

Betts, A. K. and M. J. Miller, 1986: A new convective adjustment scheme. Part II: Single column tests using GATE wave, BOMEX, ATEX and arctic air-mass data sets. *Quart. J. Roy. Meteor. Soc.*, **112**, 693–709, doi:10.1002/qj.49711247308.

Bretherton, C. S., P. N. Blossey, and M. Khairoutdinov, 2005: An Energy-Balance Analysis of Deep Convective Self-Aggregation above Uniform SST. *J. Atmos. Sci.*, **62**, 4273–4292, doi:10.1175/JAS3614.1.

Bretherton, C. S. and M. F. Khairoutdinov, 2015: Convective self-aggregation feedbacks in near-global cloud-resolving simulations of an aquaplanet. *J. Adv. Model. Earth Syst.*, **7**, 1765–1787, doi:10.1002/2015MS000499.

Bretherton, C. S., M. E. Peters, and L. E. Back, 2004: Relationships between water vapor path and precipitation over the tropical oceans. *J. Climate*, **17**, 1517–1528, doi:10.1175/1520-0442(2004)017<1517:RBWVPA>2.0.CO;2.

Bretherton, C. S. and P. K. Smolarkiewicz, 1989: Gravity waves, compensating subsidence and detrainment around cumulus clouds. *J. Atmos. Sci.*, **46**, 740–759, doi:10.1175/1520-0469(1989)046<0740:GWCSAD>2.0.CO;2.

Bretherton, C. S. and A. H. Sobel, 2002: A Simple Model of a Convectively Coupled Walker Circulation Using the Weak Temperature Gradient Approximation. *J. Climate*, **15**, 2907–2920, doi:10.1175/1520-0442(2002)015<2907:ASMOAC>2.0.CO;2.

Bretherton, C. S., M. Widmann, V. P. Dymnikov, J. M. Wallace, and I. Bladé, 1999: The effective number of spatial degrees of freedom of a time-varying field. *J. Climate*, **12**, 1990–2009, doi:10.1175/1520-0442(1999)012<1990:TENOSD>2.0.CO;2.

Brown, R. G. and C. S. Bretherton, 1997: A Test of the Strict Quasi-Equilibrium Theory on Long Time and Space Scales. *J. Atmos. Sci.*, **54**, 624–638, doi:10.1175/1520-0469(1997)054<0624:ATOTSQ>2.0.CO;2.

Charney, J. G., 1963: A note on large-scale motions in the tropics. *J. Atmos. Sci.*, **20**, 607–609, doi:10.1175/1520-0469(1963)020<0607:ANOLSM>2.0.CO;2.

Charney, J. G., 1969: A further note on large-scale motions in the tropics. *J. Atmos. Sci.*, **26**, 182–185, doi:10.1175/1520-0469(1969)026<0182:AFNOLS>2.0.CO;2.

Cho, H. and D. Pendlebury, 1997: Wave CISK of equatorial waves and the vertical distribution of cumulus heating. *J. Atmos. Sci.*, **54**, 2429–2440, doi:10.1175/1520-0469(1997)054<2429:WCOEWA>2.0.CO;2.

Cho, H.-R. and M. A. Jenkins, 1987: The Thermal Structure of Tropical Easterly Waves. *J. Atmos. Sci.*, **44**, 2531–2539, doi:10.1175/1520-0469(1987)044<2531:TTSOTE>2.0.CO;2.

Chou, C., T.-C. Wu, and P.-H. Tan, 2013: Changes in gross moist stability in the tropics under global warming. *Clim Dyn*, **41**, 2481–2496, doi:10.1007/s00382-013-1703-2.

Ciesielski, P. E., R. H. Johnson, K. Yoneyama, and R. K. Taft, 2014a: Mitigation of Sri Lanka Island Effects in Colombo Sounding Data and Its Impact on DYNAMO Analyses. *J. Meteor. Soc. Japan*, **92**, 385–405, doi:10.2151/jmsj.2014-407.

Ciesielski, P. E., et al., 2014b: Quality-Controlled Upper-Air Sounding Dataset for DYNAMO/CINDY/AMIE: Development and Corrections. *Journal of Atmospheric and Oceanic Technology*, **31**, 741–764, doi:10.1175/JTECH-D-13-00165.1.

Curry, J. A., et al., 2004: Seaflux. *Bull. Amer. Meteor. Soc.*, **85**, 409–424, doi:10.1175/BAMS-85-3-409.

Dee, D. P., et al., 2011: The ERA-Interim reanalysis: configuration and performance of the data assimilation system. *Quart. J. Roy. Meteor. Soc.*, **137**, 553–597, doi:10.1002/qj.828.

Dellaripa, E. M. R. and E. D. Maloney, 2015: Analysis of MJO Wind-Flux Feedbacks in the Indian Ocean Using RAMA Buoy Observations. *J. Meteor. Soc. Japan*, **93A**, 1–20, doi:10.2151/jmsj.2015-021.

Duchon, C. E., 1979: Lanczos filtering in one and two dimensions. *J. Appl. Meteor.*, **18**, 1016–1022, doi:10.1175/1520-0450(1979)018<1016:LFIOAT>2.0.CO;2.

Emanuel, K. A., J. D. Neelin, and C. S. Bretherton, 1994: On large-scale circulations in convecting atmospheres. *Quart. J. Roy. Meteor. Soc.*, **120**, 1111–1143, doi:10.1002/qj.49712051902.

Frierson, D. M. W., 2007: Convectively coupled Kelvin waves in an idealized moist general circulation model. *J. Atmos. Sci.*, **64**, 2076–2090, doi:10.1175/JAS3945.1.

Frierson, D. M. W., D. Kim, I.-S. Kang, M.-I. Lee, and J. Lin, 2011: Structure of AGCM-Simulated Convectively Coupled Kelvin Waves and Sensitivity to Convective Parameterization. *J. Atmos. Sci.*, **68**, 26–45, doi:10.1175/2010JAS3356.1.

Fu, X. and B. Wang, 2009: Critical roles of the stratiform rainfall in sustaining the Madden-Julian Oscillation: GCM experiments*. *J. Climate*, **22**, 3939–3959, doi:10.1175/2009JCLI2610.1.

Fuchs, Ž., S. Gjorgjievska, and D. J. Raymond, 2012: Effects of Varying the Shape of the Convective Heating Profile on Convectively Coupled Gravity Waves and Moisture Modes. *J. Atmos. Sci.*, **69**, 2505–2519, doi:10.1175/JAS-D-11-0308.1.

Fuchs, Ž. and D. J. Raymond, 2002: Large-Scale Modes of a Nonrotating Atmosphere with Water Vapor and Cloud-Radiation Feedbacks. *J. Atmos. Sci.*, **59**, 1669–1679, doi:10.1175/1520-0469(2002)059<1669:LSMOAN>2.0.CO;2.

Fuchs, Ž. and D. J. Raymond, 2005: Large-Scale Modes in a Rotating Atmosphere with Radiative-Convective Instability and WISHE. *J. Atmos. Sci.*, **62**, 4084–4094, doi:10.1175/JAS3582.1.

Fuchs, Ž. and D. J. Raymond, 2007: A simple, vertically resolved model of tropical disturbances with a humidity closure. *Tellus A*, **59**, 344–354, doi:10.1111/j.1600-0870.2007.00230.x.

Haertel, P. T. and G. N. Kiladis, 2004: Dynamics of 2-day equatorial waves. *J. Atmos. Sci.*, **61**, 2707–2721, doi:10.1175/JAS3352.1.

Haertel, P. T., G. N. Kiladis, A. Denno, and T. M. Rickenbach, 2008: Vertical-mode decompositions of 2-day waves and the Madden-Julian Oscillation. *J. Atmos. Sci.*, **65**, 813–833, doi:10.1175/2007JAS2314.1.

Hannah, W. M. and E. D. Maloney, 2011: The role of moisture-convection feedbacks in simulating the Madden-Julian Oscillation. *J. Climate*, **24**, 2754–2770, doi:10.1175/2011JCLI3803.1.

Hannah, W. M. and E. D. Maloney, 2014: The moist static energy budget in NCAR CAM5 hindcasts during DYNAMO. *J. Adv. Model. Earth Syst.*, **6**, 420–440, doi:10.1002/2013MS000272.

Hannah, W. M., B. E. Mapes, and G. S. Elsaesser, 2016: A Lagrangian View of Moisture Dynamics during DYNAMO. *J. Atmos. Sci.*, **73**, 1967–1985, doi:10.1175/JAS-D-15-0243.1.

Herman, M. J., Ž. Fuchs, D. J. Raymond, and P. Bechtold, 2016: Convectively Coupled Kelvin Waves: From Linear Theory to Global Models. *J. Atmos. Sci.*, **73**, 407–428, doi:10.1175/JAS-D-15-0153.1.

Huffman, G. J., R. F. Adler, D. T. Bolvin, and E. J. Nelkin, 2010: The TRMM Multi-Satellite Precipitation Analysis (TMPA). *Satellite Rainfall Applications for Surface Hydrology*, M. Gebremichael and F. Hossain, Eds., Springer Netherlands, 3–22.

Huffman, G. J., et al., 2007: The TRMM Multisatellite Precipitation Analysis (TMPA): Quasi-Global, Multiyear, Combined-Sensor Precipitation Estimates at Fine Scales. *J. Hydrometeor.*, **8**, 38–55, doi:10.1175/JHM560.1.

Inoue, K. and L. Back, 2015a: Column-Integrated Moist Static Energy Budget Analysis on Various Time Scales during TOGA COARE. *J. Atmos. Sci.*, **72**, 1856–1871, doi:10.1175/JAS-D-14-0249.1.

Inoue, K. and L. E. Back, 2015b: Gross Moist Stability Assessment during TOGA COARE: Various Interpretations of Gross Moist Stability. *J. Atmos. Sci.*, **72**, 4148–4166, doi:10.1175/JAS-D-15-0092.1.

Jenkins, M. A. and H.-R. Cho, 1991: An Observational Study of the First-Order Vorticity Dynamics in a Tropical Easterly Wave. *J. Atmos. Sci.*, **48**, 965–975, doi:10.1175/1520-0469(1991)048<0965:AOSOTF>2.0.CO;2.

Johnson, R. H. and P. E. Ciesielski, 2000: Rainfall and Radiative Heating Rates from TOGA COARE Atmospheric Budgets. *J. Atmos. Sci.*, **57**, 1497–1514, doi:10.1175/1520-0469(2000)057<1497:RARHRF>2.0.CO;2.

Johnson, R. H. and P. E. Ciesielski, 2013: Structure and Properties of Madden-Julian Oscillations Deduced from DYNAMO Sounding Arrays. *J. Atmos. Sci.*, **70**, 3157–3179, doi:10.1175/JAS-D-13-065.1.

Johnson, R. H., P. E. Ciesielski, and K. A. Hart, 1996: Tropical inversions near the 0C level. *J. Atmos. Sci.*, **53**, 1838–1855, doi:10.1175/1520-0469(1996)053<1838:TINTL>2.0.CO;2.

Johnson, R. H., P. E. Ciesielski, J. H. Ruppert, and M. Katsumata, 2015: Sounding-Based Thermodynamic Budgets for DYNAMO. *J. Atmos. Sci.*, **72**, 598–622, doi:10.1175/JAS-D-14-0202.1.

Johnson, R. H., T. M. Rickenbach, S. A. Rutledge, P. E. Ciesielski, and W. H. Schubert, 1999: Trimodal characteristics of tropical convection. *J. Climate*, **12**, 2397–2418, doi:10.1175/1520-0442(1999)012<2397:TCOTC>2.0.CO;2.

Khouider, B. and A. J. Majda, 2006: A Simple Multicloud Parameterization for Convectively Coupled Tropical Waves. Part I: Linear Analysis. *J. Atmos. Sci.*, **63**, 1308–1323, doi:10.1175/JAS3677.1.

Kikuchi, K. and Y. N. Takayabu, 2004: The development of organized convection associated with the MJO during TOGA COARE IOP: Trimodal characteristics. *Geophys. Res. Lett.*, **31**, L10 101, doi:10.1029/2004GL019601.

Kiladis, G. N., K. H. Straub, and P. T. Haertel, 2005: Zonal and vertical structure of the Madden-Julian Oscillation. *J. Atmos. Sci.*, **62**, 2790–2809, doi:10.1175/JAS3520.1.

Kiladis, G. N. and K. M. Weickmann, 1992: Circulation anomalies associated with tropical convection during northern winter. *Mon. Wea. Rev.*, **120**, 1900–1923, doi:10.1175/1520-0493(1992)120<1900:CAAWTC>2.0.CO;2.

Kiladis, G. N., M. C. Wheeler, P. T. Haertel, K. H. Straub, and P. E. Roundy, 2009: Convectively coupled equatorial waves. *Rev. Geophys.*, **47**, RG2003, doi:10.1029/2008RG000266.

Kim, D., J.-S. Kug, and A. H. Sobel, 2014: Propagating versus nonpropagating Madden-Julian oscillation events. *J. Climate*, **27**, 111–125, doi:10.1175/JCLI-D-13-00084.1.

Kim, D., et al., 2009: Application of MJO simulation diagnostics to climate models. *J. Climate*, **22**, 6413–6436, doi:10.1175/2009JCLI3063.1.

Kuang, Z., 2008a: Modeling the Interaction between Cumulus Convection and Linear Gravity Waves Using a Limited-Domain Cloud System-Resolving Model. *J. Atmos. Sci.*, **65**, 576–591, doi:10.1175/2007JAS2399.1.

Kuang, Z., 2008b: A moisture-stratiform instability for convectively coupled waves. *J. Atmos. Sci.*, **65**, 834–854, doi:10.1175/2007JAS2444.1.

Kuang, Z., 2010: The wavelength dependence of the gross moist stability and the scale selection in the instability of column-integrated moist static energy. *J. Atmos. Sci.*, **68**, 61–74, doi:10.1175/2010JAS3591.1.

Kumar, B. P., J. Vialard, M. Lengaigne, V. S. N. Murty, and M. J. McPhaden, 2011: TropFlux: air-sea fluxes for the global tropical oceans-description and evaluation. *Climate Dyn.*, **38**, 1521–1543, doi:10.1007/s00382-011-1115-0.

Lappen, C.-L. and C. Schumacher, 2012: Heating in the tropical atmosphere: what level of detail is critical for accurate MJO simulations in GCMs? *Clim Dyn*, **39**, 2547–2568, doi:10.1007/s00382-012-1327-y.

Lappen, C.-L. and C. Schumacher, 2014: The role of tilted heating in the evolution of the MJO. *J. Geophys. Res. Atmos.*, **119**, 2966–2989, doi:10.1002/2013JD020638.

L'Ecuyer, T. S. and G. L. Stephens, 2003: The Tropical Oceanic Energy Budget from the TRMM Perspective. Part I: Algorithm and Uncertainties. *J. Climate*, **16**, 1967–1985, doi:10.1175/1520-0442(2003)016<1967:TTOEBF>2.0.CO;2.

L'Ecuyer, T. S. and G. L. Stephens, 2007: The Tropical Atmospheric Energy Budget from the TRMM Perspective. Part II: Evaluating GCM Representations of the Sensitivity of Regional Energy and Water Cycles to the 1998-99 ENSO Cycle. *J. Climate*, **20**, 4548–4571, doi:10.1175/JCLI4207.1.

Lin, J., B. Mapes, M. Zhang, and M. Newman, 2004: Stratiform precipitation, vertical heating profiles, and the Madden-Julian Oscillation. *J. Atmos. Sci.*, **61**, 296–309, doi:10.1175/1520-0469(2004)061<0296:SPVHPA>2.0.CO;2.

Lin, J.-L., 2007: The Double-ITCZ Problem in IPCC AR4 Coupled GCMs: Ocean-Atmosphere Feedback Analysis. *J. Climate*, **20**, 4497–4525, doi:10.1175/JCLI4272.1.

Lin, J.-L. and B. E. Mapes, 2004: Radiation Budget of the Tropical Intraseasonal Oscillation. *J. Atmos. Sci.*, **61**, 2050–2062, doi:10.1175/1520-0469(2004)061<2050:RBOTTI>2.0.CO;2.

Lin, J.-L., et al., 2006: Tropical intraseasonal variability in 14 IPCC AR4 climate models. part i: Convective signals. *J. Climate*, **19**, 2665–2690, doi:10.1175/JCLI3735.1.

Lin, X. and R. H. Johnson, 1996: Kinematic and thermodynamic characteristics of the flow over the western pacific warm pool during TOGA COARE. *J. Atmos. Sci.*, **53**, 695–715, doi:10.1175/1520-0469(1996)053<0695:KATCOT>2.0.CO;2.

Ling, J., C. Zhang, and P. Bechtold, 2013: Large-Scale Distinctions between MJO and Non-MJO Convective Initiation over the Tropical Indian Ocean. *J. Atmos. Sci.*, **70**, 2696–2712, doi:10.1175/JAS-D-13-029.1.

Madden, R. A. and P. R. Julian, 1971: Detection of a 40–50 Day Oscillation in the Zonal Wind in the Tropical Pacific. *J. Atmos. Sci.*, **28**, 702–708, doi:10.1175/1520-0469(1971)028<0702:DOADOI>2.0.CO;2.

Madden, R. A. and P. R. Julian, 1972: Description of Global-Scale Circulation Cells in the Tropics with a 40–50 Day Period. *J. Atmos. Sci.*, **29**, 1109–1123, doi:10.1175/1520-0469(1972)029<1109:DOGSCC>2.0.CO;2.

Madden, R. A. and P. R. Julian, 1994: Observations of the 40–50-Day Tropical OscillationâĽ”A Review. *Mon. Wea. Rev.*, **122**, 814–837, doi:10.1175/1520-0493(1994)122<0814:OOTDTO>2.0.CO;2.

Maloney, E. D., 2009: The moist static energy budget of a composite tropical intraseasonal oscillation in a climate model. *J. Climate*, **22**, 711–729, doi:10.1175/2008JCLI2542.1.

Mapes, B., 1997: Equilibrium vs. activation control of large-scale variations of tropical deep convection. *The Physics and Parameterization of Moist Atmospheric Convection*, R. K. Smith, Ed., Springer Netherlands, 321–358.

Mapes, B., S. Tulich, J. Lin, and P. Zuidema, 2006: The mesoscale convection life cycle: Building block or prototype for large-scale tropical waves? *Dynamics of Atmospheres and Oceans*, **42**, 3–29, doi:10.1016/j.dynatmoce.2006.03.003.

Mapes, B. E., 2000: Convective inhibition, subgrid-scale triggering energy, and stratiform instability in a toy tropical wave model. *J. Atmos. Sci.*, **57**, 1515–1535, doi:10.1175/1520-0469(2000)057<1515:CISSTE>2.0.CO;2.

Maruyama, T. and M. Yanai, 1967: Evidence of Large-Scale Wave Disturbances in the Equatorial Lower Stratosphere. *J. Meteor. Soc. Japan*, **45**, 196–199.

Masunaga, H., 2012: Short-term versus climatological relationship between precipitation and tropospheric humidity. *J. Climate*, **25**, 7983–7990, doi:10.1175/JCLI-D-12-00037.1.

Masunaga, H. and T. S. L'Ecuyer, 2014: A mechanism of tropical convection inferred from observed variability in the moist static energy budget. *J. Atmos. Sci.*, **71**, 3747–3766, doi:10.1175/JAS-D-14-0015.1.

Matsuno, T., 1966: Quasi-geostrophic motions in the equatorial area. *J. Meteor. Soc. Japan*, **44**, 25–42.

Neelin, J. D. and I. M. Held, 1987: Modeling tropical convergence based on the moist static energy budget. *Mon. Wea. Rev.*, **115**, 3–12, doi:10.1175/1520-0493(1987)115<0003:MTCBOT>2.0.CO;2.

Neelin, J. D., O. Peters, and K. Hales, 2009: The transition to strong convection. *J. Atmos. Sci.*, **66**, 2367–2384, doi:10.1175/2009JAS2962.1.

Neelin, J. D. and J.-Y. Yu, 1994: Modes of Tropical Variability under Convective Adjustment and the Madden-Julian Oscillation. Part I: Analytical Theory. *J. Atmos. Sci.*, **51**, 1876–1894, doi:10.1175/1520-0469(1994)051<1876:MOTVUC>2.0.CO;2.

Neelin, J. D. and N. Zeng, 2000: A quasi-equilibrium tropical circulation model-formulation*. *J. Atmos. Sci.*, **57**, 1741–1766, doi:10.1175/1520-0469(2000)057<1741:AQETCM>2.0.CO;2.

Peters, M. E. and C. S. Bretherton, 2005: A Simplified Model of the Walker Circulation with an Interactive Ocean Mixed Layer and Cloud-Radiative Feedbacks. *J. Climate*, **18**, 4216–4234, doi:10.1175/JCLI3534.1.

Peters, M. E. and C. S. Bretherton, 2006: Structure of tropical variability from a vertical mode perspective. *Theor. Comput. Fluid Dyn.*, **20**, 501–524, doi:10.1007/s00162-006-0034-x.

Raymond, D. J., 2000: Thermodynamic control of tropical rainfall. *Quart. J. Roy. Meteor. Soc.*, **126**, 889–898, doi:10.1002/qj.49712656406.

Raymond, D. J. and Ž. Fuchs, 2007: Convectively coupled gravity and moisture modes in a simple atmospheric model. *Tellus A*, **59**, 627–640, doi:10.1111/j.1600-0870.2007.00268.x.

Raymond, D. J. and Ž. Fuchs, 2009: Moisture modes and the Madden-Julian oscillation. *J. Climate*, **22**, 3031–3046, doi:10.1175/2008JCLI2739.1.

Raymond, D. J., S. Gjorgjievska, S. Sessions, and Ž. Fuchs, 2014: Tropical cyclogenesis and mid-level vorticity. *Aust. Meteor. Ocean J.*, **64**, 11–25.

Raymond, D. J. and M. J. Herman, 2011: Convective quasi-equilibrium reconsidered. *J. Adv. Model. Earth Syst.*, **3**, M08 003, doi:10.1029/2011MS000079.

Raymond, D. J., G. B. Raga, C. S. Bretherton, J. Molinari, C. López-Carrillo, and Ž. Fuchs, 2003: Convective Forcing in the Intertropical Convergence Zone of the Eastern Pacific. *J. Atmos. Sci.*, **60**, 2064–2082, doi:10.1175/1520-0469(2003)060<2064:CFITIC>2.0.CO;2.

Raymond, D. J., S. L. Sessions, and Ž. Fuchs, 2007: A theory for the spinup of tropical depressions. *Quart. J. Roy. Meteor. Soc.*, **133**, 1743–1754, doi:10.1002/qj.125.

Raymond, D. J., S. L. Sessions, A. H. Sobel, and Ž. Fuchs, 2009: The mechanics of gross moist stability. *J. Adv. Model. Earth Syst.*, **1**, 9, doi:10.3894/JAMES.2009.1.9.

Redelsperger, J.-L., F. Guichard, and S. Mondon, 2000: A Parameterization of Mesoscale Enhancement of Surface Fluxes for Large-Scale Models. *J. Climate*, **13**, 402–421, doi:10.1175/1520-0442(2000)013<0402:APOMEO>2.0.CO;2.

Riehl, H. and J. S. Malkus, 1958: On the heat balance in the equatorial trogh zone. *Geophysica*, **6**, 503–538.

Riley, E. M., B. E. Mapes, and S. N. Tulich, 2011: Clouds Associated with the Madden-Julian Oscillation: A New Perspective from CloudSat. *J. Atmos. Sci.*, **68**, 3032–3051, doi:10.1175/JAS-D-11-030.1.

Sentić, S., S. L. Sessions, and Ž. Fuchs, 2015: Diagnosing DYNAMO convection with weak temperature gradient simulations. *J. Adv. Model. Earth Syst.*, **7**, 1849–1871, doi:10.1002/2015MS000531.

Sobel, A. and E. Maloney, 2012: An idealized semi-empirical framework for modeling the Madden-Julian oscillation. *J. Atmos. Sci.*, **69**, 1691–1705, doi:10.1175/JAS-D-11-0118.1.

Sobel, A. and E. Maloney, 2013: Moisture modes and the eastward propagation of the MJO. *J. Atmos. Sci.*, **70**, 187–192, doi:10.1175/JAS-D-12-0189.1.

Sobel, A., S. Wang, and D. Kim, 2014: Moist static energy budget of the MJO during DYNAMO. *J. Atmos. Sci.*, **71**, 4276–4291, doi:10.1175/JAS-D-14-0052.1.

Sobel, A. H., 2007: Simple models of ensemble-averaged precipitation and surface wind, given the SST. *The Global Circulation of the Atmosphere*, T. Schneider and A. H. Sobel, Eds., Princeton University Press, 219–251.

Sobel, A. H. and C. S. Bretherton, 2000: Modeling tropical precipitation in a single column. *J. Climate*, **13**, 4378–4392, doi:10.1175/1520-0442(2000)013<4378:MTPIAS>2.0.CO;2.

Sobel, A. H. and C. S. Bretherton, 2003: Large-scale waves interacting with deep convection in idealized mesoscale model simulations. *Tellus A*, **55**, 45–60, doi:10.1034/j.1600-0870.2003.201421.x.

Sobel, A. H. and H. Gildor, 2003: A Simple Time-Dependent Model of SST Hot Spots. *J. Climate*, **16**, 3978–3992, doi:10.1175/1520-0442(2003)016<3978:ASTMOS>2.0.CO;2.

Sobel, A. H. and J. D. Neelin, 2006: The boundary layer contribution to intertropical convergence zones in the quasi-equilibrium tropical circulation model framework. *Theor. Comput. Fluid Dyn.*, **20**, 323–350, doi:10.1007/s00162-006-0033-y.

Sobel, A. H., J. Nilsson, and L. M. Polvani, 2001: The Weak Temperature Gradient Approximation and Balanced Tropical Moisture Waves*. *J. Atmos. Sci.*, **58**, 3650–3665, doi:10.1175/1520-0469(2001)058<3650:TWTGAA>2.0.CO;2.

Straub, K. H., P. T. Haertel, and G. N. Kiladis, 2010: An Analysis of Convectively Coupled Kelvin Waves in 20 WCRP CMIP3 Global Coupled Climate Models. *J. Climate*, **23**, 3031–3056, doi:10.1175/2009JCLI3422.1.

Straub, K. H. and G. N. Kiladis, 2003: The observed structure of convectively coupled Kelvin waves: Comparison with simple models of coupled wave instability. *J. Atmos. Sci.*, **60**, 1655–1668, doi:10.1175/1520-0469(2003)060<1655:TOSOCC>2.0.CO;2.

Su, H. and J. D. Neelin, 2002: Teleconnection Mechanisms for Tropical Pacific Descent Anomalies during El Nino*. *J. Atmos. Sci.*, **59**, 2694–2712, doi:10.1175/1520-0469(2002)059<2694:TMFTPD>2.0.CO;2.

Sugiyama, M., 2009a: The moisture mode in the quasi-equilibrium tropical circulation model. part I: Analysis based on the weak temperature gradient approximation. *J. Atmos. Sci.*, **66**, 1507–1523, doi:10.1175/2008JAS2690.1.

Sugiyama, M., 2009b: The Moisture Mode in the Quasi-Equilibrium Tropical Circulation Model. Part II: Nonlinear Behavior on an Equatorial beta Plane. *J. Atmos. Sci.*, **66**, 1525–1542, doi:10.1175/2008JAS2691.1.

Takayabu, Y. N., 1994: Large-Scale Cloud Disturbances Associated with Equatorial Waves Part I: Spectral Features of the Cloud Disturbances. *J. Meteor. Soc. Japan*, **72**, 433–449.

Takayabu, Y. N., K. Lau, and C. Sui, 1996: Observation of a quasi-2-day wave during TOGA COARE. *Mon. Wea. Rev.*, **124**, 1892–1913, doi:10.1175/1520-0493(1996)124<1892:OOAQDW>2.0.CO;2.

Tian, B. and V. Ramanathan, 2003: A Simple Moist Tropical Atmosphere Model: The Role of Cloud Radiative Forcing. *J. Climate*, **16**, 2086–2092, doi:10.1175/1520-0442(2003)016<2086:ASMTAM>2.0.CO;2.

Velden, C. S. and J. A. Young, 1994: Satellite observations during TOGA COARE: Large-scale descriptive overview. *Mon. Wea. Rev.*, **122**, 2426–2441, doi:10.1175/1520-0493(1994)122<2426:SODTCL>2.0.CO;2.

Wallace, J. M. and V. E. Kousky, 1968: Observational Evidence of Kelvin Waves in the Tropical Stratosphere. *J. Atmos. Sci.*, **25**, 900–907, doi:10.1175/1520-0469(1968)025<0900:OEOKWI>2.0.CO;2.

Webster, P. J. and R. Lukas, 1992: TOGA COARE: The coupled ocean-atmosphere response experiment. *Bull. Amer. Meteor. Soc.*, **73**, 1377–1416, doi:10.1175/1520-0477(1992)073<1377:TCTCOR>2.0.CO;2.

Weller, R. A. and S. P. Anderson, 1996: Surface Meteorology and Air-Sea Fluxes in the Western Equatorial Pacific Warm Pool during the TOGA Coupled Ocean-Atmosphere Response Experiment. *J. Climate*, **9**, 1959–1990, doi:10.1175/1520-0442(1996)009<1959:SMAASF>2.0.CO;2.

Wentz, F., C. Gentemann, and K. Hilburn, 2015: Remote Sensing Systems TRMM TMI Daily Environmental Suite on 0.25 deg grid, Version 7.1. Remote Sensing Systems, Santa Rosa, CA, [Available online at `www.remss.com/missions/tmi`].

Wentz, F., K. Hilburn, and D. Smith, 2012: Remote Sensing Systems DMSP SSM/I Daily Environmental Suite on 0.25 deg grid, Version 7. Remote Sensing Systems, Santa Rosa, CA, [Available online at `www.remss.com/missions/ssmi`].

Wentz, F., T. Meissner, C. Gentemann, and M. Brewer, 2014: Remote Sensing Systems AQUA AMSR-E Daily Environmental Suite on 0.25 deg grid, Version 7.0.

Remote Sensing Systems, Santa Rosa, CA, [Available online at www.remss.com/missions/amsre].

Wheeler, M. and G. N. Kiladis, 1999: Convectively Coupled Equatorial Waves: Analysis of Clouds and Temperature in the Wavenumber-Frequency Domain. *J. Atmos. Sci.*, **56**, 374–399, doi:10.1175/1520-0469(1999)056<0374:CCEWAO>2.0.CO;2.

Wu, Z., 2003: A shallow CISK, deep equilibrium mechanism for the interaction between large-scale convection and large-scale circulations in the tropics. *J. Atmos. Sci.*, **60**, 377–392, doi:10.1175/1520-0469(2003)060<0377:ASCDEM>2.0.CO;2.

Yanai, M., B. Chen, and W. Tung, 2000: The Madden-Julian oscillation observed during the TOGA COARE IOP: Global view. *J. Atmos. Sci.*, **57**, 2374–2396, doi:10.1175/1520-0469(2000)057<2374:TMJOOD>2.0.CO;2.

Yanai, M., S. Esbensen, and J.-H. Chu, 1973: Determination of bulk properties of tropical cloud clusters from large-scale heat and moisture budgets. *J. Atmos. Sci.*, **30**, 611–627, doi:10.1175/1520-0469(1973)030<0611:DOBPOT>2.0.CO;2.

Yanai, M. and T. Maruyama, 1966: Stratospheric Wave Disturbances Propagating over the Equatorial Pacific. *J. Meteor. Soc. Japan*, **44**, 291–294.

Yasunaga, K. and B. Mapes, 2012: Differences between More Divergent and More Rotational Types of Convectively Coupled Equatorial Waves. Part II: Composite Analysis based on Space-Time Filtering. *J. Atmos. Sci.*, **69**, 17–34, doi:10.1175/JAS-D-11-034.1.

Yu, J., C. Chou, and J. D. Neelin, 1998: Estimating the gross moist stability of the tropical atmosphere*. *J. Atmos. Sci.*, **55**, 1354–1372, doi:10.1175/1520-0469(1998)055<1354:ETGMSO>2.0.CO;2.

Yu, J.-Y. and J. D. Neelin, 1994: Modes of Tropical Variability under Convective Adjustment and the Madden-Julian Oscillation. Part II: Numerical Results. *J. Atmos. Sci.*, **51**, 1895–1914, doi:10.1175/1520-0469(1994)051<1895:MOTVUC>2.0.CO;2.

Zebiak, S. E., 1986: Atmospheric Convergence Feedback in a Simple Model for El Niño. *Mon. Wea. Rev.*, **114**, 1263–1271, doi:10.1175/1520-0493(1986)114<1263:ACFIAS>2.0.CO;2.

Zhang, C., 2005: Madden-Julian Oscillation. *Rev. Geophys.*, **43**, RG2003, doi:10.1029/2004RG000158.

Zhang, C., 2013: MaddenâŁ"Julian Oscillation: Bridging Weather and Climate. *Bull. Amer. Meteor. Soc.*, **94**, 1849–1870, doi:10.1175/BAMS-D-12-00026.1.

Zhang, M. H. and J. L. Lin, 1997: Constrained variational analysis of sounding data based on column-integrated budgets of mass, heat, moisture, and momentum: Approach and application to ARM measurements. *J. Atmos. Sci.*, **54**, 1503–1524, doi:10.1175/1520-0469(1997)054<1503:CVAOSD>2.0.CO;2.